

APPLICATIONS OF MODEL PREDICTIVE CONTROL TO  
VEHICLE DYNAMICS FOR ACTIVE SAFETY AND STABILITY

A DISSERTATION  
SUBMITTED TO THE DEPARTMENT OF MECHANICAL  
ENGINEERING  
AND THE COMMITTEE ON GRADUATE STUDIES  
OF STANFORD UNIVERSITY  
IN PARTIAL FULFILLMENT OF THE REQUIREMENTS  
FOR THE DEGREE OF  
DOCTOR OF PHILOSOPHY

Craig E. Beal  
July 2011

*This dissertation is dedicated to my family.*

# Acknowledgement

Acknowledgements go here.

# Contents

		iv
<b>Acknowledgement</b>		v
<b>1</b>	<b>Introduction</b>	<b>1</b>
1.1	Motivation . . . . .	1
1.2	Background . . . . .	3
1.2.1	Overview of the Vehicle Stability Problem . . . . .	3
1.2.2	Development of Electronic Stability Control . . . . .	6
1.2.3	Friction and State Estimation Techniques . . . . .	9
1.2.4	Envelope Protection in Aircraft . . . . .	10
1.2.5	Vehicle Control with Model Predictive Control . . . . .	11
1.2.6	Analysis of Unstable Vehicle Dynamics . . . . .	12
1.3	Dissertation Contributions . . . . .	14
1.3.1	Instability Analysis and Criteria for Safe Handling . . . . .	15
1.3.2	Envelope Control for Enforcing Envelope Boundaries . . . . .	15
1.3.3	Guarantees of Vehicle Behavior under Envelope Control . . . . .	16
1.3.4	Integration of Real-Time Friction Estimation . . . . .	16
1.3.5	Extension of Envelope Control to Roll Dynamics . . . . .	17
1.4	Dissertation Outline . . . . .	17
<b>2</b>	<b>Vehicles and Models</b>	<b>20</b>
2.1	Pneumatic Tires . . . . .	20
2.1.1	Brush Tire Model . . . . .	21

2.1.2	Linear Tire Model . . . . .	26
2.2	Chassis Models . . . . .	27
2.2.1	Four Wheel Yaw-Roll Model . . . . .	27
2.2.2	Bicycle Model . . . . .	28
2.2.3	Affine Force-Input Model . . . . .	31
2.2.4	Linearized Roll Model . . . . .	33
2.2.5	Summary of Models . . . . .	34
2.3	P1 By-Wire Test Vehicle . . . . .	35
2.4	Experimental Testing . . . . .	37
<b>3</b>	<b>Vehicle Instability</b>	<b>38</b>
3.1	Instability Dynamics . . . . .	38
3.2	Defining Boundaries of Unstable Regions . . . . .	46
3.2.1	Defining a Safe Handling Envelope . . . . .	47
3.2.2	Alternative Envelopes . . . . .	49
3.3	Discussion . . . . .	54
<b>4</b>	<b>Envelope Control</b>	<b>55</b>
4.1	Control Strategy . . . . .	55
4.1.1	MPC with the Affine Force-Input Model . . . . .	56
4.1.2	Envelope Boundaries . . . . .	58
4.1.3	Tracking Driver Intent . . . . .	59
4.1.4	Controller Implementation . . . . .	60
4.1.5	Real Time MPC Implementation . . . . .	62
4.2	Results and Discussion . . . . .	63
4.2.1	Experiment: Limit Slalom Maneuver . . . . .	63
4.2.2	Simulation: Slalom with Friction Variation . . . . .	65
4.2.3	Experiment: Limit Cornering with Rear Drive Torques . . . . .	67
4.2.4	Experiment: Control Performance with Linear Model . . . . .	70
4.2.5	Experiment: Control with Wide Slip Boundaries . . . . .	72
4.3	Guaranteeing Controller Action . . . . .	74
4.3.1	Envelope Invariance Proof . . . . .	74

4.3.2	Envelope Attraction . . . . .	80
4.3.3	Feasible Trajectories . . . . .	81
4.3.4	Effect of Actuator Limits . . . . .	84
4.4	Summary . . . . .	85
<b>5</b>	<b>Real Time Estimation</b>	<b>87</b>
5.1	Estimation Technique . . . . .	87
5.1.1	Slip Angle Estimation . . . . .	88
5.1.2	Peak Force Estimation . . . . .	89
5.1.3	Practical Considerations . . . . .	92
5.2	Estimator Results . . . . .	94
5.2.1	Estimator Input Data Characteristics . . . . .	94
5.2.2	Slip Angle Observer Results . . . . .	97
5.2.3	Pneumatic Trail and Friction Results . . . . .	98
5.3	Coupled Controller/Estimator Design . . . . .	100
5.4	Control Results with Real Time Estimation . . . . .	101
5.4.1	System Convergence . . . . .	102
5.4.2	Coupled Operation . . . . .	102
5.4.3	Controller Parameter Sensitivity . . . . .	105
5.4.4	“Locked-low” Operating Regime . . . . .	107
5.5	Discussion . . . . .	109
<b>6</b>	<b>Extensions of Envelope Control</b>	<b>110</b>
6.1	Control of Roll Dynamics . . . . .	110
6.1.1	Control Approach . . . . .	111
6.1.2	MPC Expression . . . . .	113
6.1.3	Real Time MPC Implementation . . . . .	115
6.2	Simulation Results . . . . .	116
6.2.1	Roll Control Objective . . . . .	116
6.2.2	Baseline Dynamics . . . . .	116
6.2.3	Independent Wheel Torque Control . . . . .	119
6.2.4	Rear Wheel Steering Control . . . . .	120

6.3 Discussion . . . . .	123
<b>7 Conclusions</b>	<b>125</b>
7.1 Summary . . . . .	125
7.1.1 Safe Handling Envelopes . . . . .	125
7.1.2 Real Time Model Predictive Control . . . . .	126
7.1.3 Real Time Friction and Sideslip Estimation . . . . .	126
7.1.4 Extension of the Envelope Control Technique . . . . .	126
7.2 Future Work . . . . .	127
7.2.1 Driver Feedback . . . . .	127
7.2.2 Controller Complexity . . . . .	127
7.2.3 Handling Environmental Constraints . . . . .	128
7.3 Outlook . . . . .	128
<b>A X1 Experimental Test Vehicle</b>	<b>130</b>
A.1 Physical Design . . . . .	130
A.1.1 Modularity Concept . . . . .	131
A.1.2 Actuation Opportunities . . . . .	133
A.1.3 Drivetrain . . . . .	133
A.2 Electrical Design . . . . .	134
A.2.1 Power System . . . . .	134
A.2.2 Data Network . . . . .	134
A.3 Discussion . . . . .	135
<b>Bibliography</b>	<b>136</b>

# List of Tables

2.1	Vehicle Models . . . . .	35
2.2	Parameters for the P1 test vehicle . . . . .	36
4.1	Description of Envelope Controller Parameters . . . . .	61
4.2	Envelope Controller Parameters with AFI Model . . . . .	65
4.3	Envelope Controller Parameters with Linear Model . . . . .	69
6.1	Description of Roll Controller Parameters . . . . .	115
6.2	Independent Wheel Torque Roll Controller Parameters . . . . .	119
6.3	Rear Steering Roll Controller Parameters . . . . .	121

# List of Figures

1.1	Vehicle Dynamics Axes and Coordinates . . . . .	4
1.2	Electronic Stability Control Action . . . . .	7
1.3	Phase Portrait Showing Instability Dynamics . . . . .	13
2.1	Tire Curve - Two Coefficient Brush Model . . . . .	22
2.2	Force Distribution in the Contact Path . . . . .	23
2.3	Combined Tire Force Limits . . . . .	25
2.4	Comparison of Linear and Brush Tire Models . . . . .	26
2.5	Four-wheel Yaw-Roll Model . . . . .	28
2.6	The Bicycle Model . . . . .	29
2.7	P1 Steer and Drive By-Wire Research Testbed . . . . .	36
3.1	Phase Portraits of a Neutral Steering Vehicle . . . . .	40
3.2	Phase Portraits of an Understeering Vehicle . . . . .	42
3.3	Phase Portraits of an Oversteering Vehicle . . . . .	43
3.4	Vehicle Spin-out Data in the Phase Plane . . . . .	44
3.5	Phase Portrait of a Neutral Steering Vehicle at Higher Speed . . . . .	45
3.6	Phase Portrait with Model Predictive Envelope Controller . . . . .	48
3.7	Vehicle Derivatives on Envelope Boundaries . . . . .	49
3.8	Handling Envelope with Wider Slip Bounds . . . . .	51
3.9	Handling Envelope with Extra Allowable Yaw Rate . . . . .	52
3.10	Yaw Sideslip Handling Envelope . . . . .	53
4.1	MPC Block Diagram . . . . .	57

4.2	MPC Envelope Controller Boundaries . . . . .	58
4.3	Experimental Results from Slalom Maneuver . . . . .	64
4.4	Simulated Results from Slalom Maneuver . . . . .	66
4.5	Experimental Results from Cornering with Torque Disturbances . . . . .	68
4.6	Experimental Results from Lift-off Oversteer Maneuver . . . . .	71
4.7	Experimental Results with Wide Rear Slip Angle Boundaries . . . . .	73
4.8	Four quadrants of the state space used for the proof . . . . .	78
4.9	Feasible Envelope Re-entry Trajectory . . . . .	83
4.10	Slew Distance for Change of Tire Force . . . . .	84
4.11	Envelope Re-entry with Slew Rate Limitation . . . . .	85
5.1	Steering Axis Geometry . . . . .	90
5.2	Lateral Force and Linear Pneumatic Trail Models . . . . .	92
5.3	Coupled Sideslip and Friction Estimator Flowchart . . . . .	93
5.4	Representative Inertial Measurements . . . . .	95
5.5	Representative Steering Derivative . . . . .	95
5.6	Representative Aligning Moments . . . . .	95
5.7	Aligning Moment Frequency Content . . . . .	96
5.8	Slip Angle Estimates . . . . .	97
5.9	Calculated Pneumatic Trail . . . . .	99
5.10	Calculated Friction Coefficient . . . . .	100
5.11	Calculated Friction Coefficient . . . . .	101
5.12	Friction Convergence under Control . . . . .	103
5.13	Control with Real Time Estimation . . . . .	104
5.14	Over-response with Real Time Estimation . . . . .	106
5.15	“Locked-low” Coupled System Operation . . . . .	108
6.1	Vehicle state and input trajectories for baseline (inactive) case . . . . .	117
6.2	Vehicle state trajectories for drive/brake torque controller . . . . .	118
6.3	Inputs for controlled fast ramp steer with differential drive . . . . .	118
6.4	Vehicle state trajectories for rear wheel steering controller . . . . .	122
6.5	Inputs for controlled fast ramp steer with rear wheel steering . . . . .	123

A.1	X1 steer and drive by-wire research testbed . . . . .	131
A.2	Front-Middle-Rear Modularity Concept . . . . .	132
A.3	CAD Mockup of Modular Structure . . . . .	132
A.4	Electronic Modularity Concept . . . . .	135

# Chapter 1

## Introduction

### 1.1 Motivation

In the United States, the automobile is a foundation upon which many aspects of daily life are built. Cars provide opportunities, including the freedom to live at a distance from employers, the ability to travel, and even the option to express oneself with choice of vehicle. The utility of the automobile is clear, and the proof lies in approximately 2.9 trillion vehicle miles traveled in 2009 alone in the United States [48]. However, the cost in human lives is also clear. In that same year, nearly 34 thousand people were killed and 2.2 million people were injured in the U.S. as a result of vehicle crashes [48]. Often these crashes occur in unfavorable conditions brought about due to the actions of the driver or interactions with the environment. Excessive speed and sudden changes in surface friction due to gravel, snow, or ice are commonly associated with these types of loss-of-control crashes. In these conditions, the dynamics of the vehicle change drastically from those of normal everyday driving. Unprepared drivers who must suddenly handle the vehicle in these challenging driving regimes may fail to respond appropriately and lose control.

Automotive manufacturers have addressed this problem through the addition of active safety systems in production vehicles. These systems, including Anti-Lock Braking (ABS), Traction Control (TCS), Electronic Stability Control (ESC), and Roll Stability Control (RSC) utilize control over the drive and brake systems of the

vehicle to augment the driver's actions and improve the handling response of the vehicle. Since their implementation, these systems have improved the ability of drivers to maintain control of the vehicle and have resulted in significant reductions in the human cost of automobiles. Studies of ESC by the National Highway Traffic Safety Administration (NHTSA) have shown that ESC can be credited with a 36% reduction in single-vehicle crashes among ESC-equipped vehicles in the United States [16].

Despite the effectiveness of these assistance systems, vehicle crashes resulting in injuries and fatalities continue to occur. Therefore, future assistance systems must go farther to help the driver of the vehicle. This may be enabled through the use of new technologies that provide information about the environment, perhaps including road conditions, obstacles, and other vehicles. One example is the adoption of Electric Power Steering (EPS) in many production vehicles, which can be leveraged to obtain information about the vehicle states and the road friction coefficient at a low cost to the manufacturer. This information can be used in driver assistance systems to increase the speed and accuracy of their response.

However, incorporating additional information is a challenge on its own. Current production stability control systems utilize a limited suite of measurements, including vehicle yaw rate, speed, lateral acceleration, and steering wheel position. These measurements are reliable and readily available on production vehicles, but do not yield a complete picture of the vehicle behavior. As a result, the actuation schema currently used to alter the dynamics of the vehicle are relatively simple and rely on high level logic and experimentally determined thresholds. Thousands of hours of development have refined the implementations of these systems to tune the performance and ensure the system works as desired. However, in order to incorporate more information into these systems and provide more refined assistance to the driver, a systematic approach to the analysis and development of controllers is needed. This dissertation addresses the challenges of leveraging additional measurements to determine appropriate state boundaries for the vehicle and using model predictive control to incorporate this additional information into the control of handling dynamics to improve the safety of vehicles.

## 1.2 Background

### 1.2.1 Overview of the Vehicle Stability Problem

In order to define the task of the assistance system described in this dissertation, it is necessary to define the basic dynamics that are relevant to maintaining control of the vehicle. Figure 1.1 shows a vehicle with a coordinate system defined by ISO Standard 8855. The axes are fixed to the body of the vehicle with the positive x-axis pointing in the forward direction, the positive y-axis to the driver's left, and the positive z-axis pointing upward. The vector  $V$  points in the direction of the vehicle's velocity, allowing for the definition of an angle,  $\beta$ , that is referred to as the sideslip angle. This angle, the difference between the vehicle's heading and its velocity, is a measure of how sideways the vehicle is traveling. Clearly one often travels at highway speed with zero sideslip angle, but it would be highly disconcerting to be traveling at the same speed with a  $90^\circ$  sideslip angle. Therefore, restricting the sideslip angle to moderate values is a critical task for stability control.

The other quantity of interest is the yaw rate, which is the rate at which the vehicle rotates about the z-axis. If this yaw rate becomes too large and cannot be controlled, the vehicle is said to have "spun out." Therefore, this is the second quantity that production ESC systems control to improve the stability of the vehicle. Like these production systems, the driver assistance system presented in this dissertation also uses the yaw rate and sideslip angles to improve the response of the vehicle at the limits of its handling capabilities.

The yaw rate and sideslip angle of the vehicle are generated as a result of the tire forces, which must be examined to understand the vehicle behavior when the handling limitations are reached. These forces are generated by the adhesion of the tire rubber to the road and can be used to drive the vehicle forward, brake it, or generate lateral force to traverse a corner. Like the sideslip angle for the vehicle body, a slip angle is defined between the heading of the wheel and its velocity. Because the wheel is attached to the body of the vehicle, the lateral velocity and yaw rate of the vehicle body result in tire slip angles. The lateral force generated by the tire increases with the slip angle until the limits of the tire-road friction are reached. The

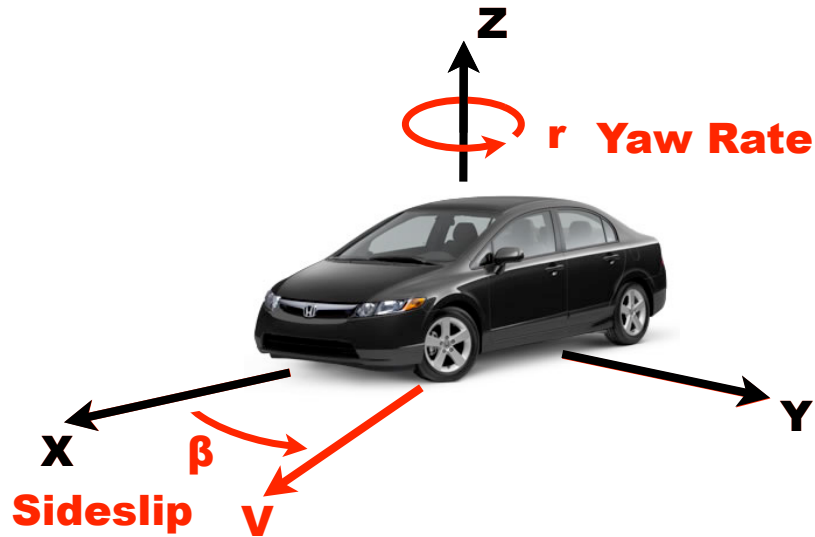


Figure 1.1: Vehicle Dynamics Axes and Coordinates

driver controls the front force by increasing or decreasing the front slip angle with the steering wheel, which results in sideslip and yaw rate motion of the vehicle. As these motions occur, the rear axle also assumes a slip angle and produces forces. When the vehicle is operating in a stable regime, these forces balance and the vehicle reaches an equilibrium state.

Depending on the handling properties of the vehicle, including the mass distribution, the suspension set up, the tire characteristics, and other factors, these equilibria will change as the steering angle changes, the vehicle speed increases, or the driver utilizes some of the available friction force to accelerate or brake the vehicle. At some point, the friction force is insufficient to maintain the equilibrium and the tires on either axle begin to slide. Once the front tires reach this condition, the vehicle will cease to turn any more and the vehicle is said to “understeer” the driver command at the limits of handling. Conversely, if the rear tires lose grip first and the front tires continue to generate high levels of force, the vehicle will turn too much and is said to “oversteer” the driver command at the limits of handling. It is also possible for both axles to lose grip simultaneously, which results in a large sideslip angle with a

low yaw rate and is referred to as “neutral” at the limits.

Fundamentally, the role of a stabilization system is to keep the vehicle from deviating significantly from the behavior intended by the driver, such as in these oversteer and understeer situations. However, this task is challenging since the true intent of the driver may be infeasible given the handling limits of the vehicle, and in any case cannot be measured. Therefore, the control system cannot simply track the driver’s intent and the problem must be phrased in an alternate manner. For production stability control systems, this is addressed by inferring the desired vehicle behavior from a linear model and a limited set of sensor measurements [70]. These measurements are combined with estimates of the states and tire-road friction coefficient and are compared to the linear model. Control action is taken if there is significant deviation. This control scheme is highly effective, as seen from NHTSA analysis [48], and is robust despite the limited sensor suite it utilizes. However, the reliance on deviation from a linear model has two drawbacks. The first is that the stability control system allows only dynamics that are close to the linear model, while skilled drivers may be able to access other handling regimes. The second is that in order to avoid unnecessary interventions, the system must not take action until the vehicle behavior is measureably outside of the stable regime.

While these types of trade-offs are required in a system for which it is feasible to install on production vehicles, a number of technologies that have the capability of providing additional information and actuation to stability control systems are appearing on the market. Among these enabling technologies are electric power steering and steer-by-wire systems. With these actuators comes the ability to measure steering torque and with it, the ability to accurately estimate both the tire-road friction coefficient and the vehicle sideslip angle [31].

With estimates of the states and friction characteristics available, it is possible to take a different approach to vehicle stabilization. Most drivers are aware that there exist inherent limitations in tire grip and therefore in the vehicle handling capabilities. Very highly skilled drivers can operate the vehicle at these limits without allowing the vehicle to become unstable. However, less skilled drivers may exceed

these handling limits without realizing it, perhaps due to aggressive driving or emergency maneuvering. With full-state feedback available, an advanced stabilization system can accurately estimate these limitations and assist the driver in maintaining the vehicle inside the bounds of the vehicle capabilities. Thus, the system may be referred to as an “envelope control” system, similar to the envelope protection systems used in modern commercial aircraft [72]. This envelope control concept is the basis for the assistance system described in this dissertation.

### 1.2.2 Development of Electronic Stability Control

The first assistance system to appear in production vehicles was Anti-Lock Braking (ABS). This system utilizes a set of valves to modulate pressure to the brakes at individual wheels. By rapidly applying and releasing brake pressure, the system keeps the wheels rolling, simultaneously reducing stopping distance and improving steerability of the vehicle. A fully-electronic, 4 channel system was first introduced by Bosch and Mercedes-Benz in 1978 for trucks and the S-Class sedan [1]. Traction Control (TCS), which prevents wheel-spin under engine torque, was developed later using the same principles.

Once independent control of the wheels of the vehicle became possible, a new control challenges was observed. On a surface with varied levels of grip between the two sides of the vehicle, a naive ABS system attempting to provide maximum braking on each wheel would produce different longitudinal forces on each side of the vehicle and tend to apply a yaw moment that would cause an undesirable rotation of the vehicle. While unintended in the split- $\mu$  braking situation, the resultant yaw motion from differential longitudinal force on the left and right sides of the vehicle can be leveraged to improve the response of the vehicle.

Production electronic stability control systems operate, like ABS, by actuating the brakes of the vehicle independently to control the orientation of the vehicle. The angle of the steering wheel, the vehicle speed, the rotation (yaw) rate of the vehicle, and the lateral acceleration of the vehicle are readily measured with inexpensive sensors. Based on a simple model of the vehicle dynamics, the driver’s intended

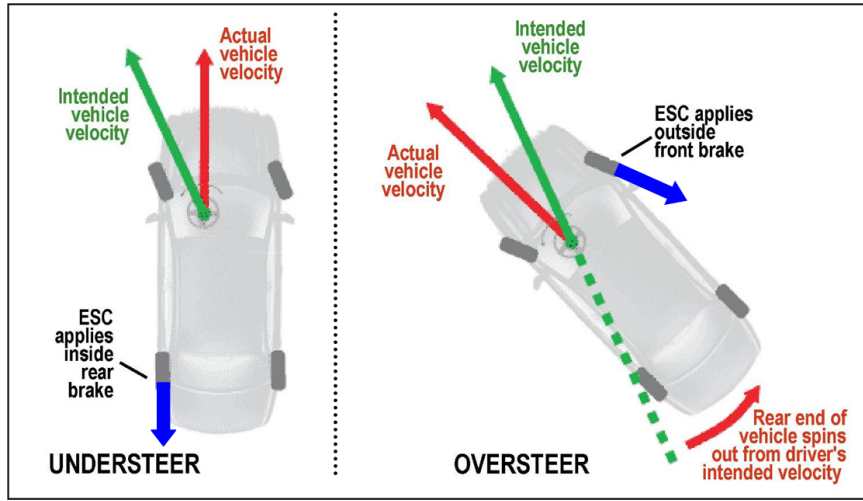


Figure 1.2: Electronic Stability Control Action [11]

vehicle behavior can be inferred from the vehicle speed and handwheel angle. The ESC system compares these desired states to the measurements of yaw rate and lateral acceleration to determine whether the driver requires assistance in stabilizing the vehicle. If there is a significant difference between the inferred states and the measurements, the system applies the brakes to correct the vehicle motion [70, 69].

There are two situations in which an ESC system intervenes to assist the driver. The first is an understeer situation, where the vehicle fails to turn as much as the driver would like. In this case, the ESC system may apply the inside rear brake judiciously to make the vehicle rotate more. However, the system is typically programmed to do this only in severe understeering situations since the application of the rear brake may cause the rear end of the car to lose grip and spin out. This is the second situation that ESC systems help to prevent. When the vehicle begins to oversteer, the ESC system can apply the outside front brake, which produces a yaw moment that tends to straighten out the vehicle and prevents a spin.

Unfortunately, production ESC systems are limited by their reliance on a small set of sensors that yield limited vehicle state information. As a result, they must react only to deviations from a known model of the vehicle behavior and typically have a “dead-band” where small deviations are allowed in order to prevent undesirable interventions in non-critical situations. Additional information about the vehicle

states and the environment would be helpful in improving the system response, since a system that could accurately gauge the situation would need not wait for a large deviation from normal driving and could offer more subtle assistance to the driver.

In addition to the production ESC systems automotive manufacturers and suppliers, many other authors have proposed methods for addressing the challenge of controlling the planar dynamics of a vehicle in adverse situations. Manning and Crolla give an excellent summary of the body of work in their 2007 survey paper [42]. Reviewing 68 salient papers, the authors divided the work into three general groups by primary control objective. The groups included work that focused on control of yaw rate, control of sideslip, and work that considered both states for control. When looking at direct yaw control work, Manning and Crolla found that yaw stability systems are dominated by the use of model reference feedback control of the yaw rate and note that attempting to track a linear reference model in the nonlinear handling region can result in excessive actuator effort ([43, 41]). Chapter 3 of this dissertation presents an analysis to show that while restricting the yaw rate is critical for stability, tracking a reference model is unnecessary when appropriate yaw limits can be calculated.

Among proposed techniques for control of the vehicle sideslip angle, Manning and Crolla found that many researchers used differential braking due to its effectiveness across a wide range of handling conditions. However, it was noted that some authors argue that brake-based stability is overly invasive in the longitudinal dynamics of the vehicle ([26, 63]). Finally, authors who considered both sideslip and yaw rate generally treated the problem as a multi-objective control problem and either used multiple actuators to address the separate objectives or used techniques such as sliding surface control to trade off the objectives when only one actuator was used ([29, 66, 75]).

Interestingly, Manning and Crolla also noted that in the body of published work, there are many theoretical studies that lack consideration of the practical aspects involved in implementing the system and similarly many studies with excellent practical value but little detail in the analysis of the vehicle dynamics or the control laws. This highlights the difficulty in developing a system that accurately accounts for the

nonlinear dynamics of the system and yet is straightforward enough for implementation on a vehicle. In controlling the sideslip dynamics of the vehicle with or without coordination with yaw control, the authors also found that there was a significant lack of work that incorporated real time estimation of the surface friction coefficient and sideslip angle.

### 1.2.3 Friction and State Estimation Techniques

One of the reasons that production ESC systems use the model following control approach that Manning and Crolla mention is that they lack information about the full capabilities of the vehicle on the road surface. However, given full-state feedback for the vehicle and the tire-road friction coefficient, it is possible to define limits to form a stable vehicle handling envelope.

There have been a variety of investigators who have developed techniques for providing the required state and friction information. Full-state feedback of the vehicle states can be provided with GPS hardware. Given the yaw angle, yaw rate, and the direction of the vehicle travel, a full description of the planar vehicle dynamics is possible [57, 8]. However, the equipment currently required to do this level of state feedback is expensive and impractical for a production vehicle and is subject to drop-out in areas where good visibility of the GPS satellite constellation is obscured. Therefore, an estimation technique that relies on commonly installed vehicle sensors is necessary to allow for advanced driver assistance on mass-produced vehicles. Several authors have proposed sideslip angle estimation schemes, but the foundation for these estimators are accurate tire models, which cannot be assumed in the presence of varying road conditions, tire wear, variable vehicle loading, and other variable conditions [37, 64, 71, 74]. Therefore, an estimate of the tire forces is simultaneously needed to complete the description of the vehicle behavior in all conditions.

Work by Sakai points out the challenges in developing accurate estimates of the tire forces. Because the tire characteristics change with a huge number of factors including normal variations in tread wear, inflation pressure, temperature, and normal load, it is impractical to use a parameterized tire model to estimate tire-road friction [58].

Therefore, alternative approaches such as those based on longitudinal tire slip have been proposed, utilizing known excitation of the wheel dynamics to estimate friction coefficients [23, 34, 54]. Other authors have utilized the lateral dynamics of the vehicle for excitation, but require lateral accelerations near the limit of the vehicle capability before obtaining accurate friction estimates, rendering them less useful for predicting the limits of the vehicle handling before reaching them [2, 22]. For the purposes of preventing the vehicle from developing unstable dynamics, a technique that provides an estimate of the available friction at lower lateral accelerations is needed.

Fortunately, such a technique has been developed. In work done by Hsu and Gerdes, the effort of an electric motor in a steer-by-wire system was used as a sensor to determine the slip angles of each axle and the friction coefficient of the tire road interface [32]. Information about the lateral force generation on the tires is obtained in the same manner as an experienced driver noticing that the steering is feeling “light” and using this information as a warning that the limits are approaching. As the steering effort decreases, the estimation technique can extract information about both the tire slip angle and the friction coefficient. Better yet, the pneumatic tire loses grip progressively, leading to a characteristic change in the steering torque. Thus, the peak force capability of the tire can be identified by the time the tire is approximately halfway to its grip limit and the friction information can be used to predict the vehicle motion and avoid hazardous situations when slippery conditions are encountered.

#### 1.2.4 Envelope Protection in Aircraft

With estimates of the states and friction characteristics available before reaching the handling limits of the vehicle, it is possible to take a different approach to vehicle stabilization than that of ESC. Most drivers are aware that there exist inherent limitations in tire grip and therefore in the vehicle handling capabilities. Very highly skilled drivers can operate the vehicle at these limits without allowing the vehicle to become unstable. However, less skilled drivers may exceed these handling limits without realizing it, perhaps due to aggressive driving or emergency maneuvering. With full-state feedback available, the stability control system can accurately estimate these

limitations and assist the driver in maintaining the vehicle inside the bounds of the vehicle capabilities. Thus, the system may be referred to as an “envelope control” system, similar to the envelope protection systems used in modern commercial aircraft [72, 73, 14, 15]. These systems restrict the pilot input to enforce bounds on values of angle-of-attack, bank angle, airspeed, and aerodynamic loading. Hsu and Gerdès demonstrated a system for an automobile that used front steer-by-wire for actuation and prevented the vehicle from exceeding front and rear slip angle thresholds [33].

Envelope protection systems, whether on aircraft or ground vehicles, are designed for assistance, not autonomous control of the system. Therefore, an important design issue is to ensure that cooperative control with the pilot or driver is possible. The Airbus and Boeing systems achieve in different ways, as the Airbus system restricts the pilot input electronically, preventing the pilot from reaching any forbidden condition. The Boeing system uses haptic feedback to resist excessive pilot input, but can be overridden with additional effort from the pilot [49, 72]. Regardless of the limitation mechanism, the overall interaction is the same. The pilot has unaltered control of the aircraft within the normal flight envelope and is restricted by the system only when the aircraft performance limits would be exceeded. The same operational behavior is designed into the vehicle envelope controller presented in this dissertation.

### 1.2.5 Vehicle Control with Model Predictive Control

The task of keeping the vehicle within the envelope boundaries while attempting to follow a driver command is well-matched to the structure of model predictive control. In a model predictive control scheme, the action of the controller is the solution to an optimization problem, providing a method for incorporating both an objective as well as constraints. Taken in the context of the stabilization problem, the objective can be leveraged to express the driver’s intended vehicle behavior while the constraints represent the physical limitations of the vehicle. Therefore, the controller responds as desired, allowing the driver full freedom to control the vehicle away from the boundaries but providing the necessary assistance to prevent the vehicle from exiting the safe handling envelope.

Several other authors have published model predictive techniques to control vehicle behavior. Falcone, et. al. presented investigations on the use of model predictive control for autonomous driving when the desired vehicle path is known *a priori* [9, 19]. Palmieri et. al. developed a model predictive regulator to decrease excessive yaw rate or sideslip angle beyond a pair of thresholds [53], and Bernardini et. al. presented a reference tracking controller with tire slip limits [7]. While these authors focused on autonomous operation and reference tracking, the approach taken in this dissertation uses model predictive control to define and enforce a safe handling envelope in which the driver can maneuver.

Common to all of these publications is the issue of modeling the nonlinear vehicle behavior for control. Since critical driver assistance situations typically occur at the limits of handling, a linear model of the tire behavior results in significant modeling error and poor controller performance. Models that represent the full nonlinear dynamics, however, present problems in terms of practical constraints such as computational time and parameter uncertainty in addition to the possibility of producing emergent behaviors. As a result, Falcone, et. al. used a full nonlinear tire model in simulation but approximated this model with linearizations for real time operation [9]. Palmieri et. al. linearized the equations of motion for the combined system of the vehicle and the tires [53], and Bernardini et. al. used a piecewise linear representation of the tire forces [7]. In this work, the input is formulated as front lateral force, rather than steering angle. As a result, the input nonlinearity is extracted rather than linearized and the control action is more precise, leading to close adherence to the envelope boundaries in operation.

### 1.2.6 Analysis of Unstable Vehicle Dynamics

In developing the boundaries for the model predictive envelope controller, key insights were gained by identifying specific vehicle dynamics that lead to the destabilization of the vehicle. Inagaki, et. al. [62], introduced a method of examining vehicle stability using the phase plane and demonstrated the existence of unstable regions reachable through driver steering input. However, Inagaki, et. al. utilized the vehicle

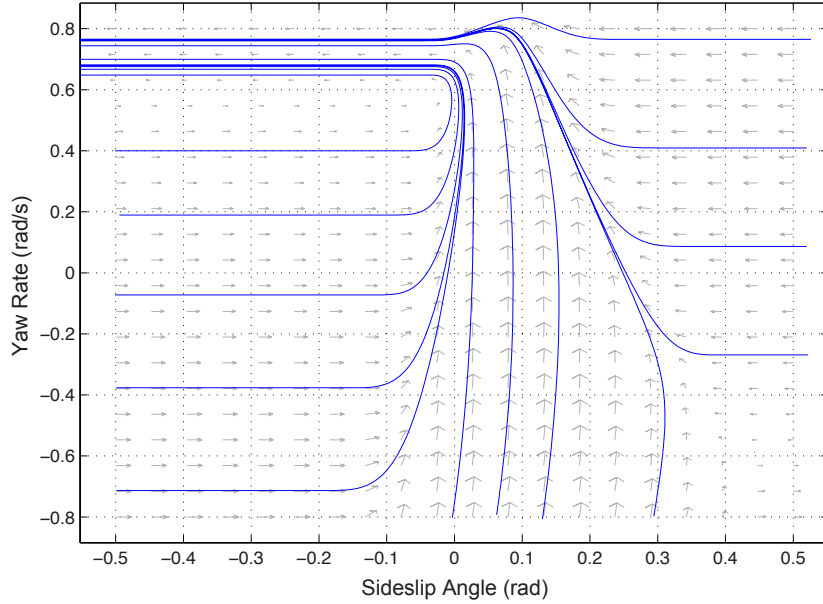


Figure 1.3: Vehicle Instability in the Yaw-Sideslip Phase Plane at  $10^\circ$  Steering

sideslip angle and its derivative as the quantities of interest, rather than the more instructive and directly measurable yaw rate. Shibahata, et. al. also examined the vehicle stability problem, concluding that the sideslip angle is a key quantity in the unstable vehicle dynamics, but this work also underestimates the value of the yaw rate information [59]. Ohno, et. al., do in fact examine the dynamics in the yaw-sideslip phase plane, but consider yaw rate as a control objective rather than an indicator of instability [50]. Chapter 3 of this dissertation presents a yaw-sideslip phase plane analysis that demonstrates that yaw rate is a key indication of the onset of instability. Because this yaw rate is built up before the sideslip angle grows, as seen in Figure 1.3, the yaw rate provides an earlier warning of instability and an opportunity to use a reliable and readily available measurement for control.

There have been several other approaches presented that utilize alternative graphical visualizations to describe the extents of the vehicle handling envelope. The Milliken Moment Method and the g-g diagram are two such approaches. The Milliken Moment Method [47] is a technique in which the lateral acceleration and a normalized yaw moment are computed over a wide range of steering and sideslip angles.

When plotted, these points fill in the interior of a parallelogram in this  $C_n - A_y$  plane, indicating all of the possible operating points of the vehicle. The edges of this parallelogram are formed by the inability of the vehicle to achieve larger lateral accelerations or yaw moments due to saturations of the front and rear axles. The distance from the operating to the boundary of the can be used to gain a sense of stability, as demonstrated in [30]. Hoffman, et. al. demonstrate the relationship of this work to the open-loop analysis of the vehicle in the phase plane and argue that the proximity to tire saturation is more informative when considering the vehicle under control of a drive. However, the point-by-point computational nature and the reliance on sideslip angle as an input present challenges in utilizing the method for real-time control of a vehicle.

The g-g diagram, as described in [55], also uses a graphical representation to illustrate the vehicle performance. The g-g diagram describes an elliptical boundary of the vehicle performance in terms of the maximum possible lateral and longitudinal accelerations at the vehicle CG. These accelerations may be estimated from the friction coefficient and the tire forces, but the method leaves out the rotational dynamics of the vehicle and any sense of the driver input and therefore cannot describe the understeer and oversteer situations that a driver assistance system would intervene to correct. Therefore, while helpful for characterizing the maximum extents of the vehicle performance, these methods are less suitable for the design of a controller for vehicle stabilization.

### 1.3 Dissertation Contributions

This dissertation describes a complete driver assistance system based on real-time estimates of state and friction information that provides progressive and smooth control action through the use of a model predictive controller. Six unique contributions form the critical concepts that allow this controller to function properly, and a seventh contribution is developed by extending the work to the roll dynamics of the vehicle.

### 1.3.1 Instability Analysis and Criteria for Safe Handling

Important issues in developing a driver assistance system are determining when to intervene and how much assistance the driver needs. This dissertation presents an analysis of vehicle instability by looking at the unstable dynamics that appear in the yaw-sideslip phase plane. It can be seen from this analysis that the yaw rate is an early indicator of instability since the sideslip dynamics become distinctly unfavorable at excessive yaw rates. Moreover, the location in the phase plane in which the unfavorable dynamics appear can be consistently located with simple, physically-motivated quantities across a wide range of vehicle speeds, steering inputs, vehicle handling characteristics, and friction coefficients.

Drawing upon the insights gained from the phase-plane analysis, a new framework for the control of vehicle instabilities is presented. This approach assumes a measurement or accurate estimate of the sideslip can be obtained and that the tire-road friction coefficient can be roughly estimated. A set of boundaries can be derived from this information to form a handling envelope in which the vehicle dynamics are stable and predictable. This envelope also allows the driver significant freedom to access driving regimes that might otherwise be disallowed by conventional stability control systems.

### 1.3.2 Envelope Control for Enforcing Envelope Boundaries

The control task of enforcing the boundaries of the handling envelope is well-matched to the structure of model predictive control, since at each time step, the controller action is the solution to an optimization problem. The optimization framework provides for incorporating both an objective as well as constraints. Taken in the context of the stabilization problem, the objective can be leveraged to express the driver's intended vehicle behavior while the constraints represent the physical limitations of the vehicle. Therefore, the controller responds as desired, allowing the driver full freedom to control the vehicle away from the boundaries but providing the necessary assistance to prevent the vehicle from exiting the safe handling envelope. Using the boundaries described previously, the model predictive control scheme provides refined

control action at the boundaries of the envelope.

A major challenge in developing a model predictive control for the task of controlling the vehicle at the handling limits is describing the vehicle dynamics in a model that is both rich enough to describe the vehicle behavior and yet simple enough to perform the optimization required for model predictive control. The Affine Force-Input (AFI) model, introduced in this dissertation, represents the key tire nonlinearity and yet is simple enough to allow for calculation of the model predictive control input in less than a few milliseconds.

### 1.3.3 Guarantees of Vehicle Behavior under Envelope Control

The AFI model used to develop the model predictive controller described in this dissertation is convex. Using this model and a combination of convex constraints, there exists a unique solution to the optimization problem at every point and fast embedded convex optimization techniques can be applied. Leveraging the convexity of the problem allows for a pair of proofs that demonstrate that the model predictive envelope controller maintains the vehicle within the invariant handling envelope and that it attracts the vehicle to the envelope in the event that disturbances push the vehicle outside the envelope boundaries.

### 1.3.4 Integration of Real-Time Friction Estimation

In the implementation of the envelope controller, the boundaries of the safe handling envelope are calculated in real-time in response to changes in vehicle speed, drive and braking torques, and tire-road friction coefficient. The sideslip state and friction coefficient estimates needed for control are provided by a real-time friction estimation scheme originally introduced by Hsu and Gerdes [32] and refined for practical use in this dissertation.

Along with the real-time friction estimation, there are significant challenges in developing a model predictive controller to operate in real time at 100Hz. This

dissertation describes the implementation of one such controller and demonstrates experimental results obtained in operation of a steer-by-wire test vehicle.

### 1.3.5 Extension of Envelope Control to Roll Dynamics

The model predictive control concept used to stabilize the planar dynamics of the vehicle in conjunction with the human driver can also be extended to the roll dynamics of the vehicle. For vehicles where the center of gravity is located significantly above the ground, the model predictive control approach may be used to alter the vehicle dynamics to control the vehicle roll and prevent deadly rollover crashes.

## 1.4 Dissertation Outline

This dissertation presents the development, analysis, and validation of the model predictive envelope control system that has been introduced in this chapter. The remaining chapters are organized as follows:

### *Chapter 2: Vehicles and Modeling*

The first portion of Chapter 2 describes the models of the vehicle that are used throughout the dissertation. These models vary in complexity and are used for various parts of the control design as well as simulation of the vehicle dynamics. The Affine Force-Input model, developed in this chapter, is a critical concept needed for use in the model predictive envelope controller. The second part of this chapter introduces the P1 test vehicle and testing surface used to validate the control design.

### *Chapter 3: Unstable Vehicle Dynamics*

In Chapter 3, a phase-plane analysis is presented to illustrate the dynamics of the vehicle that can lead to unstable responses in the sideslip and yaw dynamics. Phase portraits for neutral steering, understeering, and oversteering vehicles are included with various speeds and driver input. Across a wide range of vehicles and conditions, the unstable and undesirable dynamics appear in a clearly defined and consistent region, giving motivation for choosing a set of handling boundaries that keep the

vehicle from entering these undesirable handling regimes.

### ***Chapter 4: Model Predictive Envelope Control***

With the understanding of the unstable dynamics of the vehicle obtained from the analysis in the previous chapter, Chapter 4 describes a model predictive envelope controller that eliminates the unstable handling regions from the phase plane, yet allows the driver to have complete freedom to control the vehicle within boundaries of the safe handling region. Along with the description of the controller, experimental results are presented to demonstrate the efficacy of the controller and a pair of proofs show that the controller attracts the vehicle to the interior of the envelope and maintains it in the envelope in the absence of disturbances.

### ***Chapter 5: Friction Estimation***

The complete model predictive envelope controller must have the capability to adjust the safe handling envelope in response to changing driving conditions. Some of these changes are easy to incorporate, since it is straightforward to measure and include the effects of changing vehicle speed or driver input. However, the tire-road friction coefficient and the vehicle sideslip angle are not readily measured and must therefore be estimated. Chapter 5 reviews the fundamental concepts of the estimation technique utilized to obtain these two quantities. The chapter then describes the challenges associated with implementing the estimator to inform the model predictive controller, particularly in situations with significant variability in surface conditions. The chapter concludes with results from experimental testing that demonstrate the viability of the coupled estimation and control scheme.

### ***Chapter 6: Extensions of Model Predictive Control***

The previous chapters of the dissertation address the control of planar vehicle dynamics. Chapter 6 utilizes the model predictive control framework developed for planar envelope control and extends it to the control of the roll states. Since the body roll motion of the vehicle is excited only by the planar motions of the vehicle, prediction of the roll states using a model offers a straightforward method of linking the body roll motion to control actions on the vehicle chassis. The use of a set

constraints on the safe roll states together with an objective function that describes the driver intent is drawn directly from the concepts in previous chapters and provides good control over the roll behavior of the vehicle.

### ***Chapter 7: Conclusions***

The dissertation concludes with an evaluation of the model predictive envelope control system presented in the previous chapters. Discussion of viability for implementation in production systems is included along with possibilities for future development of the system.

# Chapter 2

## Vehicles and Models

The estimation and envelope control systems presented in this dissertation take advantage of several different models of the dynamics of the vehicle. While it is possible to model all of the degrees of freedom associated with the vehicle, the models presented here represent the critical dynamics while reducing the complexity for analytical use, practical computational concerns, or transparency. The models can take on the properties of many vehicles, but in this work, the parameters are taken from P1, a drive-by-wire test vehicle used for the validation of the envelope controller. The latter sections of this chapter describe P1 and the testing conditions used for validation.

### 2.1 Pneumatic Tires

The modern automobile tire is a complicated product; it is a composite of various rubber compounds, steel and often kevlar and the design has been refined through decades of development. Tread patterns may be highly specialized for removing water from between the tire and road or for gripping on snow and ice. The rubber itself may be sticky for maximum grip or hard for longevity. Furthermore, the inflation pressure and wear on a tire also affect the manner in which it generates force. While these and other factors affect the handling of the vehicle, consideration of all of them is prohibitively complex. Therefore, models of the tires that capture the most important effects are used in this dissertation.

### 2.1.1 Brush Tire Model

There are many choices of tire models, including those that consider many of the details of the tire construction through finite element analysis [27, 38, 61, 67, 21], and others that base the model on experimental data, such as with the popular “Magic Tire Formula” by Pajecka [52, 51]. A third group of tire models also exists, which utilizes a physical model of a tire carcass and ring with brushes attached to it. A variety of assumptions may be made in developing these brush models, including the contact patch shape and vertical pressure distribution, brush elements, model of friction interaction between the brushes and the road, and the tire band and carcass models [18, 24, 20, 6].

The brush model used in this dissertation is much like that developed by Fromm [24], with a rectangular contact patch, a parabolic pressure distribution, and rigid carcass and ring models. However, unlike the model by Fromm, this model allows for separate peak and sliding friction coefficients.

The brush model utilizes the concepts of force demand and force availability to determine the total force developed in the portion of the tire in contact with the road, typically referred to as the contact patch. When cornering, the brushes representing the rubber at the front of the contact patch are unstressed as this rubber is just beginning to come into contact with the road. However, at the back of the contact patch, the brushes are highly stressed since the wheel moves laterally throughout the period in which the rubber is in contact with the surface. Since the stress in the brushes is proportional to the displacement of the wheel over the time period from first contact, the distribution of stress throughout the contact patch increases at the angle between the lateral and longitudinal wheel velocities. Thus, the tire force demand increases linearly with this tire slip angle, as seen in Figure 2.1.

However, the amount of force available to keep the brushes stuck to the road is limited by the normal load and surface friction coefficients. While the friction coefficients are assumed to be constant throughout the contact patch, the normal load in this brush model is assumed to be parabolic. The result is a pair of parabolic distributions of available adhesion and sliding friction force. Therefore, the force demand and force availability curves are mismatched, and where the demand exceeds the available

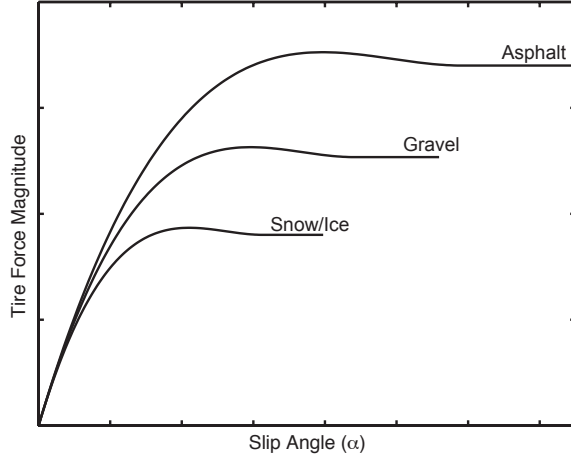


Figure 2.1: Tire Curve - Two Coefficient Brush Model

friction, the brushes in that portion of the contact patch slide, producing force equivalent to the maximum sliding friction. The amount of the contact patch that slides increases as the slip angle grows until the tire is completely sliding. This progression is illustrated in Figure 2.2, where the shaded regions represent the resultant force distribution. The effects are also seen in Figure 2.1, where the curves progressively drop away from the initial linear slope as more of the contact patch slides. Note also in Figure 2.1 that the tire behaves identically at low slip angles, regardless of the friction coefficient, since the force is initially dependent only on the brush deflections where the force demand does not exceed the available friction.

The variation of the distribution of force in the contact patch has a secondary effect as well. As the tire begins to slide, the centroid of the force distribution changes. Because the distributed force effectively acts at this point and the steering axis is usually located closer to the center of the contact patch, a moment is created by the lateral force. This is often referred to as the “aligning moment” since it tends to restore the wheel to a straight-ahead orientation. As the tire begins to saturate, the centroid of the force moves closer to the steering axis and this aligning moment decreases. Highly skilled drivers feel this in the steering system and can use it to sense the friction limits. The friction estimation technique presented in Chapter 5 leverages this effect in a similar manner.

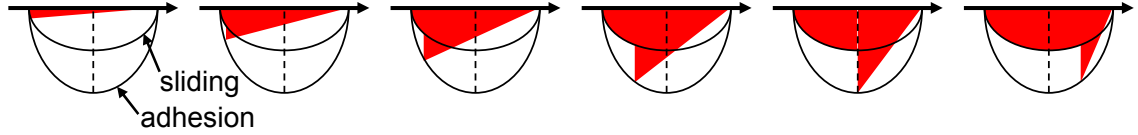


Figure 2.2: Force Distribution in the Contact Path

Written in mathematical form, the model is parameterized by the linear cornering stiffness ( $C_\alpha$ ), the peak force ( $\mu F_z$ ), and the ratio of the sliding friction coefficient to the peak coefficient ( $R_\mu$ ). The relationship between the slip angle and the tire force is given by the following expression if the tire is operating at a slip angle equal to or less than the angle of full sliding:

$$F_y = -C_\alpha \tan \alpha + \frac{C_\alpha^2}{3\mu F_z} (2 - R_\mu) \tan \alpha |\tan \alpha| - \frac{C_\alpha^3}{9(\mu F_z)^2} \left(1 - \frac{2}{3} R_\mu\right) \tan^3 \alpha. \quad (2.1)$$

The angle of full sliding is

$$\alpha_{\text{slide}} = \frac{3\mu F_z}{C_\alpha} \quad (2.2)$$

and can be found analytically using the assumed parabolic pressure distribution and triangular force demand on the tire. Once beyond this angle, the tire force is assumed to be equal to

$$F_y = \mu_s F_z, \quad (2.3)$$

the maximum sliding friction force. Since the tire force equation is a cubic polynomial in  $\tan \alpha$  once the sign of  $\tan \alpha$  is known, it is possible to reverse the relationship and calculate slip angle from lateral force, but the solution is unique only if an additional assumption that the tire is operating at an angle equal to or below the slip angle corresponding to peak force is added. This reverse relationship is used later in this dissertation to find a steering angle to produce a desired lateral force. Therefore, the minimum slip angle assumption is justified since the front axle operating point is a control variable and will be chosen between the positive and negative peak slip angles. In addition to the reverse mapping, a relationship for local cornering stiffness may be derived from the force model by direct differentiation.

Several explicit relationships also may be derived for a tire at the angle of peak force generation. The resulting equations (used in developing the control strategy in the following sections) are:

$$q = \left(1 - \frac{2}{3}R_\mu\right)^{-1} \quad (2.4a)$$

$$F_{y_{\text{peak}}} = \mu F_z \left(-q + \frac{2 - R_\mu}{3}q^2 - \frac{1 - \frac{2}{3}R_\mu}{9}q^3\right) \quad (2.4b)$$

$$\alpha_{\text{peak}} = \arctan\left(\frac{q\mu F_z}{C_\alpha}\right). \quad (2.4c)$$

where  $F_{y_{\text{peak}}}$  is the maximum achievable tire force, and  $\alpha_{\text{peak}}$  is the tire slip angle at which the maximum tire force is attained.

The brush tire model also provides a mechanism for including the effects of lateral-longitudinal force coupling. In general, the force demand on a tire is a vector sum of the lateral and longitudinal components and must be less than the total available force,

$$F_{\text{tot}} = \sqrt{F_x^2 + F_y^2} \leq \mu F_z. \quad (2.5)$$

A rigorous treatment of this elliptical force limitation on each tire requires that the rotational dynamics of the tires be modeled. With these rotational dynamics, the longitudinal slip on the tire can be calculated and the combined slip may be used to calculate the coupled forces,  $F_x$  and  $F_y$ , on each axle. Longitudinal slip is defined as the difference between the free rolling velocity and actual rotational speed of each wheel, and can be written

$$\kappa = \frac{\omega R_w - V_{x_{\text{wheel}}}}{V_{x_{\text{wheel}}}} \quad (2.6)$$

where  $\omega$  is the wheel rotational speed,  $R_w$  is the effective rolling radius, and  $V_{x_{\text{wheel}}}$  is the longitudinal velocity of the wheel center. The longitudinal slip is analogous to the lateral slip angle of the tire and the two equations for lateral and longitudinal forces have a common form. Thus, it is possible to combine these equations using the friction circle concept to yield coupled equations for the lateral and longitudinal tire

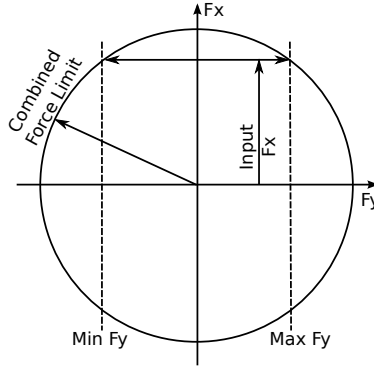


Figure 2.3: Combined Tire Force Limits

forces:

$$\gamma = \sqrt{C_x^2 \left( \frac{\kappa}{1 + \kappa} \right)^2 + C_\alpha^2 \left( \frac{\tan \alpha}{1 + \kappa} \right)^2} \quad (2.7a)$$

$$F = \begin{cases} \gamma - \frac{1}{3\mu F_z} \left( 2 - \frac{\mu_s}{\mu} \right) \gamma^2 + \frac{1}{9\mu^2 F_z^2} \left( 1 - \frac{2\mu_s}{3\mu} \right) \gamma^3 & \gamma \leq 3\mu F_z \\ \mu_s F_z & \gamma > 3\mu F_z \end{cases} \quad (2.7b)$$

$$F_x = \frac{C_x}{\gamma} \left( \frac{\kappa}{1 + \kappa} \right) F \quad (2.7c)$$

$$F_y = \frac{-C_\alpha}{\gamma} \left( \frac{\tan \alpha}{1 + \kappa} \right) F. \quad (2.7d)$$

However, the wheel dynamics are significantly faster than the chassis dynamics that are pertinent for envelope control. They also add quite a bit of complexity to the model. Therefore, for the model predictive control problem, an approximation of this behavior is made by treating the  $F_x$  demand as an input that dictates the maximum available  $F_y$  force, as illustrated in Figure 2.3. This “derating” approach can be expressed as

$$\mu F_z = \sqrt{(\mu F_z)_{\text{nom}}^2 - F_x^2} \quad (2.8)$$

and the adjusted value of  $\mu F_z$  can be used as a parameter for the lateral brush tire model to yield an approximate coupled tire force. For longitudinal forces significantly smaller than  $(\mu F_z)_{\text{nom}}$ , this is a relatively good model, but the lack of longitudinal slip

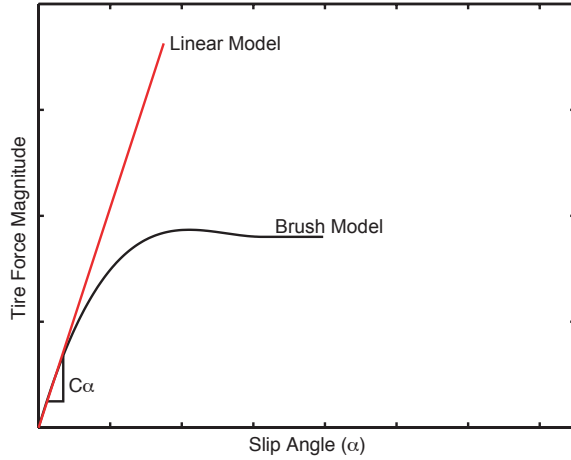


Figure 2.4: Comparison of Linear and Brush Tire Models

information makes the relationship incomplete. If this method is applied naively with very large longitudinal forces, the lateral force may be reduced to zero. Therefore, for use in the envelope control system,  $\mu F_z$  is bounded away from zero to improve the model performance.

### 2.1.2 Linear Tire Model

For some tasks described in this dissertation, the brush tire model is more detailed than necessary. At low levels of lateral acceleration with respect to the maximum on the surface, a linear model describes the tire forces well and provides a useful way to develop a linear version of bicycle model. The linear tire model yields the following expressions for the front and rear tire forces,

$$F_{yf} = -C_{\alpha_f} \alpha_f, \quad F_{yr} = -C_{\alpha_r} \alpha_r \quad (2.9)$$

where  $\alpha_f$  and  $\alpha_r$  are described in terms of the vehicle states and the steering angle input from the driver.

Despite the complex construction of tires and the influence of stick-slip friction, their behavior at low levels of lateral force is dominated by the elastic nature of the rubber. Therefore, this linear model of the tire forces yields good results up to

approximately half of the maximum tire force as seen in Figure 2.4.

## 2.2 Chassis Models

### 2.2.1 Four Wheel Yaw-Roll Model

The most complex model of the vehicle dynamics used in this dissertation is represented in Figure 2.5. The four wheels of the vehicle are connected to each other by a rigid base, while the body of the vehicle is represented by an inverted pendulum that rolls about an imaginary axis connecting the front and rear of the vehicle. Rotational states for all four wheels are included, weight transfer between the wheels is calculated, and the coupled lateral-longitudinal brush tire model is used to calculate the forces on each tire. The effects of the suspensions are incorporated into the roll motion of the inverted pendulum and the weight transfer between the wheels, making this a relatively complete description of the vehicle behavior. The equations for the yaw, roll, and sideslip derivatives of the vehicle are:

$$m\dot{U}_x - mrU_y + mh'\dot{r}\sin\phi + 2mh'r\dot{\phi}\cos\phi = Q_x \quad (2.10a)$$

$$m\dot{U}_y + mrU_x - mh'\ddot{\phi}\cos\phi + mh'\left(r^2 + \dot{\phi}^2\right)\sin\phi = Q_y \quad (2.10b)$$

$$\dot{r} = \frac{Q_\psi - Q_xh'\sin\phi - 2(I_{yy} - I_{zz})r\dot{\phi}\sin\phi\cos\phi}{I_{yy}\sin^2\phi + I_{zz}\cos^2\phi} \quad (2.10c)$$

$$\ddot{\phi} = \frac{Q_yh'\cos\phi - K_\phi\phi - b_\phi\dot{\phi} + mgh'\sin\phi + \left[(I_{yy} - I_{zz})r^2 - mh'^2\dot{\phi}^2\right]\sin\phi\cos\phi}{I_{xx} + mh'^2\sin^2\phi} \quad (2.10d)$$

$$Q_x = (F_{xlf} + F_{xrf})\cos\delta - (F_{ylf} + F_{yrf})\sin\delta + F_{xlr} + F_{xrr} \quad (2.10e)$$

$$Q_y = (F_{ylf} + F_{yrf})\cos\delta + (F_{xlf} + F_{xrf})\sin\delta + F_{ylr} + F_{yrr} \quad (2.10f)$$

$$Q_\psi = a[(F_{ylf} + F_{yrf})\cos\delta + (F_{xlf} + F_{xrf})\sin\delta] - b[F_{ylr} + F_{yrr}] - \frac{d}{2}[(F_{xlf} - F_{xrf})\cos\delta - (F_{ylf} - F_{yrf})\sin\delta + F_{xlr} - F_{xrr}] \quad (2.10g)$$

where  $I_{xx}$ ,  $I_{yy}$ ,  $I_{zz}$ , are the moments of inertia about the x, y, and z axes, respectively. Products of inertia are assumed to be zero in this model, though the equations for a

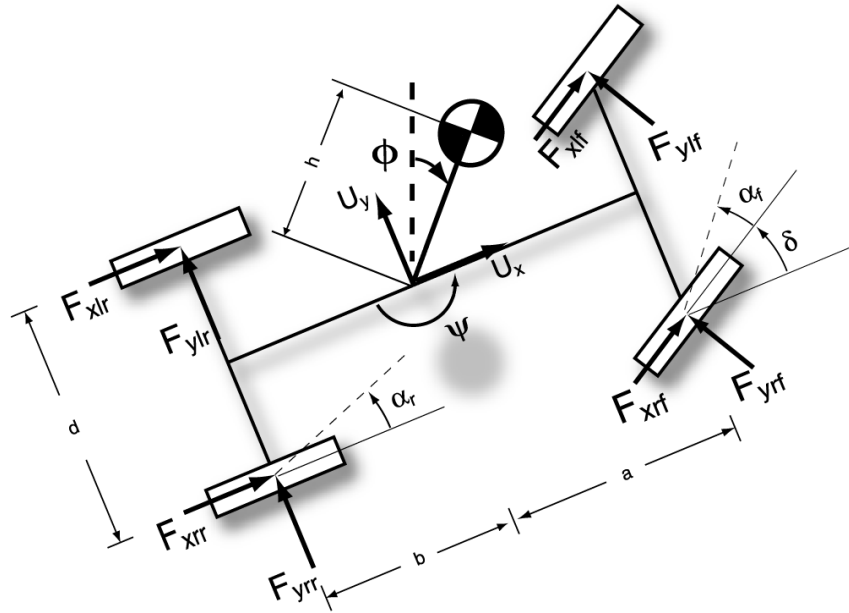


Figure 2.5: Four-wheel Yaw-Roll Model

similar model with non-zero yaw-roll product of inertia may be found in [40].

The four wheel yaw-roll model was used as a virtual testbed to validate the design of the envelope controller before experiments were performed and provides the basis for the investigation of vehicle roll control as described in Chapter 6. Perhaps more importantly, by making certain assumptions about the vehicle state, the four wheel yaw-roll may be reduced to a variety of other useful and less complicated models.

### 2.2.2 Bicycle Model

The bicycle model, shown in Figure 2.6, is a two-state model of the vehicle dynamics that yields a pair of equations that describe the rotational and lateral velocities of the vehicle. This description of the planar vehicle dynamics is used in the development of the model predictive envelope controller.

Several key assumptions are made in reducing the yaw-roll model to the bicycle model. Since the bicycle model is used to describe the planar behavior of the vehicle, the body roll behavior is neglected by assuming that the mass of the vehicle is entirely

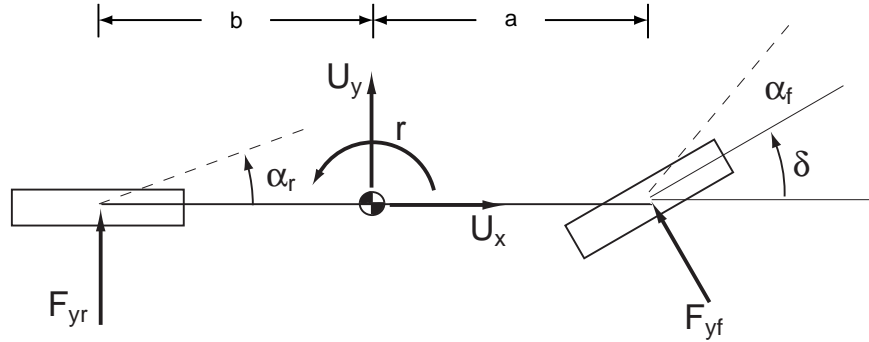


Figure 2.6: The Bicycle Model

in the rigid base of the vehicle. Furthermore, for traversing corners of moderate radius at typical driving speeds, the left and right wheels on each axle attain nearly identical slip angles. Therefore, the forces from the wheels on each axle are summed and lumped together as a single equivalent wheel. However, it is well known that lateral weight transfer and suspension deflections also result in differences between the left and right wheels. These effects are incorporated into the model through the use of lumped parameters that are identified from the car in experimental testing. The cornering stiffness allows the linear tire model to incorporate these effects while the measured peak force on each axle informs the nonlinear brush tire model.

For the purposes of friction estimation and envelope control, a constant longitudinal velocity is assumed. However, it is noted that accelerating and braking torques and longitudinal weight transfer play a significant role in determining the lateral behavior of the vehicle. Fortunately, these influences on the lateral tire forces may be approximated separately and are included where necessary to achieve sufficient accuracy in the lateral dynamics.

The equations of motion for the bicycle model are developed from first principles by writing a force balance in the vehicle  $y$ -coordinate and a moment balance around the  $z$ -axis, also known as the yaw axis.

$$ma_y = F_{yf} + F_{yr}, \quad \dot{r}I_{zz} = aF_{yf} - bF_{yr} \quad (2.11)$$

The lateral acceleration of the vehicle in an inertial reference frame is

$$a_y = \dot{U}_y + rU_x \quad (2.12)$$

and small angles are assumed to obtain a linear approximation for the sideslip angle

$$\beta = \tan^{-1} \left( \frac{U_y}{U_x} \right) \text{ to } \beta = \frac{U_y}{U_x}. \quad (2.13)$$

Using these expressions for lateral acceleration and sideslip angle, Eq. 2.11 can be rearranged to find state equations for the sideslip angle and yaw rate:

$$m \left( \dot{U}_y + rU_x \right) = F_{yf} + F_{yr} \quad \dot{r}I_{zz} = aF_{yf} - bF_{yr} \quad (2.14)$$

$$\dot{\beta} = \frac{F_{yf} + F_{yr}}{mU_x} - r \quad \dot{r} = \frac{aF_{yf} - bF_{yr}}{I_{zz}} \quad (2.15)$$

where the parameters  $m$  and  $I_{zz}$  are the vehicle mass and yaw moment of inertia, respectively.

The forces,  $F_{yf}$  and  $F_{yr}$ , are generated by the tires at each axle and are highly nonlinear at elevated levels of lateral acceleration. Therefore, the nonlinear brush model may be used to describe their force generating characteristics. However, at low levels of lateral acceleration, the linear model describes the tire forces well and provides a useful way to develop a completely linear version of bicycle model. Like the sideslip angle of the vehicle, small angles are assumed to get linear expressions for the axle slip angles:

$$\alpha_f = \beta + \frac{ar}{U_x} - \delta, \quad \alpha_r = \beta - \frac{br}{U_x}. \quad (2.16)$$

The driver input,  $\delta$ , is also included through these slip angle expressions. Substitution of these slip angles into the linear tire force equations (Eq. 2.9) and then into the state equations in Eq. 2.15 yields a pair of differential equations that specify the behavior of the two states when the driver input is known. This system can be written in

state-space form as  $\dot{x} = Ax + B\delta$  with  $x = [\beta \ r]^T$  and

$$A = \begin{bmatrix} \frac{-(C_{\alpha f} + C_{\alpha r})}{mU_x} & \frac{-(aC_{\alpha f} - bC_{\alpha r})}{mU_x^2} - 1 \\ \frac{-(aC_{\alpha f} - bC_{\alpha r})}{I_{zz}} & \frac{-(a^2C_{\alpha f} + b^2C_{\alpha r})}{I_{zz}U_x} \end{bmatrix}, \quad B = \begin{bmatrix} \frac{C_{\alpha f}}{mU_x} \\ \frac{aC_{\alpha f}}{I_{zz}} \end{bmatrix}. \quad (2.17)$$

While this model is not sufficiently accurate in the nonlinear regions of the state space to be used for control, it is used to perform state estimation when the vehicle operates in the linear regions. The model is also used in Section 4.1.3 as a reference model of the driver's intent, as it is assumed that drivers will readily accept and understand a vehicle that follows a linear response.

### 2.2.3 Affine Force-Input Model

The nonlinear brush tire model may be used to model the front and rear axle forces for the bicycle model and the resulting equations of motion provide a very good description of the planar vehicle motion. Unfortunately, both the solve time and the risk of emergent solutions grow rapidly with increased model complexity. To preserve the ability to calculate the solution to the model predictive control problem in real time at 100Hz, the underlying model for the controller must be simplified.

The Affine Force-Input (AFI) model describes the same states and is based on the same small angle, lumped-axle, and constant speed assumptions as the bicycle model depicted in Figure 2.6. The AFI model is also derived from the same equations of motion as the bicycle model, given in Eqs. 2.15, with a few key differences. In contrast to the bicycle model, the front lateral force,  $F_{yf}$ , is the input rather than substituting the front slip angle into the model and using the steering angle,  $\delta$ . This is a critical choice as it preserves the linear relationship between the input and the model states. The tire model described in Section 2.1.1 describes the relationship between the steering angle and front force and can be used outside of the AFI model to convert between the two quantities.

The nonlinearities of the rear axle also must be handled. Because the lateral force on the rear axle cannot be directly controlled like the front lateral force in this representation of the dynamics, the rear force,  $F_{yr}$ , is dependent upon the vehicle states.

Therefore, to represent the link between the vehicle motion and the rear tire force, the brush tire model is linearized about the slip angle operating point. This linearization is found by taking the zeroth and first-order terms of the Taylor expansion of a smooth tire model, from which the tire force,  $\bar{F}_{yr}$  and the local cornering stiffness,  $\tilde{C}_{\alpha_r}$  can be found at the operating point,  $\bar{\alpha}_r$ .

$$F_{yr} = \bar{F}_{yr} - \tilde{C}_{\alpha_r} (\alpha_r - \bar{\alpha}_r) \quad (2.18)$$

This rear tire force equation is affine in the rear slip angle  $\alpha_r$ , which provides a representation of the saturation behavior of the tire without including a nonlinear expression. Substituting Eq. 2.18 into Eq. 2.15 yields:

$$\dot{\beta} = \frac{F_{yf} + \bar{F}_{yr} - \tilde{C}_{\alpha_r} (\alpha_r - \bar{\alpha}_r)}{mU_x} - r \quad (2.19a)$$

$$\dot{r} = \frac{aF_{yf} - b [\bar{F}_{yr} - \tilde{C}_{\alpha_r} (\alpha_r - \bar{\alpha}_r)]}{I_{zz}}. \quad (2.19b)$$

Like the bicycle model, small angle assumptions allow the rear slip angle to be written  $\alpha_r = \beta - \frac{b}{U_x}r$ , which yields

$$\dot{\beta} = \frac{F_{yf} + \bar{F}_{yr} - \tilde{C}_{\alpha_r} \left( \beta - \frac{b}{U_x}r - \bar{\alpha}_r \right)}{mU_x} - r \quad (2.20a)$$

$$\dot{r} = \frac{aF_{yf} - b [\bar{F}_{yr} - \tilde{C}_{\alpha_r} \left( \beta - \frac{b}{U_x}r - \bar{\alpha}_r \right)]}{I_{zz}}. \quad (2.20b)$$

A state-space description of the system needed for use in the model predictive control problem can be defined as  $\dot{x} = Ax + BF_{yf} + d$ , where again  $x = [\beta \ r]^T$  with

$$A = \begin{bmatrix} -\frac{\tilde{C}_{\alpha_r}}{mU_x} & \frac{b\tilde{C}_{\alpha_r}}{mU_x^2} - 1 \\ \frac{b\tilde{C}_{\alpha_r}}{I_{zz}} & -\frac{b^2\tilde{C}_{\alpha_r}}{U_x I_{zz}} \end{bmatrix}, \quad B = \begin{bmatrix} \frac{1}{mU_x} \\ \frac{a}{I_{zz}} \end{bmatrix}, \quad d = \begin{bmatrix} \frac{(\bar{F}_{yr} + \tilde{C}_{\alpha_r} \bar{\alpha}_r)}{mU_x} \\ \frac{-b(\bar{F}_{yr} + \tilde{C}_{\alpha_r} \bar{\alpha}_r)}{I_{zz}} \end{bmatrix}. \quad (2.21)$$

The resulting model satisfies the requirements for convexity and allows for the use of efficient optimization techniques when implementing the model predictive controller.

### 2.2.4 Linearized Roll Model

When extending the model predictive envelope controller to control vehicle roll, there is no direct actuation of the roll states and any roll motion is excited solely by the planar motion of the vehicle. Therefore, it is critical for the model to describe the planar dynamics as well as the mechanism for transferring energy into the roll modes of the vehicle. At the same time, the model must be simple enough to underly a model predictive control scheme.

The compromise between modeling complexity and solve speed for the MPC problem is handled by linearizing the equations of motion for the yaw roll model, neglecting the rotational dynamics of the wheels, and utilizing a linear model to produce the tire forces. All four wheels are included for the purposes of incorporating differential drive, but the lateral forces are calculated with a common axle slip angle for the left and right wheels. As with the other models, small angles and a constant vehicle velocity are assumed.

The state variables selected to represent the base mode of the vehicle are the yaw rate about the body pivot point and the vehicle slip angle between the vehicle velocity at the pivot point and the vehicle heading. For the roll mode, the states are the angle and rotation rate of the pendulum about the pivot point. There are also three inputs to the model: front steering angle, rear steering angle, and rear differential drive. The roll controller presented later in this dissertation takes advantage of these multiple actuators to achieve the desired vehicle states. To incorporate the rear wheel steering, the rear slip angle is redefined to include the extra input:

$$\alpha_r = \frac{Uy - ra}{Ux} - \delta_r. \quad (2.22)$$

Rear wheel differential drive may be generated by modulating the engine of a rear-wheel-drive car or the rear brake channels of a vehicle with ABS/stability control. Therefore, these inputs are represented by two longitudinal force terms in the yaw equation.

Combining these inputs with the nonlinear yaw-roll equations and linearizing, the

model can be described by the following equations:

$$F_{yf} + F_{yr} = m_s \left[ U_x (\dot{\beta} + r) - h \ddot{\phi} \right] + m_u U_x (\dot{\beta} + r) \quad (2.23a)$$

$$aF_{yf} - bF_{yr} + \frac{d}{2} (F_{xr} - F_{xl}) = I_{zz} \dot{r} \quad (2.23b)$$

$$(m_s g h - K_\phi) \phi - b_\phi \dot{\phi} + m_s h \left[ U_x (\dot{\beta} + r) - h \ddot{\phi} \right] = I_{xx} \ddot{\phi} \quad (2.23c)$$

As with the planar envelope control problem, a computationally efficient model is needed for the optimization phase of the model predictive control step. Therefore, for the roll control task, the linear tire model was selected in order phrase the problem as a quadratic program (QP), a specific type of convex optimization problem that may be solved rapidly and robustly.

The linearized equations can be rearranged to obtain the continuous time state space representation of the system that is discretized and used in the roll control investigation.

$$\begin{bmatrix} \dot{\beta} \\ \dot{r} \\ \dot{\phi} \\ \ddot{\phi} \end{bmatrix} = \begin{bmatrix} \frac{-I_{eq}C_0}{mU_x^2 I_{comb}} & \frac{-I_{eq}[C_1+mU_x^2]}{mU_x^2 I_{comb}} + \frac{m_s^2 h^2 U_x}{mU_x I_{comb}} & \frac{m_s h (m_s g h - K_\phi)}{mU_x I_{comb}} & \frac{-m_s h b_\phi}{mU_x I_{comb}} \\ \frac{-C_1}{I_{zz} U_x} & \frac{-C_2}{I_{zz} U_x} & 0 & 0 \\ 0 & 0 & 0 & 1 \\ \frac{-m_s h C_0}{mU_x I_{comb}} & \frac{-m_s h [C_1+mU_x^2]}{mU_x I_{comb}} + \frac{m_s h U_x}{I_{comb}} & \frac{(m_s g h - K_\phi)}{I_{comb}} & \frac{-b_\phi}{I_{comb}} \end{bmatrix} \begin{bmatrix} \beta \\ r \\ \phi \\ \dot{\phi} \end{bmatrix} + \begin{bmatrix} \frac{C_{\alpha f} I_{eq}}{mU_x I_{comb}} & 0 & 0 \\ \frac{a C_{\alpha f}}{I_{zz}} & \frac{d}{2I_{zz}} & -\frac{d}{2I_{zz}} \\ 0 & 0 & 0 \\ \frac{m_s h C_{\alpha f}}{mI_{comb}} & 0 & 0 \end{bmatrix} \begin{bmatrix} \delta_f \\ F_{xlr} \\ F_{xrr} \end{bmatrix} \quad (2.24)$$

## 2.2.5 Summary of Models

Table 2.1 summarizes the key features of the models that were introduced in the previous subsections.

Table 2.1: Vehicle Models

Chassis Model	Tire Model	Assumptions
Four wheel yaw-roll	Coupled brush	Vehicle body as inverted pendulum
Bicycle	Linear	No roll, small angles, lumped wheels, constant speed
Affine Force Input	Lateral brush	No roll, small angles, lumped wheels, constant speed
Linearized roll	Linear	Pendulum body, small angles, constant speed

## 2.3 P1 By-Wire Test Vehicle

The parameters used for the models described in the previous section are those of an experimental test vehicle constructed by students at Stanford University. This vehicle, referred to as P1 and shown in Figure 2.7, is a rear-wheel drive vehicle powered by independent left and right electric drive motors. P1 is also equipped with a pair of GPS systems that provide velocity and attitude information that is fused with inertial measurements to achieve high-accuracy full-state feedback at a 500Hz update rate, as described in [57]. The steering system includes independent left- and right-wheel actuation with high bandwidth response, as detailed in [40], and the handling properties of P1 are consistent with those of a sports sedan – with one important exception – and are detailed in Table 2.2.

The exception to the normal handling properties for P1 is the yaw moment of inertia. Compared to the mass, wheelbase, and track width, the moment of inertia is unusually small. In addition, the drive system of P1 provides regenerative braking on the rear axle when the driver lifts off the accelerator pedal. The combination of these properties results in the vehicle being highly sensitive to accelerator inputs by the driver while cornering. In open-loop driving with the vehicle on a low-friction surface, drivers are often unable to stabilize the vehicle in drive-torque induced oversteer.



Figure 2.7: P1 Steer and Drive By-Wire Research Testbed

Table 2.2: Parameters for the P1 test vehicle

Parameter	Symbol	Value	Units
vehicle mass	$m$	1724	$kg$
yaw moment-of-inertia	$I_{zz}$	1100	$\frac{kg}{m^2}$
wheelbase	$L$	2.5	$m$
front axle-CG distance	$a$	1.35	$m$
rear axle-CG distance	$b$	1.15	$m$
front cornering stiffness	$C_{\alpha_f}$	90000	$\frac{N}{rad}$
rear cornering stiffness	$C_{\alpha_r}$	138000	$\frac{N}{rad}$

## 2.4 Experimental Testing

For the experimental validation given in later chapters of this dissertation, tests were performed on surfaces comprised of mixed dirt, gravel, and asphalt. The friction characteristics of the surfaces were therefore highly variable. Some sections with very little loose dirt and gravel had normal adhesive friction characteristics of asphalt while other sections with a lot of gravel would allow the tires to slide quite a bit. The variation in the distribution of loose particles on the surface was estimated to have a length scale on the order of tens of centimeters and at speed, an average friction coefficient of 0.6 was a suitable estimate. In some experiments, the friction information, as well as the sideslip angle, were estimated in real time using the technique described in [32], but for many of the initial experiments with the controller, a static *a priori* estimate of the friction properties and GPS-based state estimation were used to isolate the controller behavior from any undesired estimator-controller interactions.

# Chapter 3

## Vehicle Instability

While it is well known that a vehicle may become unstable once it reaches certain states in the nonlinear regions of the tires, there has been little published previously to describe the transition of the vehicle from normal driving into the unstable handling regime. This chapter presents an analysis of the driving dynamics and demonstrates the appearance of unstable dynamics across a range of vehicles, speeds, and driver inputs.

### 3.1 Instability Dynamics

Using a two-state model, it is possible to develop phase plane representations of the vehicle dynamics in the linear and nonlinear handling regimes. These plots allow the designer of a driver assistance system to identify regions in which the dynamics are unfavorable and in which the vehicle would fail to respond in a manner that most drivers would expect. These are the regions in which production stability control systems activate to assist the driver. A driver assistance system based on handling envelopes would seek to prevent the vehicle from entering these regions at all.

The phase plots shown in this dissertation are “snapshots” of the dynamics of the vehicle model at various conditions. To obtain a reasonable level of accuracy, the dynamics are calculated from a bicycle model with nonlinear tires and no small angle assumptions. The sideslip and yaw rate states of the vehicle are plotted on the

horizontal and vertical axes, respectively. Since only two variables can be represented in these plots, all other vehicle parameters are held constant. Therefore, each plot shows the vehicle dynamics at a specific friction coefficient, vehicle speed, and driver steering angle. Inagaki, et. al. examined this yaw-sideslip plane but argued in favor of a plane with the sideslip derivative plotted against sideslip due to the location and movement of the equilibria [62]. Hoffman, et. al. utilized a similar analysis where a simulated closed loop maneuver was plotted over a three-dimensional envelope in the open loop  $\beta - \dot{\beta} - \delta$  space [30].

The first set of phase plots shown in this section illustrates the dynamics of a vehicle being driven at  $10 \frac{m}{s}$  on a surface with an average coefficient of friction of 0.6. The parameters for the vehicle are those of the P1 test vehicle, seen in Figure 2.7. This vehicle is mildly understeering in the linear region, with an understeer gradient of  $0.02 \frac{rad}{g}$ . At the handling limits, the vehicle is close to being neutral, but tends slightly to limit oversteering. The driver steering input in the set of plots progresses from  $3^\circ$  at the road wheels in Figure 3.1a up to  $12^\circ$  in Figure 3.1d.

For each phase plot in Figures 3.1a-3.1c, there are three equilibria. In these plots, the steering angles are less than or equal to  $10^\circ$  and there is a stable equilibrium on each plot at moderate yaw rate and sideslip angles. There are also two saddle points that separate regions of stable handling from unstable regions. These saddle points are located along lines of constant yaw rate, in this case at approximately  $0.59 \frac{rad}{g}$ . As the steering angle of the vehicle is increased, the stable equilibria of the vehicle move to higher yaw rates and larger (negative) sideslip angles, while the regions of instability shift, as seen by the movement of the saddle points toward lower sideslip angles. Figure 3.1d illustrates the vehicle behavior when the steering angle is increased to  $12^\circ$ . At this steering angle, the vehicle is unstable, as evidenced by a bifurcation from a stable to unstable equilibrium. Nearly all trajectories of the system result in the growth of the vehicle yaw rate followed by the vehicle sliding sideways with a large sideslip angle. Since the vehicle is nearly neutral steering, the yaw rate remains moderate during the slide.

These plots yield interesting insights for the design of stability controllers. Even though Figures 3.1a-3.1c show vehicle behaviors with stable dynamics immediately

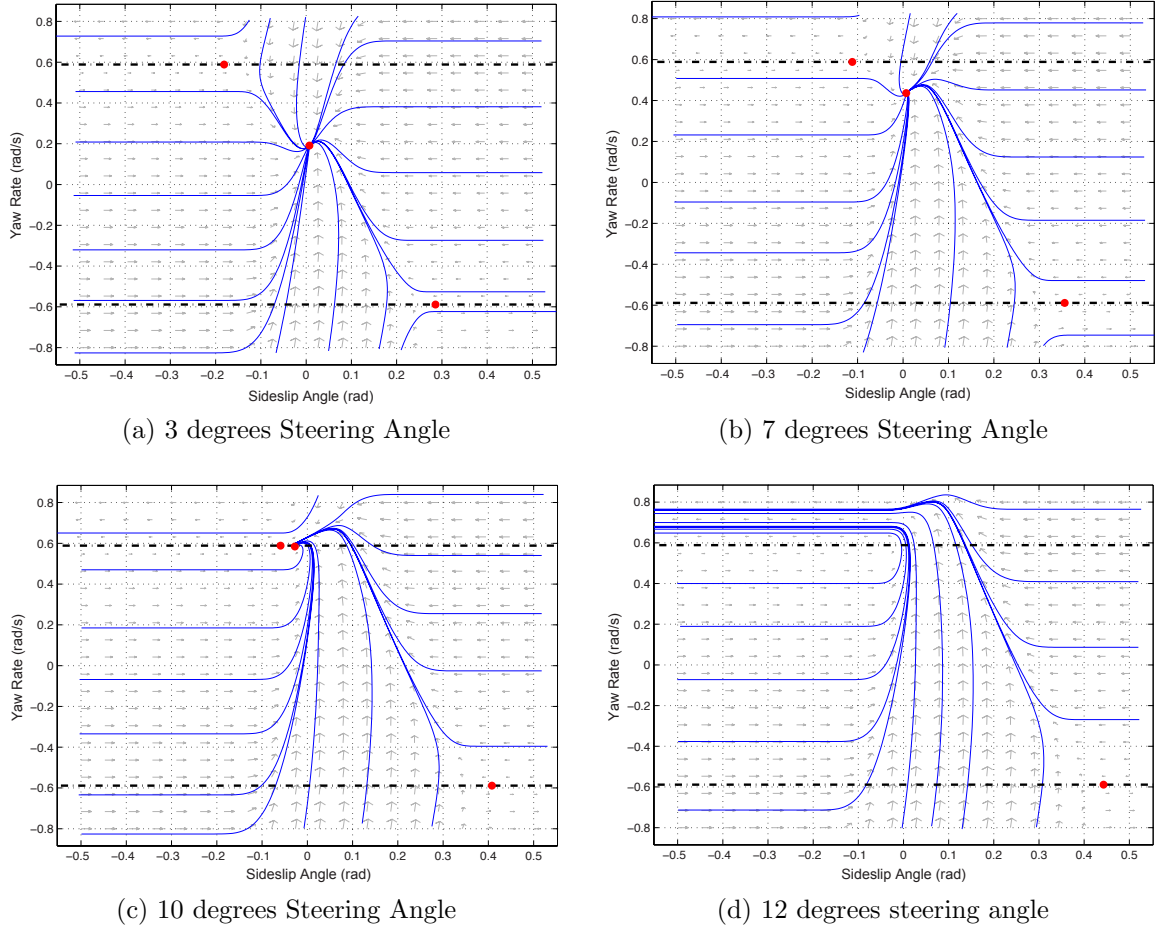


Figure 3.1: Neutral Vehicle Dynamics at 10m/s with 0.6 Surface Friction Coefficient

surrounding the equilibria, unstable regions exist for all of these conditions. Therefore, a stability control system should seek to prevent the vehicle from entering these regions in case of disturbances to the system. Fortunately, the unstable dynamics occur in the same location, regardless of the driver's steering input. The dotted black line on each of the phase plots in Figure 3.1d represents the maximum equilibrium yaw rate for the vehicle. This yaw rate may be found utilizing the maximum tire

force at each axle. The yaw rate is in equilibrium when

$$\dot{r} = \frac{aF_{yf} - bF_{yr}}{I_{zz}} = 0 \quad (3.1)$$

$$F_{yf} = \frac{b}{a}F_{yr}, \quad (3.2)$$

assuming that lateral aerodynamic forces can be neglected in the driving conditions considered in this dissertation.

With the simplified model of the lateral vehicle dynamics used in this investigation, each tire simultaneously reaches its maximum force at steady state. However, other effects such as weight transfer, suspension motions, and drive torque can cause one axle to reach saturation earlier than the other. If this occurs, one axle will limit the maximum yaw rate. If  $F_{yf_{\max}} \leq \frac{b}{a}F_{yr_{\max}}$ , then the equilibrium is dictated by the front lateral tire force. If  $F_{yf_{\max}} \geq \frac{b}{a}F_{yr_{\max}}$ , then the rear lateral tire force dictates the equilibrium. If the driver has pushed the vehicle to the equilibrium associated with the limiting tire force, then  $\dot{\beta} = 0$  and

$$r = \begin{cases} \frac{F_{yr_{\max}}(1+b/a)}{mU_x} & F_{yf_{\max}} \geq \frac{b}{a}F_{yr_{\max}} \\ \frac{F_{yf_{\max}}(1+a/b)}{mU_x} & F_{yf_{\max}} < \frac{b}{a}F_{yr_{\max}} \end{cases} \quad (3.3)$$

Therefore, this line of constant yaw rate separates the areas of convergent sideslip dynamics from the areas of divergent dynamics. Furthermore, examining Figure 3.1d, when the driver steers far enough to cause the vehicle to slide without any external disturbance, the vehicle yaw rate grows rapidly with low sideslip angles prior to exceeding the equilibrium yaw rate and developing large sideslip. This observation also makes clear the underlying reason for the efficacy of stability control through independent braking to produce a yaw moment, or what many authors term Direct Yaw Control (DYC) [43, 41]. By restricting the yaw rate from deviating significantly from a linear reference, large growth in vehicle sideslip angle can be prevented, even when direct measurements of sideslip angle are absent.

While the handling properties of the vehicle used for the phase plots in Figure 3.1 are quite neutral at the limits of handling, the observations made about the regions of

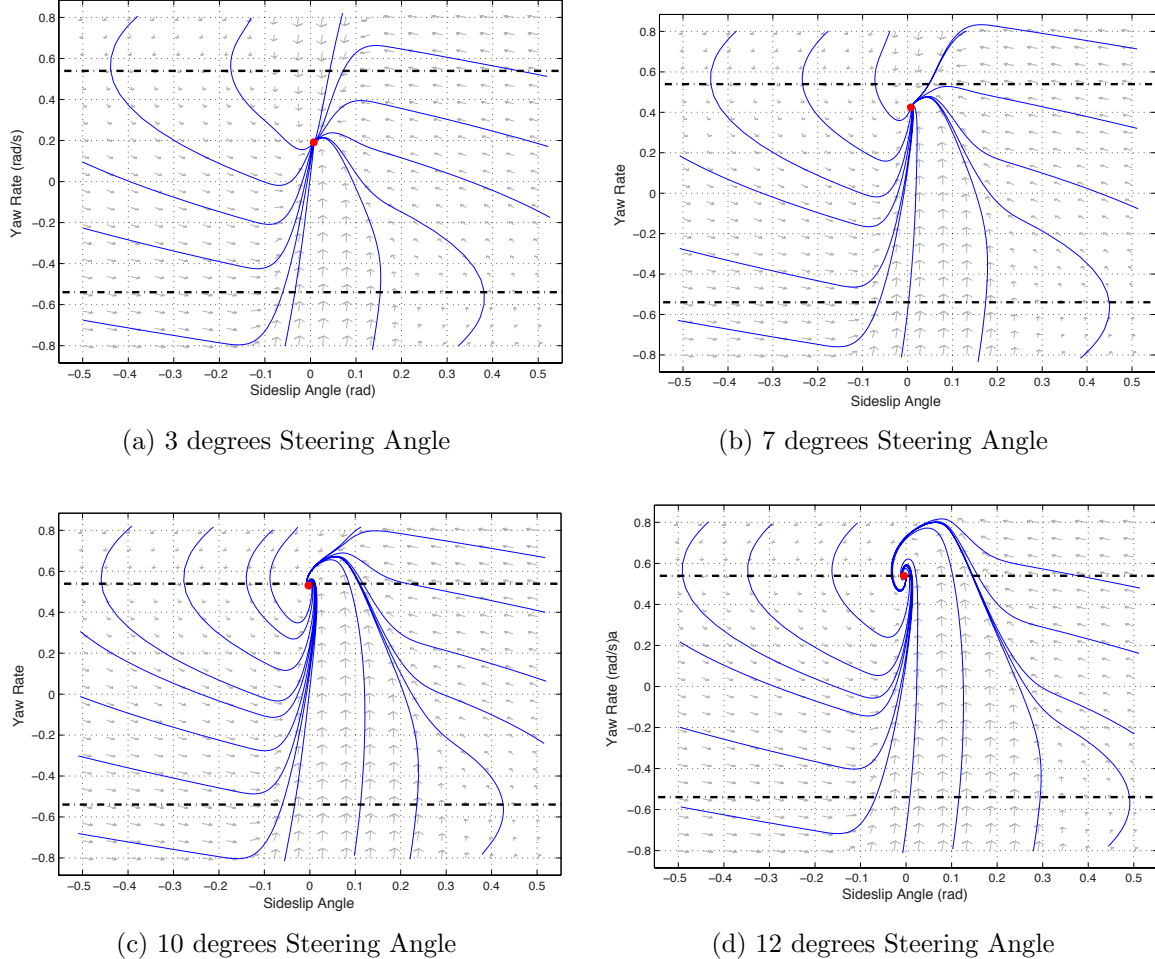


Figure 3.2: Understeering Vehicle Dynamics at 10m/s

instability remain valid for understeering and oversteering vehicles as well. Not only is this important for evaluating production vehicles with different weight distributions and handling properties, but it is also critical since the application of drive and brake torques can alter the handling behavior at the friction limits. Figure 3.2 shows the same vehicle as before, but with the maximum available force on the front axle reduced to produce limit understeering behavior. Figure 3.3 illustrates the same vehicle again, but with the friction on the rear axle reduced to produce limit oversteering behavior. In each case, the axle with reduced force capability is modeled with an effective friction coefficient of 0.55, reduced from 0.6.

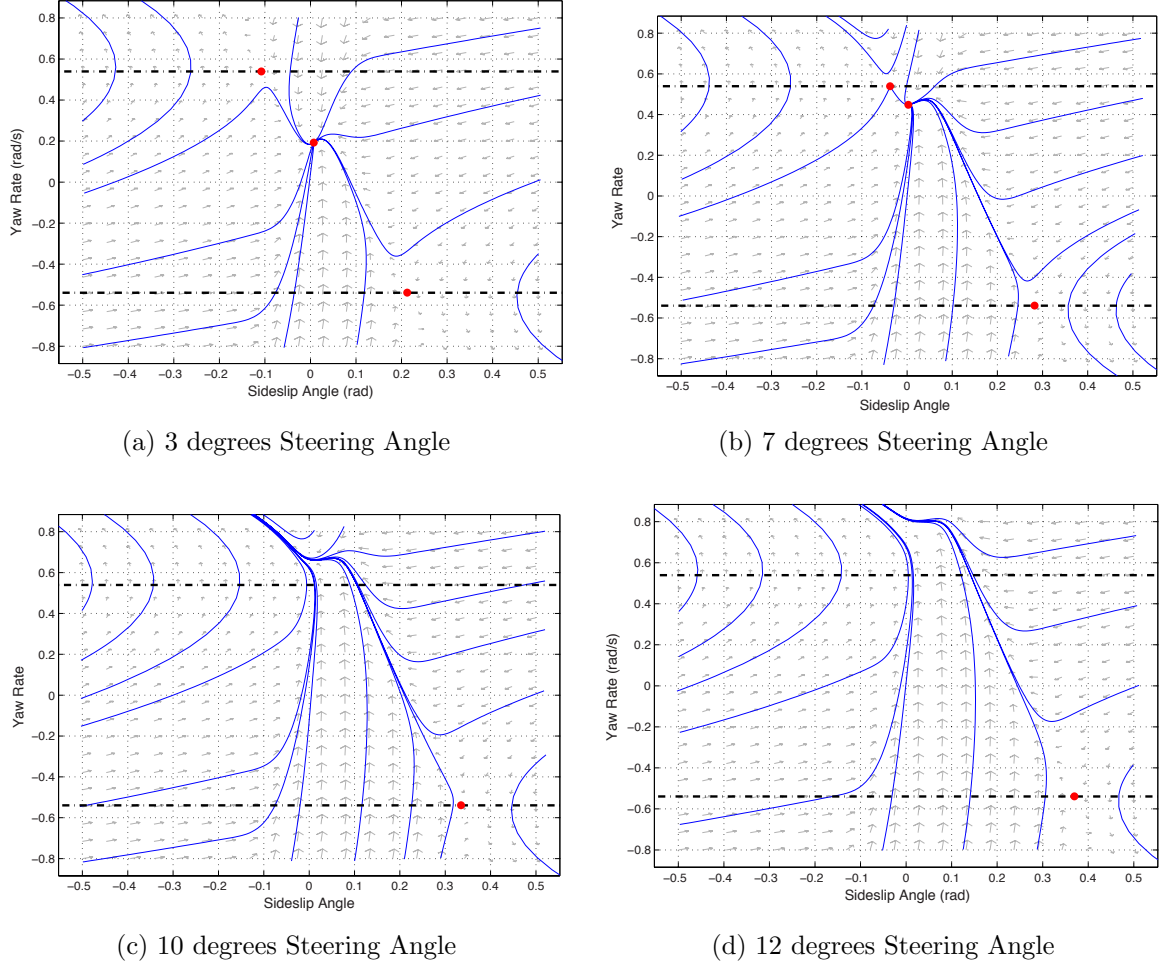


Figure 3.3: Oversteering Vehicle Dynamics at 10m/s

When the vehicle understeers, the stability problems of the neutral vehicle disappear, but the oscillatory behavior associated with an understeering vehicle becomes apparent. Like the neutral vehicle, there is also convergence to the equilibria within the maximum yaw equilibrium bounds. The oversteering vehicle, as expected, demonstrates significant degradation of stability. For 7° of steering angle, the stable equilibrium is quite close to the saddle point, beyond which the dynamics are strongly divergent. As a result, minor disturbances at this condition could cause the vehicle to spin. When the steering angle is increased to 10°, the vehicle exhibits the unstable tendencies seen at larger steering angles with the neutral steering vehicle. However, in

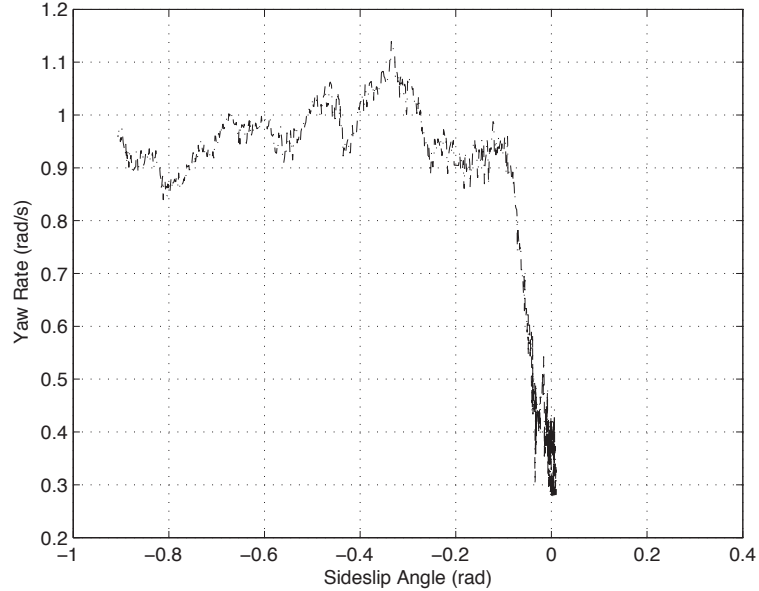


Figure 3.4: Vehicle Dynamics at 10m/s on Slippery Surface with Large Steer Angle

in this case, the yaw rate continues to grow once the maximum equilibrium boundaries are exceeded and the vehicle “spins out” rather than experiencing a lateral slide.

This can be seen in experimental data as well. P1, the experimental steer-by-wire testbed for which the parameter set was taken for the plots in Figure 3.1, was used to perform an experiment where the vehicle was driven manually to equilibrium cornering. At  $10\frac{\text{m}}{\text{s}}$  and at an equilibrium near  $0.4\frac{\text{rad}}{\text{g}}$  yaw rate, the accelerator pedal was used to upset the vehicle in the corner, yielding dynamics somewhere in between the neutral nominal dynamics and the oversteering dynamics illustrated in the previous plots. No controller was active on the vehicle during the test, and the steering angle was held constant. Figure 3.4 shows the state trajectory of the vehicle in the phase plane. From this plot, the behavior that is expected from the phase plane analysis is evident. Because the vehicle is upset with rear wheel torque, the initial phase of the maneuver approximately follows the unstable growth of yaw rate seen in Figure 3.3 as a result of reduced lateral force capability on the rear axle. Once the vehicle is upset, the accelerator is released and the neutral steering characteristics of the vehicle return. However, since the yaw rate is well into the region of unfavorable dynamics,

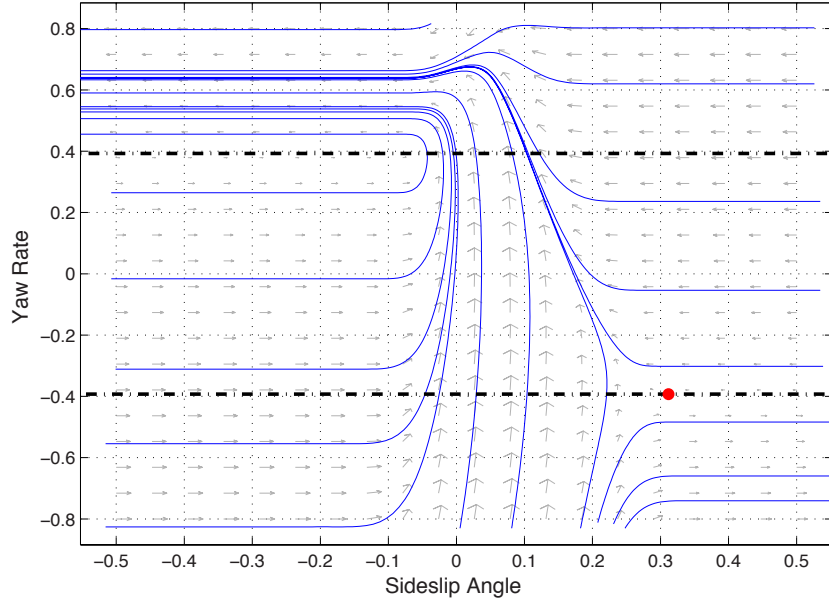


Figure 3.5: Neutral Vehicle Dynamics at 15m/s with 7 degrees Steering and 0.6 Surface Friction Coefficient

the sideslip angle grows rapidly as the vehicle spins, as is predicted by the upper left hand portion of the phase plots in Figure 3.1. The experimental data from the maneuver are truncated for clarity, but the vehicle comes to rest at a sideslip angle of over 180° as it fully spins out.

Aside from the steering angle from the driver, the vehicle speed is also a critical parameter. From the expression of the lateral acceleration,  $a_y = \dot{\beta} + rU_x$ , it is clear that since the forces needed to produce lateral acceleration are limited, as the vehicle speed increases, the maximum yaw rate must decrease. Figure 3.5 shows the phase plane for the vehicle with a 7° driver steering angle on the same surface as the previous figures, but at 15  $\frac{m}{s}$ . While the lines of maximum steady state yaw rate are located at lower values and the steering angle that destabilizes the vehicle is smaller, the dynamics are remarkably similar to those illustrated in Figure 3.1d. In both plots, the unstable dynamics occur in the same location relative to the lines of maximum yaw equilibrium.

From the plots shown in this section, it is clear that regions of unstable dynamics

can be identified and separated from the stable regions of handling by a constant yaw rate boundary. All of the stable equilibria for the bicycle model lie within these bounds, and the work of Hindiyeh and Gerdes [28] demonstrates that even the equilibria for high sideslip “drifting” maneuvers lie along these bounds. Supporting the importance of measuring and bounding the yaw rate of a vehicle is the observation that over the range of steering angles, speeds, and vehicle handling properties, the large sideslip angles develop only after the yaw rate grows large. Since this yaw measurement can be made directly, accurately, and inexpensively, these observations suggest excellent opportunities for control.

## 3.2 Defining Boundaries of Unstable Regions

In designing a stability controller, the objective is to assist the driver in maintaining, to the extent that the dynamics allow, control over the orientation and path of the vehicle. In the best case, the system would allow the driver to have full authority over the vehicle in all situations in which the vehicle dynamics are favorable and intervene only in the case of the vehicle beginning to enter a region of unstable dynamics. Therefore, the insights gained from the yaw-sideslip phase plane in the previous section can be used to develop an envelope that includes a large set of the stable dynamics but excludes regions of instability. Since there are well-defined undesirable regions, the primary challenge in determining the envelope is thus to calculate the boundaries of an appropriate envelope in real time.

Fortunately, many vehicles being manufactured today are incorporating electric power steering and future vehicles may be equipped with steer-by-wire, both of which have been shown by Hsu and Gerdes [32] to allow for estimates of both sideslip angle and tire-road friction coefficient. It is this additional information that enables the identification of stable handling envelopes.

### 3.2.1 Defining a Safe Handling Envelope

In the previous section, analysis of the unstable vehicle dynamics showed that the equilibrium yaw rate associated with the maximum available tire forces is a key quantity. Below this yaw rate, the vehicle dynamics are stable and the states converge toward stable equilibria. Therefore, it makes sense when designing a stable handling region to include a yaw rate constraint. Assuming that the axle normal loads are known and the tire-road friction coefficient can be estimated with a technique such as that presented by Hsu and Gerdts, then a tire model may be assumed and a yaw rate constraint can be expressed simply as a function of the estimated peak tire forces:

$$r_{\max} = \begin{cases} \frac{F_{y_{r\max}}(1+b/a)}{mU_x} & F_{y_{f\max}} \geq \frac{b}{a} F_{y_{r\max}} \\ \frac{F_{y_{f\max}}(1+a/b)}{mU_x} & F_{y_{f\max}} < \frac{b}{a} F_{y_{r\max}} \end{cases} \quad (3.4)$$

This yaw rate constraint is, however, not sufficient to completely ensure the stability of the vehicle. In certain low-friction conditions, it is possible for disturbances or transients to excite large sideslip angles while maintaining low yaw rates, as demonstrated by Rock, et. al. [56]. To prevent the vehicle from reaching this condition, a second set of bounds can be used to close the stable handling envelope. A variety of boundaries may be chosen for this purpose, but choosing a constraint on the rear axle slip angle results in natural scaling of the envelope. This is in part due to the fact that the rear slip angle remains small at low speeds and does not exhibit the non-minimum phase behavior seen in the sideslip angle. The rear slip angle is also a linear combination of the vehicle sideslip angle and the yaw rate and is dependent on the vehicle speed, as seen by the rear slip expression,  $\alpha_r = \beta - \frac{b}{U_x}r$ .

As a result, the allowed sideslip scales naturally with both the speed and the yaw rate, allowing the driver to utilize a significant portion of the state space associated with stable driving. One natural choice for the value of this rear slip angle boundary is the angle at which the tire force reaches full saturation. Thus, a controller that enforces these boundaries will maintain the vehicle within the grip limits of the tires. However, choosing the rear slip limit in this way may feel constraining to skilled drivers who may be capable of driving the vehicle with the rear tires in saturation.

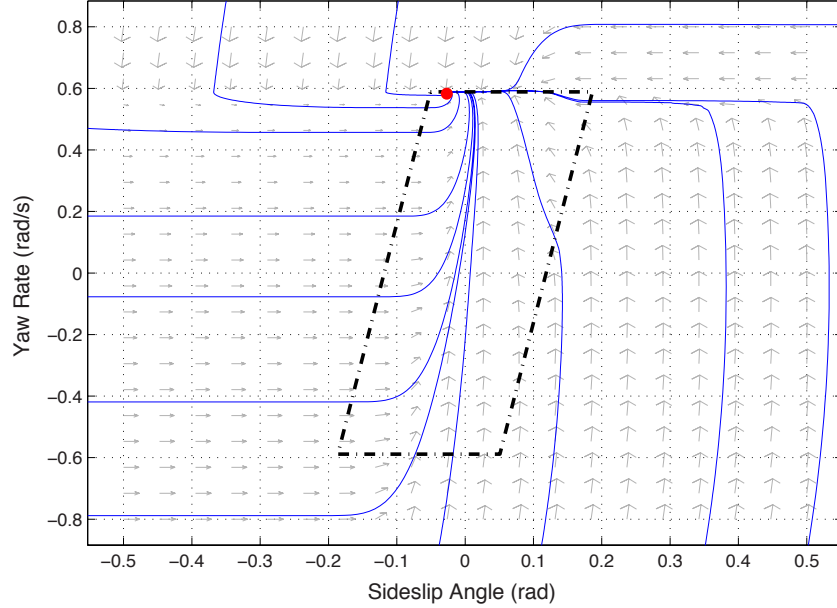


Figure 3.6: Phase Portrait with Model Predictive Envelope Controller

Fortunately, arbitrarily wide rear slip limits may be chosen to allow skilled drivers to drift the vehicle without a stability control intervention and yet vehicle stability can be guaranteed.

The envelope boundaries form a parallelogram in the yaw-sideslip plane, as illustrated in Figure 3.6, where the stable handling envelope is plotted over the phase plane with a model predictive envelope controller active. From this figure, it is clear that the dynamics on the interior of the envelope are nearly identical to the uncontrolled vehicle. However, outside the envelope, the controller alters the unstable dynamics to stabilize the unstable regions and push the vehicle back toward the envelope interior. The remaining task is to verify that it is possible to design a controller to enforce the invariance of the envelope. This is done by finding a control input that causes the yaw rate and sideslip derivatives to cut into the envelope on every portion of the boundary.

If active front steering is used to enforce the boundaries of the envelope, the control action on the boundary is to alter the front axle lateral force. Figure 3.7 shows the envelope with possible state derivatives plotted at points on each of the boundaries.

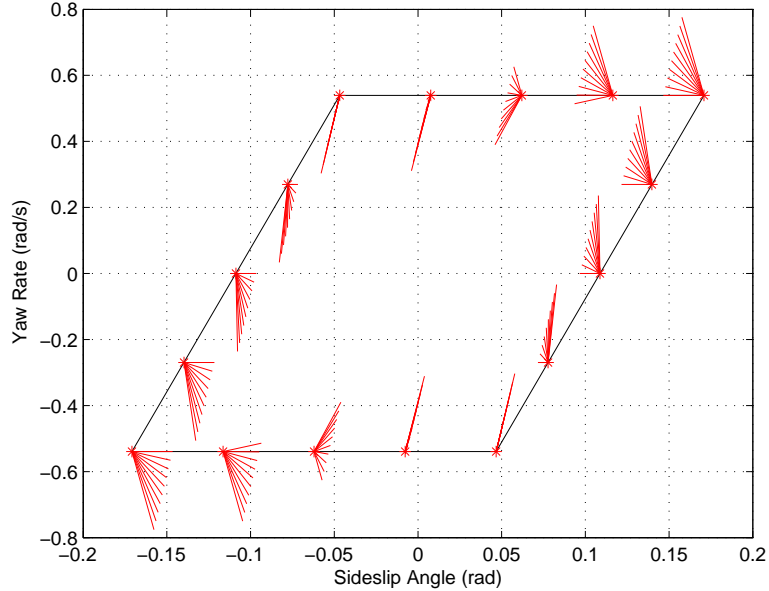


Figure 3.7: Ranges of Possible Vehicle Trajectories on Envelope Boundaries

The set of arrows at each point shows the complete range from the minimum to the maximum front lateral force. From the diagram, it is possible to see that at every point, there is a trajectory that stays within the envelope. At the top right and bottom left corners, only the extreme lateral force keeps the vehicle in the envelope. However, this is sufficient to establish the feasibility of creating an invariant envelope. More complete statements are presented for the model predictive envelope controller in the following chapter. Similar analyses may be performed for other actuation schemes, including independent braking such as that used by production stability control, rear wheel steering, or differential drive.

### 3.2.2 Alternative Envelopes

In defining a safe handling envelope, there are a variety of choices that may be made. The envelope presented in the previous section is straightforward to develop, analyze, and implement. Chapter 4 will demonstrate that this envelope is also capable of the desired augmentation of the vehicle dynamics in cooperation with the driver.

However, there are a number of other envelopes that may be utilized instead. This section presents several alternative envelope formulations.

### An Envelope to Allow Rear Tire Sliding

As mentioned in the description of the envelope in the previous section, it is possible to change the value of the rear slip angle bounds. This does not result in a change in the shape of the envelope, but merely makes the envelope wider. This larger envelope allows a driver to fully saturate the rear tires, as is done in drifting, and the controller only intervenes if the driver fails to keep the vehicle within these wider bounds.

Since these boundaries are designed to allow skilled drivers to maximize the capabilities of the vehicle, it is also interesting to see how the same system might be viewed by a less skilled driver. Assuming that the less skilled driver intends to maintain rear tire grip, any excursion beyond the peak slip angle can be viewed as a mistake. If this happens and the driver fails to correct, the rear end of the car will slide up until the point where the envelope controller intervenes. With the rear slip angle bounds set at this wider point, this motion will be felt by the driver, allowing the driver to experience and learn from these dynamics without losing control of the car.

Figure 3.8 illustrates the dynamics of the vehicle under envelope control with yaw rate bounds as described in the previous section, but with wider slip angle boundaries set at  $\pm 20^\circ$ . The vehicle speed and steering angle are  $10 \frac{m}{s}$  and  $10^\circ$ , respectively. The action of the controller is similar to that of the narrow boundary controller, where the dynamics on the interior of the envelope remain very similar to the uncontrolled vehicle. However, above the yaw rate boundary, the controller intervenes strongly to prevent the buildup of excessive yaw rate and sideslip angle such as in the uncontrolled case.

### An Envelope to Allow more “Turn-in”

Skilled drivers, particularly those with racing experience, may notice with both the narrow and wide boundary envelopes presented in the previous sections that the yaw response when initiating a corner is slightly diminished when compared to the

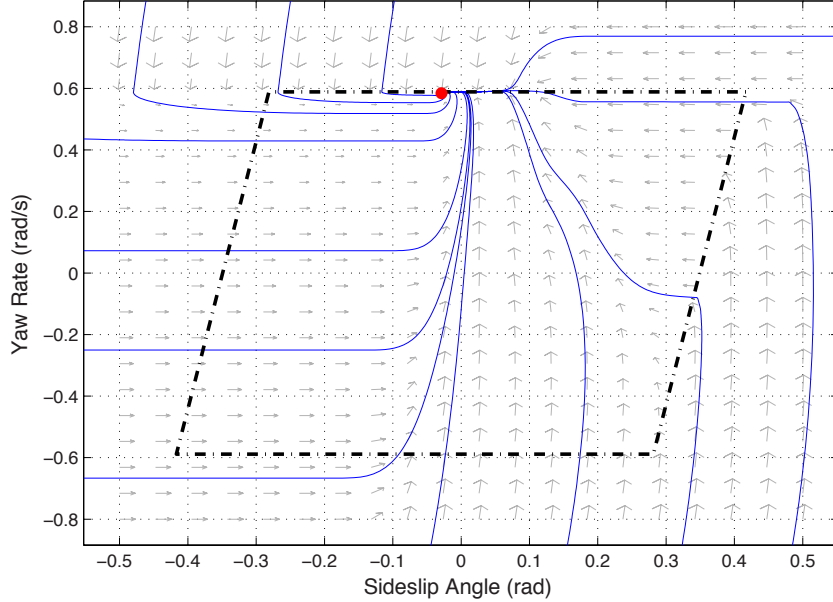


Figure 3.8: Handling Envelope for  $10^\circ$  Steering at  $10 \frac{m}{s}$  with Slip Bounds at  $\pm 20^\circ$

uncontrolled vehicle. This is because the yaw response of the uncontrolled system has a small overshoot in the yaw rate before reaching equilibrium. This can be seen in Figure 3.9c. In order to restore this turn-in response, the constant yaw rate boundary can be changed to a graduated yaw boundary that allows for more yaw rate at low sideslip angles. This variation of the yaw rate boundary is shown in figures 3.9a and 3.9b. The yaw boundary is set so that it passes through the rear tire slip angle for peak force at the maximum steady state yaw rate. The slope of the line is then set by choosing the amount of additional yaw rate to allow at zero sideslip angle. In figure 3.9, this is set to 15%. Because of a convexity requirement for the envelope and the fixed point for the boundary to pass through, this forces a slight reduction in the allowed rear slip angle at higher yaw rates, as seen in Figure 3.9a. Thus, the additional allowed “turn-in” yaw rate and slip angle at higher yaw rates are traded off, and the designer of the system must select the best compromise for the driving style of intended drivers.

One final advantage to this approach is that if the boundary is chosen properly, the controller need not interfere with the normal stable dynamics, even when

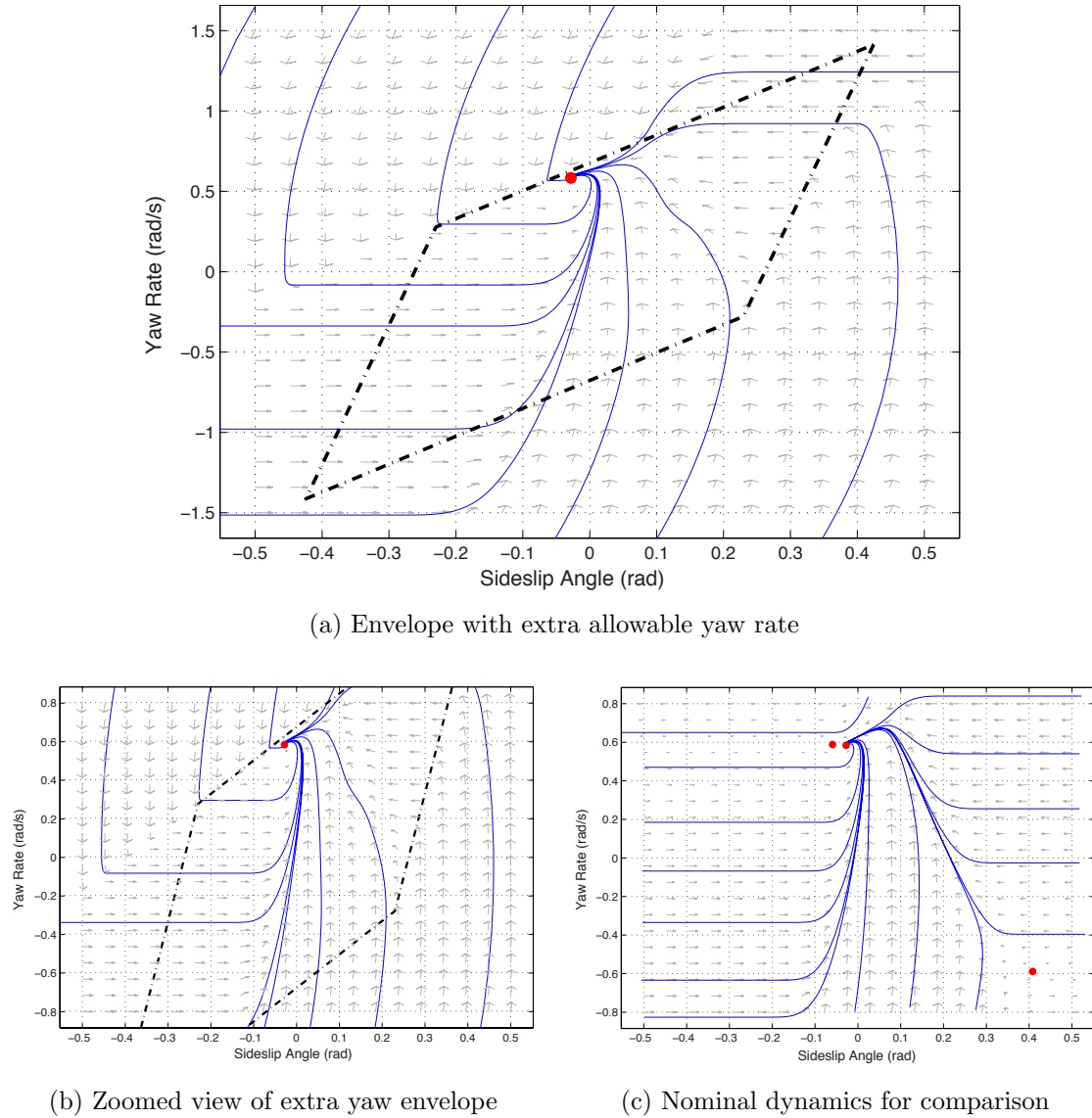


Figure 3.9: Handling Envelope for 10° Steering at 10  $\frac{m}{s}$  with Slip Bounds at  $\pm 20^\circ$

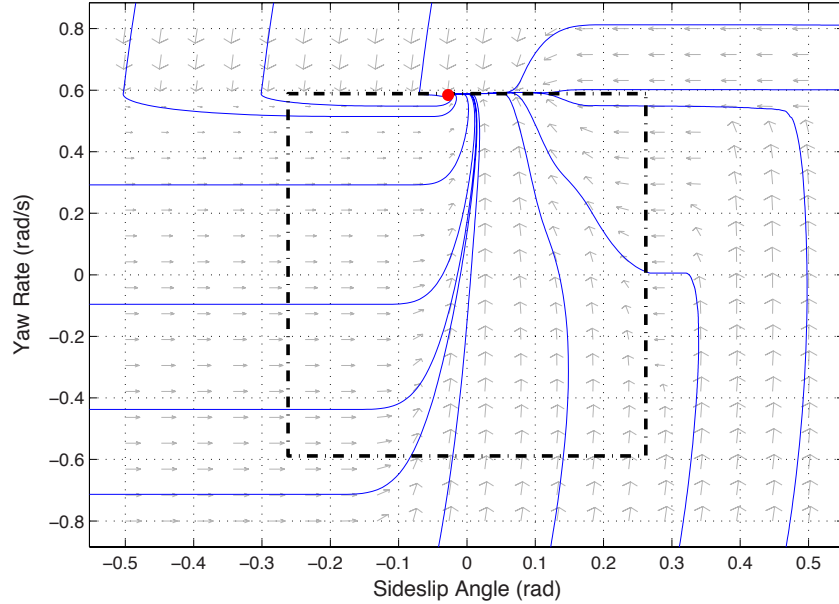


Figure 3.10: Handling Envelope for  $10^\circ$  Steering at  $10 \frac{m}{s}$  with Sideslip Bounds at  $\pm 15^\circ$

they exceed the maximum steady state yaw rate, as seen in the comparison of Figures 3.9b and 3.9c. The boundary lies directly alongside the nominal overshoot dynamics, but eliminates the unstable region where the sideslip angle of the vehicle begins to diverge. Thus, the vehicle behavior will be very close to that of the uncontrolled vehicle that drivers may be accustomed to and the envelope controller will not exercise needless control action to eliminate normal stable dynamics.

### A Yaw-Sideslip State Envelope

It is also possible to define an envelope using only the states of the bicycle model. This yaw-sideslip state envelope is illustrated in Figure 3.10. Though the use of the sideslip angle makes the controller slightly simpler than those using the rear slip angle, the drawback is that the controller lacks the natural scaling of the slip bound with the yaw rate and vehicle speed.

### An Envelope Defined by Tire Grip

One final choice of envelope is one where all of the boundaries are defined by the angles of peak tire force. In this case, the angles at which the front and rear axles saturate are calculated from an assumed tire model and used to restrict the vehicle motion. This envelope, utilized in [3, 4], is diamond shaped in the state space since lines of constant front slip angle have negative slopes. The drawback to the use of this envelope is that it couples together the actuator and the state limits. Since the linearized front slip angle is  $\alpha_f = \beta + \frac{a}{U_x}r - \delta$ , this could limit the amount of countersteer allowed by the controller in cases where the steering angle must be changed rapidly to stabilize the vehicle.

## 3.3 Discussion

The insight gained from examining the dynamics suggests an alternative to the approach used in production stability control systems. This approach specifies a region of stable handling in which the driver has full authority to control the vehicle. The boundaries of this stable handling envelope are developed naturally from information about the tire-road friction coefficients and scale well with vehicle speed and tire grip. With techniques for leveraging new sensing opportunities from electric power steering (EPS), the boundaries of these unstable regions can be reliably estimated. Variants of the boundaries can be also be used to yield different handling characteristics at the maximum extents of the envelope to satisfy the preferences of different drivers.

The results of this chapter serve not only to elucidate the dynamics of vehicle instability, but also to form a basis for designers of future stability control systems to synthesize controllers and make guarantees about vehicle performance. This framework also opens up many other possibilities for vehicle control, including the use of new or combined actuation to stabilize the vehicle, consideration of rollover or environmental factors in determining the proper driver assistance, and the ability to combine stability control with higher level controllers for more advanced vehicle control tasks.

# Chapter 4

## Envelope Control

The previous chapter was devoted to the development of a stable handling envelope that prevents the vehicle from entering undesirable handling regions. However, the analysis was restricted to establishing the feasibility of stabilizing inputs on the boundaries of the envelope and did not discuss a control technique for generating these inputs. This chapter presents a model predictive envelope controller capable of enforcing the boundaries of the safe handling envelopes and providing progressive and smooth assistance to a human driver.

### 4.1 Control Strategy

In enforcing the boundaries of the envelope, the controller presented in this chapter must satisfy two objectives. The first is that the controller must respond appropriately in the event that a driver input would cause the vehicle to leave the envelope or that a disturbance pushes the states outside the envelope. The second is that the controller should track the driver's intended vehicle behavior inside the envelope and behave in a predictable manner when at or beyond the envelope boundaries.

Since a model predictive controller operates by solving an optimization problem to determine a set of inputs that satisfies an objective and any constraints over a specified control time horizon at each control time step, model predictive control (MPC) provides a straightforward method of implementing an envelope control strategy. In

the MPC framework, tracking the driver's desired trajectory becomes the objective while the envelope boundaries and actuator limits are the constraints. Furthermore, after finding the optimal input sequence, the first input in the sequence is applied to the system and the process is started again. In this manner, the optimization routine needs only to find an open-loop optimal set of inputs, but the resampling and recomputation at each time step provides a feedback loop to take into account deviations from the optimal trajectory from disturbances or model error, for example. The following subsections describe how an envelope control scheme can be implemented in a model predictive control formulation.

#### 4.1.1 MPC with the Affine Force-Input Model

While there are clear advantages for using model predictive control to implement the envelope controller, there are some significant challenges in this process. Most significant of these is the choice of model with which to inform the controller. At the limits of handling, where the envelope controller must be active to assist the driver, a linear model provides a poor representation of the vehicle dynamics. However, the nonlinear brush tire models presented in Chapter 2 are both computationally expensive and non-convex. As a result, the optimization routine used to determine the output of the model predictive controller may run too slowly for real time operation in a vehicle and worse yet, may produce emergent behaviors.

Convex optimization provides a solution to both of these problems. Certain classes of optimization problems, when phrased correctly, have a single unique solution and can be solved with computationally efficient methods [10, 44, 45, 46]. Therefore, the definition of a convex model of the nonlinear vehicle dynamics at the handling limits is desirable for the implementation of the model predictive envelope controller.

The rationale for using the AFI model to implement the model predictive controller can be explained by examining the equations of motion for the single-track model, given here again as Eq. 4.1. It is obvious by inspection that the equations are

linear in the front and rear lateral forces, highlighted in bold font.

$$\dot{\beta} = \frac{\mathbf{F}_{yf} + \mathbf{F}_{yr}}{mU_x} - r, \quad \dot{r} = \frac{a\mathbf{F}_{yf} - b\mathbf{F}_{yr}}{I_{zz}} \quad (4.1)$$

The controller design presented in this chapter assumes a vehicle with rear wheel drive and front steering, where the controller has the authority to augment the driver's steering command up to the limits of the actuators. In this configuration, the drive torques and steering are located on separate axles and so the tires on the front axle generate only lateral forces. Therefore, a manipulation of the steering can be seen simply as a state-dependent front lateral force command. Taking this abstraction a bit farther, the front lateral force can be viewed by the optimization solver as the input to the system rather than the front steering angle. Thus, by changing variables, the non-convex relationship between front lateral force and steering angle is extracted outside the optimization solver as seen in Figure 4.1, maintaining the ability to rapidly solve the problem while preserving the characteristics of the desired tire model.

Unfortunately, this technique does not work on the rear axle of the vehicle due to the lack of actuation. The rear lateral tire force is a function of the vehicle states and the longitudinal slip. Worse, this function is non-convex and is needed to accurately calculate the predicted model states in the optimization routine. As a result, the rear tire linearization in Eq. 2.18 is used. With the pre-solve and post-solve steps illustrated in Figure 4.1, the resulting optimization problem is convex and thus can

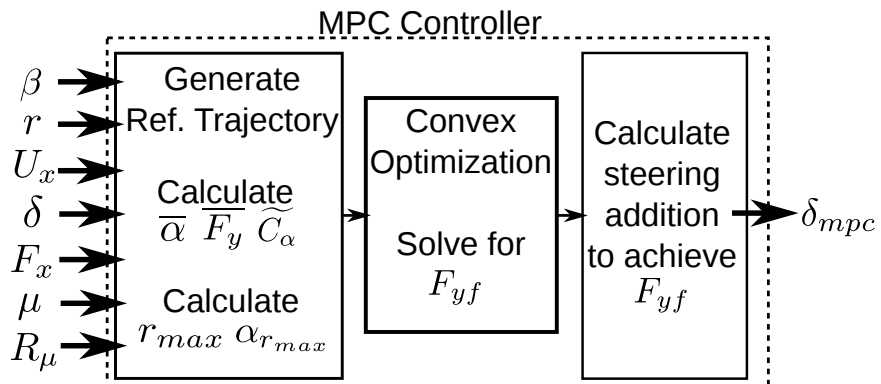


Figure 4.1: MPC Block Diagram

be solved robustly and rapidly through the use of well-known convex optimization techniques [10].

### 4.1.2 Envelope Boundaries

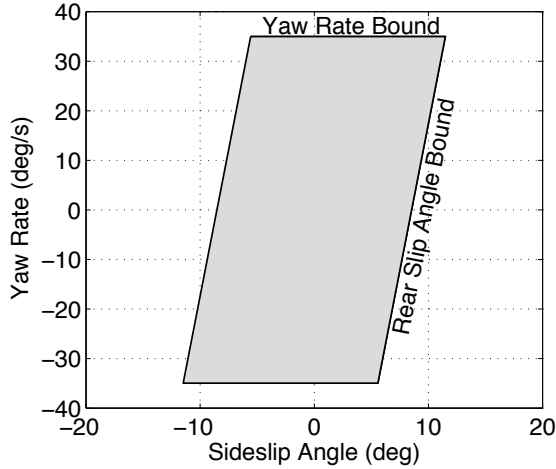


Figure 4.2: MPC Envelope Controller Boundaries

The envelope for the controller is a parallelogram in state space, as introduced in the previous chapter and seen in Figure 4.2. The envelope boundaries are computed using an approximation of the tire-road friction coefficient, which is assumed to be estimated in real-time. It is not expected that an exact value of the friction coefficient will be known, particularly since it is likely to be varying frequently with the changing road surface, as seen in experimental results.

Using the friction information, the first envelope constraint is computed from the steady-state yaw rate associated with the estimated maximum tire forces. To close the envelope in the state plane, a second set of constraints that limit the sideslip angle are needed. However, a simple limit on the sideslip angle has significant drawbacks when considering the sideslip angle dependence on speed and vehicle parameterization. A better choice for the boundary is the slip angle of the rear tire, which scales naturally with speed and also includes the effect of yaw rate, limiting the sideslip angle at high yaw rates. Given estimates of the vehicle cornering stiffness and tire-road friction

coefficients, Eq. 2.4c specifies the angle associated with the maximum tire force generation. Using this angle to set the maximum rear slip angle yields a conservative envelope in which the vehicle maintains rear tire grip. However, highly skilled drivers can maintain vehicle stability while the rear tires attain large slip angles. The same is true of the envelope controller, and this performance can be achieved by choosing the rear slip angle boundary to be a few degrees past the peak. In practical testing, experienced drivers preferred the wider rear slip angle boundaries and enjoyed being able to stably slide the vehicle with the assistance of the controller.

### 4.1.3 Tracking Driver Intent

Stabilizing the vehicle is an important function of an envelope controller, but to assist the driver in guiding the vehicle along a safe trajectory, the envelope controller also utilizes a tracking objective. There are a limited number of sensors available in production vehicles that yield information about the driver's intended vehicle behavior. Thus, the control design assumes that the driver's intended yaw rate and sideslip can be inferred by holding the steering angle and vehicle speed constant and propagating a linear bicycle model over a  $150ms$  control horizon to determine the target states to use for tracking. Away from the envelope boundaries, the linear model matches the vehicle behavior and renders the controller silent, providing an alternative to the use of logic to switch the controller on and off.

#### 4.1.4 Controller Implementation

When described as a control problem for MPC, the output of the controller at each time step is the solution to the optimization problem described here:

$$\text{minimize} \quad \sum_{k=1}^N \left\| x_{\text{opt}}^k - x_{\text{des}}^k \right\|_{W_x}^2 + \sum_{k=1}^{N-1} \left\| F_{yf}^k \right\|_{W_u}^2 + \eta \sum_{k=1}^N \left\| s_{\text{opt}}^k \right\|_1 \quad (4.2a)$$

$$\text{subject to} \quad x_{\text{opt}}^1 = A_d x_{\text{init}} + B_d F_{yf_{\text{init}}} \quad (4.2b)$$

$$x_{\text{opt}}^{k+1} = A_d x_{\text{opt}}^k + B_d F_{yf}^k + d_d, \quad (4.2c)$$

$$k = 1, \dots, N-1$$

$$F_{yf_{\text{min}}} \leq F_{yf}^k \leq F_{yf_{\text{max}}} \quad (4.2d)$$

$$k = 1, \dots, N-1$$

$$\left| F_{yf}^k - F_{yf}^{k+1} \right| \leq F_{yf_{\text{slew}}} \quad (4.2e)$$

$$k = 1, \dots, N-2$$

$$C_{\text{lim}} |x^k| \leq x_{\text{lim}} + s_{\text{opt}}^k \quad (4.2f)$$

$$k = 1, \dots, N$$

$$s_{\text{opt}}^k \geq 0, \quad k = 1, \dots, N \quad (4.2g)$$

Each term in this optimization statement has physical meaning in terms of the functionality of the envelope control system. The first term in the objective function (Eq. 4.2a) represents the tracking objective. Thus, error between the solution trajectory and the desired linear behavior is penalized through a weighted norm. This ensures that the optimal control input tracks the driver's desired behavior. The second term in the input is a weighted norm on the inputs. For the controller described here, the only input to the system is  $F_{yf}$ , but by defining the function as a weighted norm on the inputs, the problem may be extended to additional actuators. The final term in the objective function is a penalty on the slack variables that are added to the problem to ensure that the constraints do not cause the problem to become infeasible.

The dynamic constraints (Eqs. 4.2b-4.2c) describe the dynamics that the solution trajectory must obey. These dynamics are obtained by discretizing the continuous

Table 4.1: Description of Envelope Controller Parameters

Parameter	Description
$A_d$	Discrete State Propagation Matrix
$B_d$	Input Effect Matrix
$d_d$	Affine Offset from Linearization
$W_x$	State Tracking Weight Matrix
$W_u$	Input Penalty Matrix
$x_{\text{des}}$	Open Loop Trajectory from Driver Input
$x_{\text{init}}$	Vehicle State at Start of Optimization
$F_{yf_{\text{init}}}$	Front Force Input at Start of Optimization
$F_{yf_{\text{min}}}$	Minimum Available Front Force Input
$F_{yf_{\text{max}}}$	Maximum Available Front Force Input
$F_{yf_{\text{slew}}}$	Maximum Front Force Slew Rate
$C_{\text{lim}}$	Output Constraint Matrix
$x_{\text{lim}}$	State and Input Limits
$\eta$	Stiffness of Slack Variables

AFI system given in Eq. 2.21. A Tustin discretization method is used since it offers a closed-form solution that can easily be implemented in real time. The third constraint (Eq. 4.2d) restricts the MPC solver to a range of inputs that are achievable given the estimated friction coefficients and normal load on the front axle. Similarly, Eq. 4.2e restricts the maximum change in the lateral force so that the actuator slew rate limits are respected. Finally, Eq. 4.2f implements the constraints that define the boundaries of the envelope. Since yaw rate is one of the system states and rear slip angle is a linear combination of yaw rate and sideslip angle, the limit calculation matrix,  $C_{\text{lim}}$ , and limit vector,  $x_{\text{lim}}$ , are:

$$C_{\text{lim}} = \begin{bmatrix} 0 & 1 \\ 1 & -\frac{b}{U_x} \end{bmatrix}, \quad x_{\text{lim}} = \begin{bmatrix} r_{\text{lim}} \\ \alpha_{r_{\text{lim}}} \end{bmatrix} \quad (4.3)$$

### Predictive Time Horizon and Update Rate

The time step and horizon for the MPC problem are 10ms and 15 steps, respectively, yielding a 150ms predictive time horizon. This horizon is well-scaled to the vehicle control problem for two reasons. The first is that the dynamics of vehicle are fast enough that most of the response of the vehicle to a sudden input or disturbance can be observed in 150ms. Therefore, the controller can predict the dynamics far enough in advance to prevent hazardous responses to these sudden events. However, the preview horizon cannot be extended arbitrarily since error in the prediction grows as the model is propagated forward in time. The AFI model, as presented in Section 2.2.3, uses a single linearization of the rear tire. Because of this linearization, the model is most accurate at the beginning of the horizon and less accurate later on when the states move farther away from the initial conditions. Likewise, the driver input and vehicle speed are assumed to be constant over the time horizon. Since the longitudinal dynamics typically have bandwidth less than 1-2Hz and the responses of skilled drivers are usually less than 3Hz, the assumption that these parameters remain constant over the 150ms time horizon is reasonable. Furthermore, the 100Hz update rate chosen to implement the controller means that any changes to the states, speed, and driver input are taken into account within 10ms, leading to very good handling of these slowly varying parameters.

#### 4.1.5 Real Time MPC Implementation

The optimization problem that results from the envelope controller is convex, as seen by inspection of the terms, and thus a specific set of embedded convex optimization tools can be brought to bear on the problem. Using software such as described in [45] and [46], custom C-code is generated which can solve the model predictive envelope control problem with a 15-step horizon in under 2ms on a single core of an Intel Core2 Duo processor. Despite fast solution techniques, this solve step requires non-trivial computation time, so delay compensation is also added to the controller as described in [17]. This is expressed in the problem formulation by Eq. 4.2b, where the states after one time step are dictated solely by the initial conditions. By doing

this, the MPC problem is solved not for the time step at initiation of the solver, but rather a solution is computed for the following time step when the inputs are applied.

## 4.2 Results and Discussion

### 4.2.1 Experiment: Limit Slalom Maneuver

The first set of results with the model predictive envelope controller are shown in Figure 4.3. This test was designed to excite the vehicle dynamics with steering input at roughly constant speed such that an uncontrolled vehicle would have left the envelope. To ensure consistent, clean excitation of the vehicle steering, the sinusoidal driver steering input was generated using the vehicle computer. The envelope control parameters are shown in Table 4.2, while the results are illustrated in Figure 4.3, where Figure 4.3a shows the vehicle states throughout the maneuver. The surface friction coefficient was estimated to be approximately 0.55-0.6, and so it is clear that the vehicle is very close to the maximum lateral acceleration on each phase of the sinusoidal maneuver.

Figure 4.3b shows the limited quantities along with the dynamically calculated envelope boundaries. Because the boundaries are dependent upon vehicle speed, friction coefficients, and rear-wheel torque, all of which are held nearly constant, little variation in the limits occurs through the maneuver. Examining the limited quantities, it is clear that aside from a slight overshoot of the yaw rate, the controlled vehicle remains within the envelope boundaries. However, the advantage of the envelope controller goes beyond preventing major excursions of the vehicle states outside of the envelope. Using the AFI model to predict the vehicle behavior, the controller is capable of holding the vehicle very close to the boundaries. Assuming that the boundaries are set at the maximum capabilities of the vehicle, the controller is capable of assisting the driver while utilizing all of the vehicle's cornering capability while maintaining stability.

Figure 4.3c shows the sinusoidal driver steering command as well as the total command that is applied to the front wheels after the controller steering addition. In

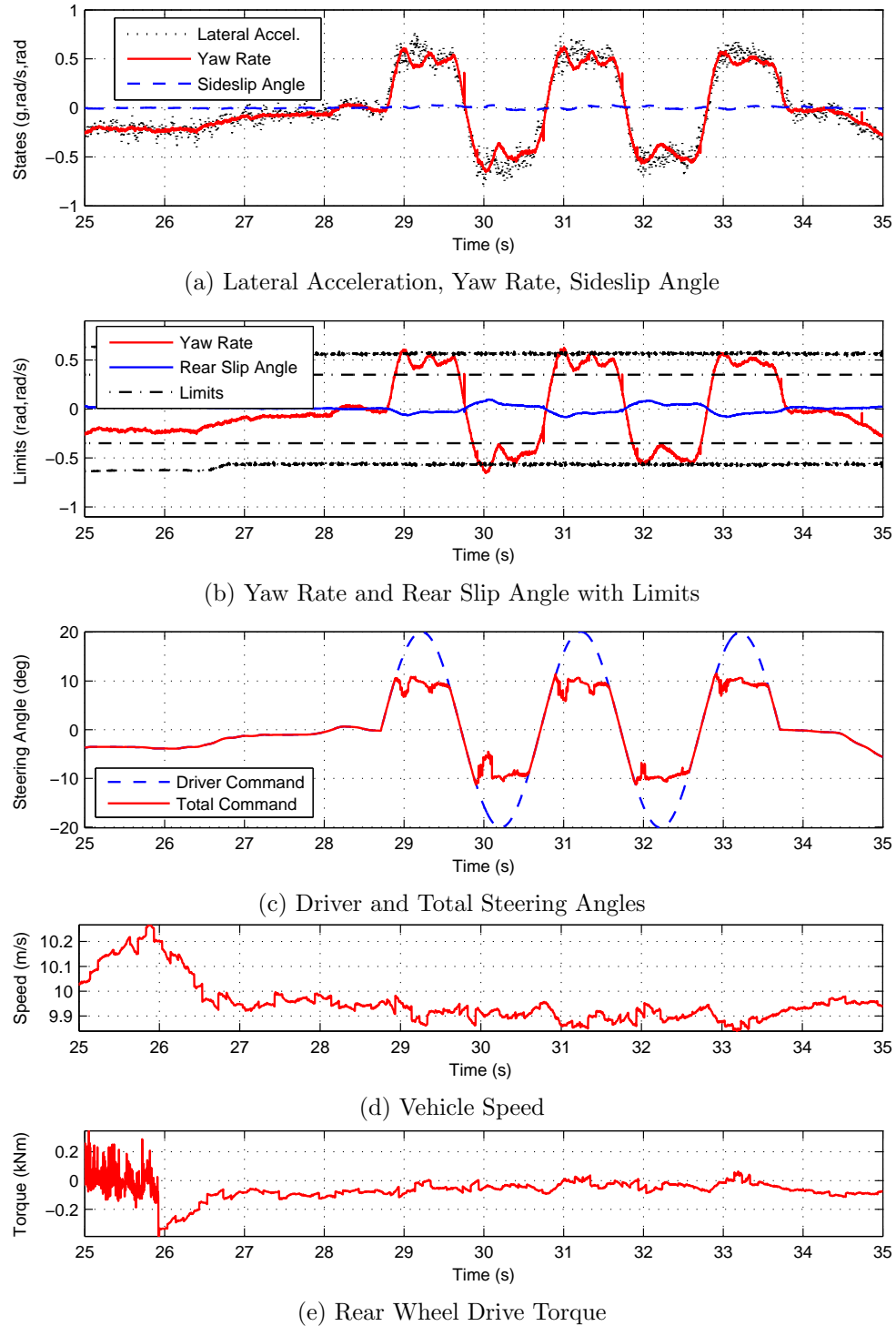


Figure 4.3: Experimental Results from Slalom Maneuver

in this case, the driver command would cause the vehicle to exceed the boundaries of the envelope and so the controller countersteers to compensate. An important note here is that there is no delay in resuming the driver command once the driver steering angle is attainable within the envelope. Therefore, there is no lag in the steering if the driver chooses to reverse the direction of the vehicle.

#### 4.2.2 Simulation: Slalom with Friction Variation

One other feature in the data sets seen particularly in the yaw rate and steering signals of Figure 4.3 is an oscillation around the limit. Because the gravel is unevenly distributed on the test surface, this oscillation reflects the controller response to disturbances. This can be confirmed with a simulation run where the grip properties of each wheel are chosen from a random distribution.

Table 4.2: Envelope Controller Parameters with AFI Model

Parameter	Symbol	Value
MPC horizon	$N$	15
MPC time step	$\Delta T$	0.01s
Sideslip tracking weight	$W_{x_\beta}$	$5 \frac{1}{rad}$
Yaw rate tracking weight	$W_{x_r}$	$50 \frac{s}{rad}$
Input penalty weight	$W_{F_{yf}}$	$1 \times 10^{-5} \frac{1}{N}$
Slack variable penalty	$\eta$	$5 \times 10^4$
Input limit	$F_{yf_{\max}}$	††
Input slew rate limit	$F_{yf_{\text{slew}}}$	††
Yaw rate limit	$r_{\lim}$	††
Rear slip limit	$\alpha_{r_{\lim}}$	††
Static friction coefficient	$\mu$	0.6
Sliding friction coefficient	$\mu_s$	0.55

†† : Parameter is computed in real-time before optimization step.

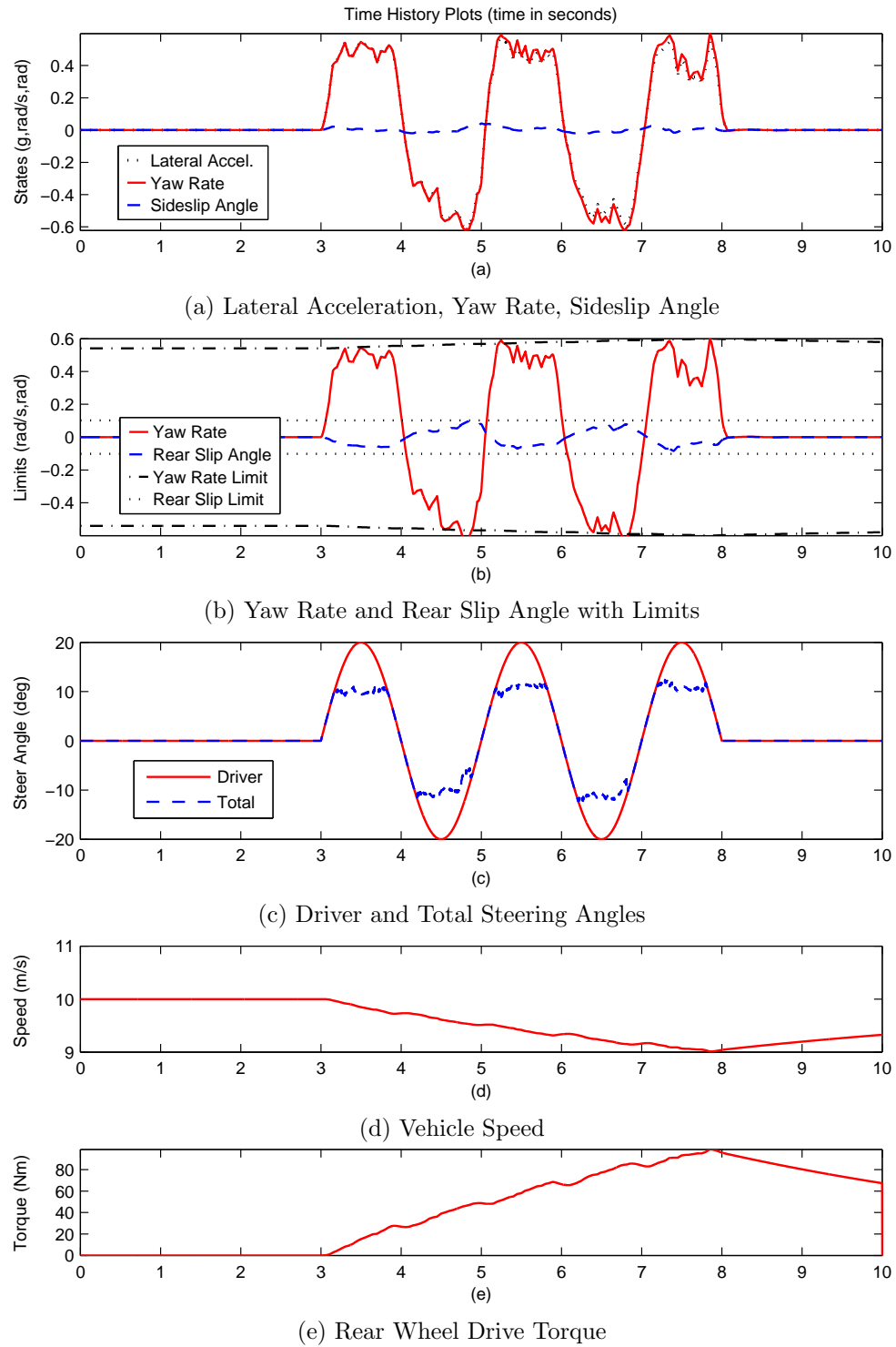


Figure 4.4: Simulated Results from Slalom Maneuver

The conditions for the simulation were set as closely as possible to match those of the experimental slalom shown in Figure 4.3, including identical controller parameters. The friction coefficients were varied independently for each wheel every 0.04s to represent the effect of unevenly distributed gravel. At the vehicle speed of 10 m/s, this equates to a 40cm length scale for the friction variation. The distribution was assumed to be uniformly random, within the ranges  $\mu = 0.6 \pm 0.4$  and  $\mu_s = 0.55 \pm 0.4$ . Since the friction coefficient  $\mu$  always appears in the lateral tire force expression given in Eq. 2.1 as a product with normal force, this variation can also represent the changing normal load on a wheel.

Once the random friction conditions were incorporated into the simulation framework, oscillations of approximately the same magnitude and frequency as in the experiments were observed. This is particularly apparent when looking at the first two cycles of slalom in Figs. 4.3cc and 4.4c, where the total steering command is plotted. Similar effects are also seen in Figs. 4.3b and 4.4b, where the yaw rate and rear slip angles show this same oscillatory behavior.

### 4.2.3 Experiment: Limit Cornering with Rear Drive Torques

The previous two sets of results demonstrate the vehicle behavior when primarily excited with steering input. However, rear-wheel drive vehicles on low-friction surfaces exhibit significant degradation in stability when large drive torques are applied. Figure 4.5 shows the vehicle behavior while applying drive and braking torques to the rear axle while cornering. This maneuver is intended to develop oversteer by reducing the available lateral force on the rear axle. A sequence of drive-brake-drive-brake torques at the actuator limits is used to provide multiple instances of excitation to test the controller. Figure 4.5 shows the results from the maneuver and the controller parameters are again those given in Table 4.2.

As with the previous figures, Figure 4.5a is a plot of the yaw rate, sideslip angle, and lateral acceleration. Figure 4.5b illustrates the yaw rate and rear slip angles along with their limits. In this case the limits are a bit more interesting, as the rear wheel torque and speed profiles (seen in Figs. 4.5d and 4.5e) significantly affect the

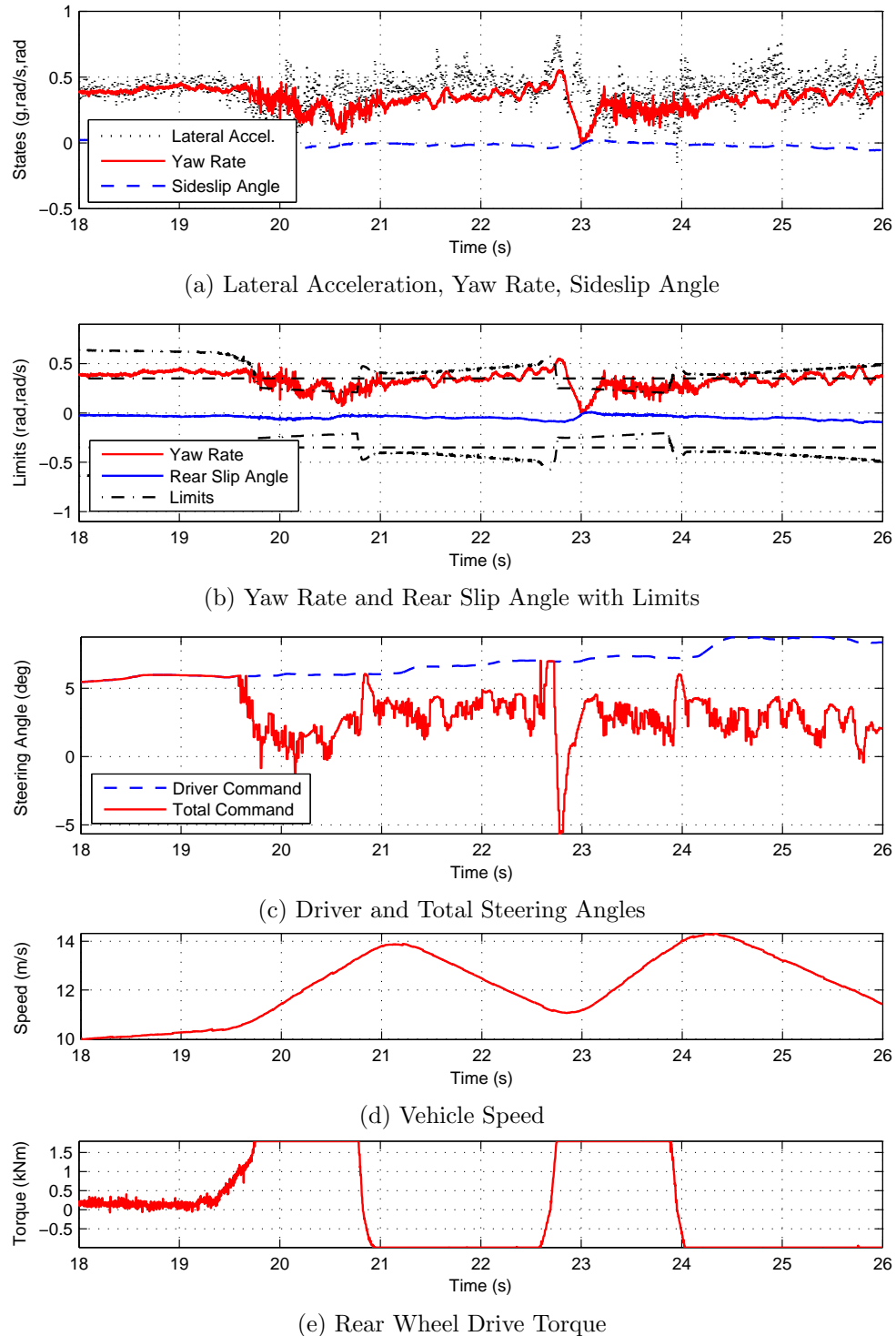


Figure 4.5: Experimental Results from Cornering with Torque Disturbances

Table 4.3: Envelope Controller Parameters with Linear Model

Parameter	Symbol	Value
MPC horizon	$N$	15
MPC time step	$\Delta T$	$0.01s$
Sideslip tracking weight	$W_{x_\beta}$	$5 \frac{1}{rad}$
Yaw rate tracking weight	$W_{x_r}$	$50 \frac{s}{rad}$
Input penalty weight	$W_\delta$	$1 \frac{1}{rad}$
Slack variable penalty	$\eta$	$5 \times 10^4$
Input limit	$\delta_{lim}$	$\pm 22^\circ$
Input slew rate limit	$\delta_{slew}$	$\pm 140^\circ/s$
Front slip limit	$\alpha_{f_{lim}}$	$\pm 8^\circ$
Rear slip limit	$\alpha_{r_{lim}}$	$\pm 8^\circ$

†† : Parameter is computed in real-time before optimization step.

limits. For example, at approximately 22.5s the accelerator is depressed to command maximum torque. The yaw rate and rear slip angle limits are instantly decreased since the MPC controller calculates that the maximum achievable values are lowered. However, the vehicle states cannot respond instantaneously, and so for several time steps the states are outside the new, smaller envelope. The controller therefore countersteers hard to bring the states inside the envelope and then returns the vehicle again to the boundary, giving the driver the maximum possible cornering capability.

#### 4.2.4 Experiment: Control Performance with Linear Model

The representation of rear tire saturation in the AFI model (Eq. 2.18) is critical in obtaining the performance of the envelope controller seen in Figure 4.5. Without the prediction of decreased rear lateral force, the controller would be incapable of responding accurately to the rapid growth in rear slip angle. To illustrate the necessity of this information, a set of experiments was performed with a purely linear tire model used to predict the forces that would be developed on each axle. Figure 4.6 demonstrates a lift-off oversteer on a mixed dirt and gravel surface. For this test, the model underlying the controller utilized a static linearization about zero slip angle at the rear axle and assumed a purely linear mapping between front steering angle and front lateral tire force. A front slip angle limit also replaced the yaw rate constraint. The parameters of this model, seen in Table 4.3, were chosen to allow the tires to get to full saturation.

Figure 4.6a shows the vehicle states throughout the maneuver. Note here that the vehicle has already entered a corner at 56s when the timeline of the plot begins. The driver continues to increase the steering angle (seen in Figure 4.6c) until reaching a limit understeering case where the controller countersteers to keep the front slip angle near the envelope boundary. There is a small steady-state error during the initial cornering phase as a result of the tire model overstating the effect of steering input near tire saturation. Usage of the AFI model avoids this by including the saturation dynamics in the steering angle calculation. When the driver applies drive torque to the rear axle, the rear slip angle increases dramatically. The controller countersteers, but the tire model mismatch results in a poor prediction of the dynamics in this highly nonlinear region and thus a violation of the envelope boundary occurs. Because the linear model has no representation of this tire saturation, the controller underestimates the steering input needed to stabilize the vehicle. The countersteer maneuver does eventually return the vehicle to the envelope, and the controller is successful in stabilizing the vehicle in the lift-off oversteer maneuver.

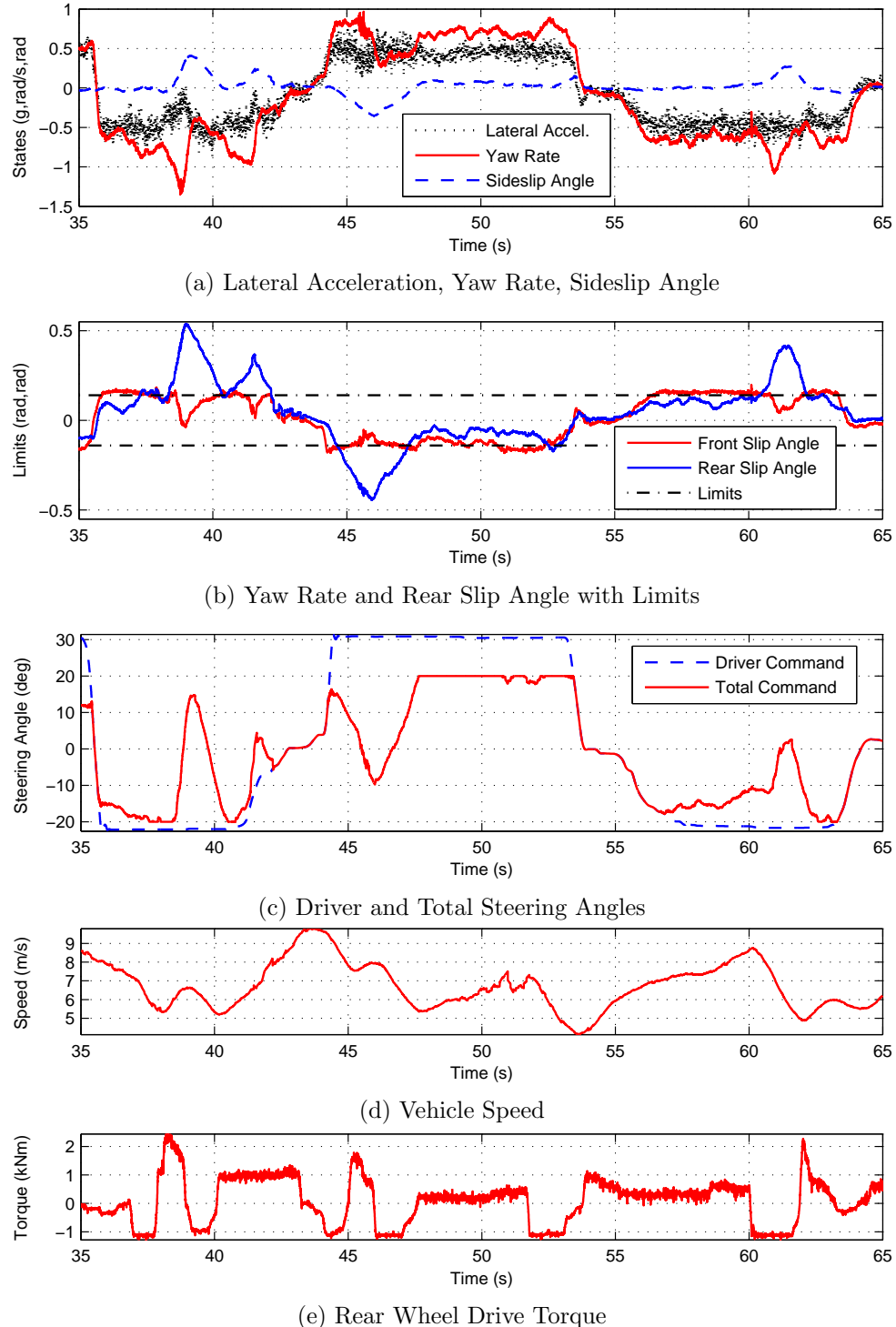


Figure 4.6: Experimental Results from Lift-off Oversteer Maneuver

#### 4.2.5 Experiment: Control with Wide Slip Boundaries

In Chapter 3, a series of alternative envelopes were presented, including an envelope with extended rear slip angle boundaries intended to allow a driver to saturate the rear tires and allow the car to slide without losing control. Figure 4.7 demonstrates the performance of the vehicle while under envelope control with this enlarged envelope. The rear slip angle boundaries are set to a static value of  $20^\circ$  for the maneuver and the driver performs a lift-off oversteer followed by a double lane change. In the lift-off oversteer, the driver lifts off the accelerator pedal while cornering as seen by the plot of the states in Figure 4.7a and the torque input in Figure 4.7e, producing braking torque and resulting in a significant rear tire saturation and the rear axle beginning to slide. However, once the rear slip angle gets near the boundary, the controller countersteers as seen in Figure 4.7c and holds the rear slip angle approximately at the boundary (Figure 4.7b) until the driver begins to reduce the braking torque and steer out of the turn. Later in the data set, the driver performs a double lane change at approximately  $12\frac{m}{s}$ . Though the double lane change excites both the yaw and slip dynamics of the vehicle, the rear slip angle remains well away from the limit and only the yaw rate constraint is enforced.

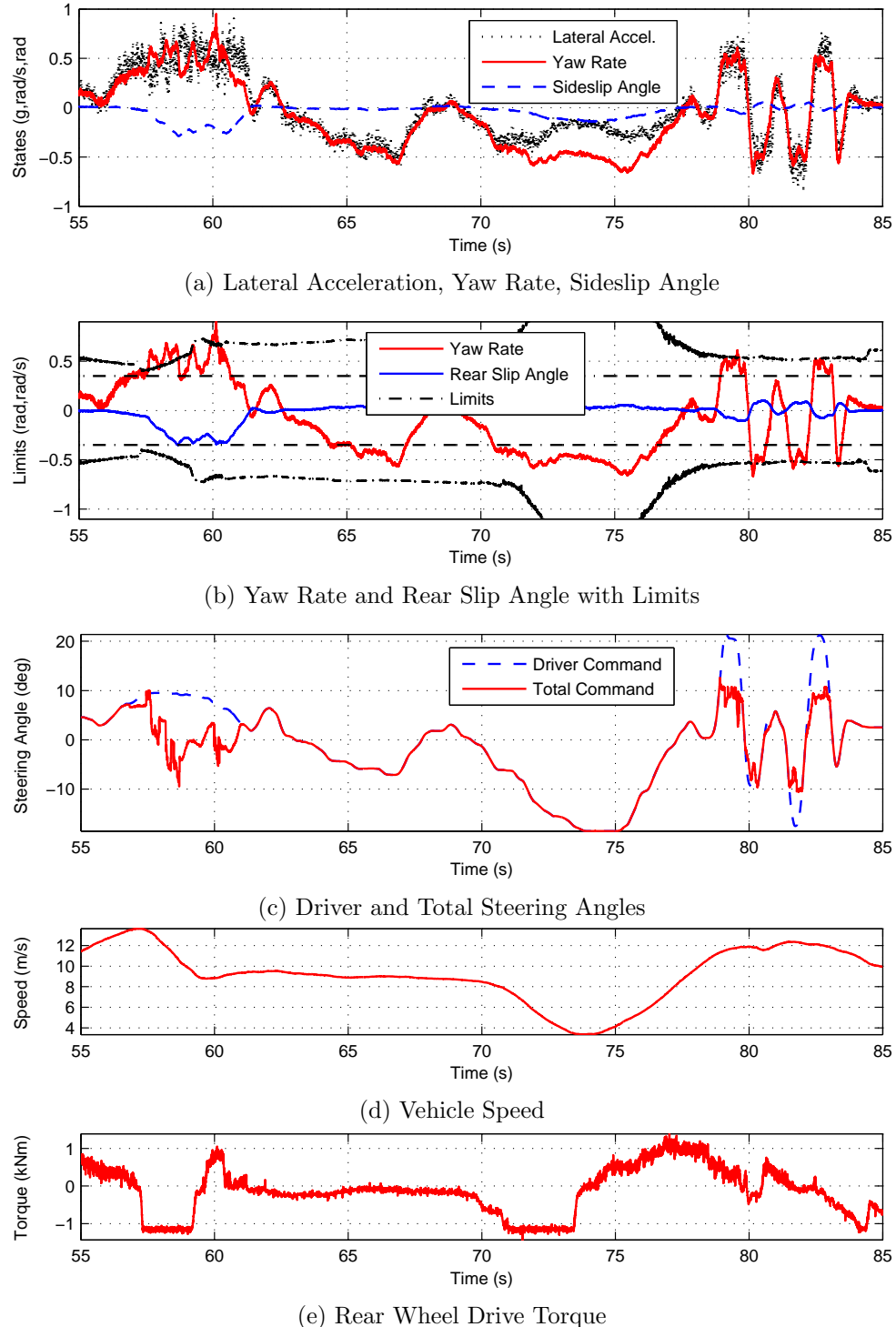


Figure 4.7: Experimental Results with Wide Rear Slip Angle Boundaries

## 4.3 Guaranteeing Controller Action

The following subsections examine the action of the vehicle under envelope control to demonstrate that the controller is capable of keeping the vehicle inside the safe handling in the absence of disturbances and acts appropriately to attract the vehicle to the envelope in cases where disturbances or sudden reductions in envelope size cause the states to lie outside the boundaries of the envelope. These analyses are based on the assumption that the vehicle behavior is accurately described by a linear bicycle model with nonlinear brush tires as described in Chapter 2. In cases where the action of the controller using the AFI model is considered, the it is assumed that the AFI model is linearized at every point considered and thus yields the same response as the nonlinear model at each point. Error between these models and the behavior of the real vehicle is known to be minor and in many cases will be less than the error incurred through the utilization of an estimate of the real friction coefficient.

### 4.3.1 Envelope Invariance Proof

A proof that the model predictive envelope controller stabilizes the vehicle, regardless of the driver input, is presented in this section. Since the controller is not easily expressed in a closed form, the proof is presented by examining the range of stabilizing inputs and showing that the optimization will produce these inputs as the MPC input to the vehicle.

The proof presented here leaves out the slew rate limits for clarity. The test vehicle used in experiments with the controllers described in this paper has an extremely fast steering system [40] for which the slew rate constraints appear to be unrestrictive.

#### Theory of Exact Penalty Functions

It is common for a model predictive controller to contain, at its core, an optimization problem with both state and input constraints. As mentioned in the previous section, if both of these constraints are hard constraints, then the problem may be infeasible at some points. This can occur either due to the constraints being incompatible at some point in the state space or due to disturbances causing the states to deviate outside

the boundaries of the state constraints. In either case, the controller is incapable of determining a control action, so the constraints are softened in order to ensure problem feasibility. The drawback to softening the constraints is that the guarantee of controller action in the case that the original hard-bounded problem was feasible is lost. Fortunately, the theory of exact penalty functions provides a means to recover this guarantee.

In a paper by Han and Mangasarian [25], the authors describe the use of exact penalty functions with a hard-constrained optimization problem of the form:

$$\text{minimize} \quad f(x) \quad (4.4a)$$

$$\text{subject to} \quad g(x) \leq 0 \quad (4.4b)$$

$$h(x) = 0 \quad (4.4c)$$

where  $f$ ,  $g$ , and  $h$  are functions from  $\mathbb{R}^n$  into  $\mathbb{R}$ ,  $\mathbb{R}^m$ , and  $\mathbb{R}^k$  respectively. A point  $x$  in  $\mathbb{R}^n$  satisfying the constraints is considered to be a feasible point. This problem can be re-expressed as an optimization problem with no constraints, but with a cost associated with any non-feasible point.

$$\text{minimize} \quad f(x) + \alpha Q(\|g(x)_+, h(x)\|) \quad (4.5)$$

where  $\alpha$  is a nonnegative real number,  $g(x)_+$  is a penalty on any positive value of  $g(x)$ , and  $Q$  is a function that satisfies

$$Q(0) = 0 \quad (4.6a)$$

$$Q(\zeta) > 0 \text{ for } \zeta > 0 \quad (4.6b)$$

If  $Q(\zeta) = \zeta$  and the one-norm is used, then this problem becomes

$$\text{minimize} \quad f(x) + \alpha \left( \sum_{j=1}^m g_j(x)_+ + \sum_{j=1}^k |h_j(x)| \right) \quad (4.7)$$

and is of exactly the same form used for the envelope control problem. The results

presented by Han and Mangasarian demonstrate that given this problem, there is a condition on the penalty weight that is defined by the dual norm of the Lagrange dual optimal inequality and equality multipliers  $\lambda$  and  $\nu$ , for the original problem. If  $\alpha > \bar{\alpha}$  with

$$\bar{\alpha} = \|\lambda, \nu\|_\infty \quad (4.8)$$

then a solution to the soft-bounded problem will also be a solution to the hard-bounded problem, provided that the hard-bounded problem is feasible.

The hard-constrained envelope control problem can be expressed as a standard-form quadratic program with linear constraints, which is:

$$\text{minimize} \quad x^T Px + q^T x + r \quad (4.9a)$$

$$\text{subject to} \quad A_1 x - b_1 \geq 0 \quad (4.9b)$$

$$A_2 x - b_2 = 0. \quad (4.9c)$$

Therefore, the Lagrange dual problem can be expressed as:

$$\text{maximize} \quad r - \lambda^T b_1 - \nu^T b_2 \quad (4.10a)$$

$$\text{subject to} \quad q + A_1 \lambda + A_2 \nu \quad (4.10b)$$

$$\lambda \geq 0. \quad (4.10c)$$

For each combination of  $A_1$ ,  $A_2$ ,  $b_1$ ,  $b_2$ ,  $q$ , and  $r$ , there is an associated condition on the penalty weight defined, as before, by the dual norm of the optimal multiplying factors,  $\lambda^*$  and  $\nu^*$ . Since the desired soft-constrained problem uses the 1-norm to penalize the slack variables, the dual norm is the infinity-norm. Therefore, the condition needed for the envelope control problem slack weight is

$$\eta > \sup_{A_1, A_2, b_1, b_2, q, r} \|\lambda^*, \nu^*\|_\infty \quad (4.11)$$

With respect to the envelope control problem, this establishes that if the slack weight  $\eta$  is chosen to be sufficiently large and an input exists that prevents the vehicle from leaving the envelope, this input will be the solution to the optimization problem.

### Feasibility of the Envelope

In order to determine that a feasible input is present for all points on the boundary, the envelope is examined in each quadrant, as illustrated in Figure 4.8. In Quadrant I, the yaw rate and sideslip angle are both positive. Quadrant II contains states with positive yaw rates and negative sideslip angles. Quadrant III has negative yaw rates and sideslip angles and is symmetric to Quadrant I. Finally, Quadrant IV contains negative yaw rates and positive sideslip angles and is symmetric to Quadrant II.

Beginning with Quadrant II, in which open-loop equilibria for left turns lie, if they exist, the conditions for remaining in the envelope when on the boundary can be written as

$$\dot{r} \leq 0, \quad \dot{\alpha}_r \geq 0. \quad (4.12)$$

If, at every point on the boundary, these conditions can be satisfied, then the model predictive controller can find an input that will, at the first time step, keep the states from exiting the boundary. At subsequent steps in the time horizon, the predicted states may move away from the linearization point. As such, there may be error in the prediction, but exits from the envelope will still be prevented since only the first time step will elapse before the solution is recomputed.

The conditions on the states must be expressed in terms of the input,  $F_{yf}$  to ensure that they are feasible at every point on the boundary of the envelope. Beginning with the yaw rate, a bound on the input,  $F_{yf}$  is computed.

$$\dot{r} = \frac{aF_{yf} - bF_{yr}}{I_{zz}} \leq 0 \quad \Rightarrow \quad F_{yf} \leq \frac{b}{a}F_{yr} \quad (4.13)$$

Given sufficient steering range on the vehicle, this condition is easily achievable since  $F_{yr}$  is positive in Quadrant II and thus any negative  $F_{yf}$  is acceptable.

The rear slip angle derivative is comprised of a linear combination of the yaw rate and sideslip angle derivatives, and is thus more complicated than the yaw rate derivative. However, this can be handled in the same manner as the yaw rate derivative.

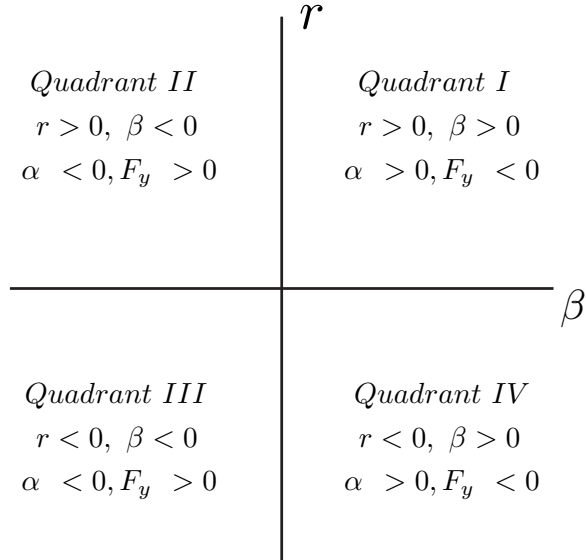


Figure 4.8: Four quadrants of the state space used for the proof

Beginning with the expression for the rear slip angle derivative,

$$\dot{\alpha}_r = \dot{\beta} - \frac{b}{U_x} \dot{r} \geq 0 \quad (4.14a)$$

$$\frac{F_{yf} + F_{yr}}{mU_x} - r - \frac{b}{U_x} \dot{r} \geq 0. \quad (4.14b)$$

Since the yaw rate condition must simultaneously hold,  $\dot{r}$  is known to be negative, and it is clear that with  $\dot{r} \leq 0$ , and  $m$ ,  $U_x$ ,  $I_{zz}$ , and  $F_{yr}$  all positive quantities, a somewhat conservative condition can be written as:

$$\frac{F_{yf} + F_{yr}}{mU_x} \geq r \quad (4.15)$$

On the boundary,  $\alpha_r = \alpha_{r_{\max}}$ , the rear tire is already fully saturated, yielding  $F_{yr} = F_{yr_{\max}}$ . Considering the case where the input is chosen to yield the least restriction on the yaw rate,  $F_{yf} = \frac{b}{a} F_{yr_{\max}}$ , this reduces to

$$\frac{F_{yr_{\max}} \left(1 + \frac{b}{a}\right)}{mU_x} \geq r \quad (4.16)$$

which is the yaw rate boundary of the envelope. Therefore, when inside the bounds, a feasible input may always be found which will prevent the vehicle from leaving the envelope. The same result holds for Quadrant IV by symmetry.

Quadrants I and III are considered pathological cases of the vehicle control scheme since these combinations of states can only be possible in transient cases and have not been observed in experiment. However, the dynamics of the controlled vehicle can be illustrated in the same way as with Quadrants II and IV. In Quadrant I, the slip angle condition changes sign, yielding the following conditions for maintaining the vehicle in the envelope.

$$\dot{r} \leq 0, \quad \dot{\alpha}_r \leq 0. \quad (4.17)$$

Beginning with the yaw rate equation like Quadrant II, the same condition on the front lateral force may be derived.

$$\dot{r} = \frac{aF_{yf} - bF_{yr}}{I_{zz}} \leq 0 \quad \Rightarrow \quad F_{yf} \leq \frac{b}{a}F_{yr} \quad (4.18)$$

However, unlike Quadrant II, the rear lateral force,  $F_{yr}$  is negative. Therefore, at the positive slip angle boundary, the input  $F_{yf}$  must be saturated at its minimum value to meet the yaw rate condition. This yields  $F_{yf} = \frac{b}{a}F_{yr}$  and  $\dot{r} = 0$ . Thus, while it is not possible to reduce the yaw rate everywhere, there is an input at every point on the boundary that prevents the yaw rate from growing and keeps the vehicle within the envelope.

This yaw rate condition also makes analysis at the slip angle boundary simple. Since the best-case input on the slip angle boundary yields  $\dot{r} = 0$  with  $F_{yf} = \frac{b}{a}F_{yr}$ , these values may be substituted into the slip angle dynamics.

$$\dot{\alpha}_r = \dot{\beta} - \frac{b}{U_x} \dot{r} \leq 0 \quad (4.19a)$$

$$\frac{F_{yf} + F_{yr}}{mU_x} - r - \frac{b}{U_x} \dot{r} \leq 0 \quad (4.19b)$$

$$\frac{F_{yr} \left(1 + \frac{b}{a}\right)}{mU_x} - r \leq 0 \quad (4.19c)$$

In Quadrant I,  $F_{yr} \leq 0$  and  $r \geq 0$  and thus the rear slip angle is reduced when the

yaw rate condition is satisfied. Again, the same conditions hold in Quadrant III by symmetry.

### Statement of the Proof

**Theorem 1.** *If, (1) the vehicle states are initially within the envelope, and (2) an input exists at every point on the envelope boundary that drives the system states to the interior of the envelope and (3) the penalty weight on the slack variables in the optimization problem is chosen according to Eq. 4.11, the vehicle cannot leave the envelope.*

*Proof.* Given that the vehicle starts inside the boundaries of the envelope, it is known from solving the appropriate linear programs that

$$10 \geq \eta > \sup_{A_1, A_2, b_1, b_2, q, r} \|\lambda^*, \nu^*\|_\infty, \quad (4.20)$$

The actual slack weight for the controller is set at 50,000 for good performance in cases with disturbances that result in the vehicle outside the boundaries. Thus, since the results demonstrate that an input exists on every point on the boundary that keeps the states from leaving the envelope, the hard-constrained problem is feasible. Therefore, the model predictive controller with sufficient slack weight will always select an input that preserves the invariance of the envelope.  $\square$

#### 4.3.2 Envelope Attraction

A demonstration that the envelope controller attracts the vehicle states to the envelope is possible by leveraging the optimality of the solution to the model predictive control problem. Since the controller solution will produce a trajectory with the lowest cost, it can be seen that inputs that attract the vehicle states to the envelope result in a smaller cost function than inputs that allow the vehicle states to drift away and therefore the controller will attract the vehicle to the envelope.

### Optimality of the Objective Function

The result of the optimization problem will seek to minimize the following objective function:

$$\text{minimize} \quad \sum_{k=1}^N \left\| x_{\text{opt}}^k - x_{\text{des}}^k \right\|_{W_x}^2 + \sum_{k=1}^{N-1} \left\| F_{yf}^k \right\|_{W_u}^2 + \eta \sum_{k=1}^N \left\| s_{\text{opt}}^k \right\|_1 \quad (4.21)$$

This objective function is dependent on both the input chosen and the resulting vehicle trajectory. Each summation may be examined to determine its effect on the output of the optimization. The first term in Eq. 4.21 minimizes deviation from the desired trajectory. While the desired trajectory is chosen based on the vehicle state and driver steering input, it is always restricted within the boundaries of the envelope. Therefore, any  $x_{\text{opt}}$  that is outside the envelope incurs cost in this term and the optimization will seek a trajectory that draws the vehicle closer to the nearest point on the envelope.

The second term in Eq. 4.21 is the sum of the force input required to achieve the desired trajectories. This term is added to the objective function with a low weight to incentivize small inputs when other criteria are satisfied. This term has the potential to push the solution for the vehicle trajectory away from the envelope, but since the maximum front lateral force is restricted, this term is bounded and small, and therefore has little influence on the solution.

The third and final term in Eq. 4.21 is the penalty on the slack variables. During normal operation inside the envelope, this term is zero. When outside the envelope, a large value of  $\eta$  causes this term to become dominant. Since the term is the sum of the linear deviations of both the sideslip and yaw rate states in the optimal trajectory, this term heavily penalizes any solution that does not return the states toward the envelope.

#### 4.3.3 Feasible Trajectories

From the discussion of the terms in the objective function, the ideal trajectory for an initial condition outside the envelope would seem to be along a line in the direction of

the nearest point on the envelope. However, the saturation dynamics of the tires may prevent the controller from achieving this trajectory. For example, Eq. 4.16 in the previous section demonstrated that when the rear tire is saturated and the vehicle is within the yaw rate bounds, the sideslip angle may always be reduced. However, this result may be reversed as well. In order to reduce the magnitude of the sideslip angle in Quadrant II,

$$\dot{\beta} = \frac{F_{yf} + F_{yr}}{mU_x} - r > 0 \quad (4.22)$$

However, if the vehicle is already outside of both the yaw rate and the slip angle boundaries, then

$$r = \gamma \frac{F_{yr_{max}} (1 + \frac{a}{b})}{mU_x}, \quad \text{and } F_{yr} = -F_{yr_{max}} \quad (4.23)$$

with  $\gamma \geq 1$ . Therefore,

$$\dot{\beta} = \frac{F_{yf} + F_{yr_{max}}}{mU_x} - \gamma \frac{F_{yr_{max}} (1 + \frac{a}{b})}{mU_x} \quad (4.24a)$$

$$= \frac{F_{yf} - \gamma \frac{a}{b} F_{yr_{max}}}{mU_x} \quad (4.24b)$$

Assuming the nominal weight distribution for the vehicle, the maximum front force is statically related to the rear force,  $F_{yf} = \frac{a}{b} F_{yr_{max}}$ . Thus,

$$\dot{\beta} = \frac{F_{yf} - \gamma \frac{a}{b} F_{yr_{max}}}{mU_x} \quad (4.25a)$$

$$= \frac{(1 - \gamma) \frac{a}{b} F_{yr_{max}}}{mU_x} \quad (4.25b)$$

$$\dot{\beta} \leq 0 \quad (4.25c)$$

which shows that outside the yaw rate and slip boundaries, it is not possible to directly increase the sideslip angle. Instead the yaw rate must first be reduced until it is below the bound, where the sideslip angle may be increased to re-enter the envelope.

Figure 4.9 illustrates a situation where the vehicle encounters a sudden reduction of the friction coefficient from 1.0 to 0.1. The vehicle, which was operating at the

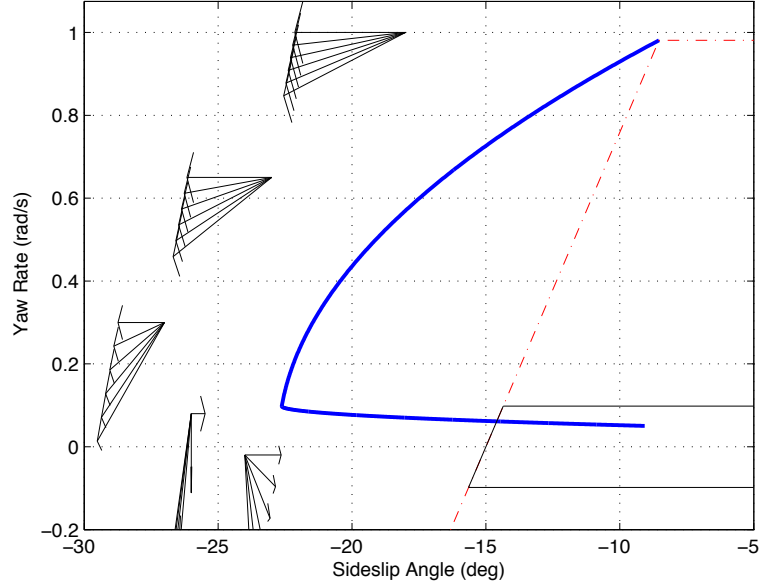


Figure 4.9: Feasible Envelope Re-entry Trajectory

edge of the envelope for the high friction surface, illustrated by the red dotted line, is suddenly well outside the envelope. Several bundles of arrows are plotted on the figure to demonstrate the direction of possible trajectories at various yaw rates. The arrows at the extremes represent the trajectories associated with  $F_{yf_{\max}}$  and  $F_{yf_{\min}}$ . Note that above the yaw rate limit of the smaller new envelope, these arrows show that the sideslip angle grows regardless of the chosen input. The resulting action of the controller is to maximize the reduction in yaw rate until it is possible to increase the sideslip angle and re-enter the new envelope for the changed friction conditions, illustrated by the black line.

This action represents the best case recovery for a vehicle using front-wheel steering for actuation. Unfortunately, the dynamics of the vehicle dictate that the rear slip angle will grow before recovering. In this case, the rear slip angle grew to a maximum deviation of 10° from the boundary before recovering.

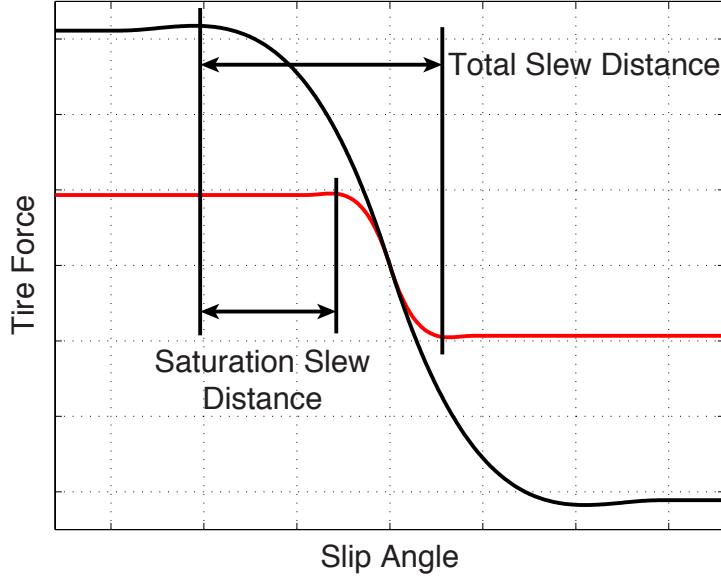


Figure 4.10: Slew Distance for Change of Tire Force

#### 4.3.4 Effect of Actuator Limits

In Figure 4.9, the steering system was assumed to be able to immediately attain the slip angle required to generate  $F_{yf\min}$  and reduce the yaw rate. However, to operate near the boundary of the initial high-friction envelope, the steering system is typically producing nearly the maximum front force and would thus have to slew the wheels from one side to the other to countersteer and reduce the vehicle yaw rate. Worse yet, the reduction in friction coefficient also causes a reduction in the slip angle associated with peak lateral force. As a result, the steering system must slew through the region of saturated maximum tire force before finally reaching a point where lateral force begins to decrease, as seen in Figure 4.10. This extended period in which the tire remains in saturation and produces the worst-case force drastically increases the rear slip angle growth, as seen in Figure 4.11.

This analysis underscores the importance of utilizing fast actuators and minimizing system delays in implementing the envelope control system. In situations with sudden disturbances or friction changes, a substantial and rapid intervention must

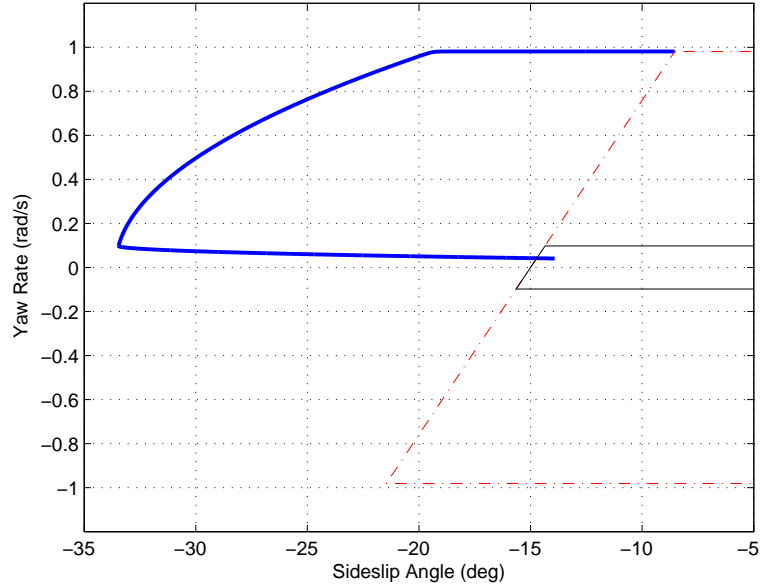


Figure 4.11: Envelope Re-entry with Slew Rate Limitation

be made. This also highlights the opportunities for assisting a human driver, since many drivers will initially fail to recognize the change in the driving conditions. Furthermore, once the driver has made the decision to act, there is an additional delay before physical action can be taken. Therefore, the fast response of the envelope control system can prevent the vehicle from spinning out and give the driver time to regain control.

## 4.4 Summary

The analysis presented in this chapter shows that the model predictive envelope controller augments the vehicle dynamics in precisely the desired manner so that the driver is provided with the assistance needed to maintain stability of the vehicle. The invariance proof presented in Section 4.3.1 demonstrates that the controller is capable of keeping the vehicle within the specified envelope boundaries when the vehicle speed, tire-road friction coefficient, and rear wheel torques remain constant.

Unfortunately, these quantities vary in normal driving and may change drastically in an emergency situation. In many cases, the envelope size may increase as a result in favorable changes in these parameters. However, in critical situations, the envelope is much more likely to decrease in size. If this reduction of the envelope occurs quickly, such as in the case of a sudden drop in friction, it will outpace the dynamics of the vehicle and the actuators and result in the vehicle states being outside the envelope. In this case, the analysis of envelope attraction presented in Section 4.3.2 demonstrates that the model predictive controller will utilize maximum actuator authority to bring the vehicle back into the envelope. The extreme and unlikely case of a sudden drop in the friction coefficient from 1.0 to 0.1 demonstrates that while the dynamics of the vehicle and the actuators prevent the controller from driving the states directly into the envelope, the controller achieves the best possible return to the envelope, providing maximum assistance to the driver in maintaining stability.

# Chapter 5

## Real Time Estimation

In order for the controller described in the previous chapter to work in real world driving conditions, the boundaries of the safe handling envelope must be continuously updated to reflect changing conditions in the environment. However, because direct measurement of the tire-road friction coefficient is impractical and GPS or optical measurements of the vehicle sideslip angle are relatively expensive and sometimes obscured, these quantities that dictate the size of the vehicle envelope must be estimated. This chapter describes the integration of the envelope controller with an estimator that utilizes inexpensive and readily available steering effort and chassis inertial measurements to produce estimates of these important quantities that are suitable for use in the model predictive envelope controller. Despite the challenges of estimation and control on a highly variable surface, experimental results demonstrate that the coupled system is capable of suitably restricting the vehicle motion and preventing undesirable vehicle behavior.

### 5.1 Estimation Technique

The estimation technique chosen to supply slip angles and real time friction information to the envelope controller utilizes steering torque and steering angle measurements to supplement measurements of yaw rate and lateral acceleration supplied by standard automotive grade inertial sensors. This coupled slip angle and peak force

estimator is the same structure as the one presented by Hsu and Gerdès in [31].

### 5.1.1 Slip Angle Estimation

The slip angle dynamics for the front axle are straightforward to derive from the bicycle model. Assuming small angles and constant longitudinal speed, the derivative of the front slip angle is

$$\dot{\alpha}_f = \dot{\beta} + \frac{a}{U_x} \dot{r} - \dot{\delta} \quad (5.1)$$

where  $\dot{\beta}$  and  $\dot{r}$  are defined by the basic bicycle model equations as presented in Equation 2.15. With these relationships substituted, the front slip angle is seen to be a function of the front and rear axle forces, the yaw rate, and the steering rate.

$$\dot{\alpha}_f = \left( \frac{1}{mU_x} + \frac{a^2}{I_z V} \right) F_{yf} + \left( \frac{1}{mU_x} - \frac{ab}{I_z V} \right) F_{yr} - r - \dot{\delta} \quad (5.2)$$

The yaw rate and steering rate are directly measurable, but the lateral forces must be estimated simultaneously with the slip angle. Assuming these force estimates are available, the resultant observer dynamics for the slip angle estimate are

$$\dot{\hat{\alpha}}_f = \left( \frac{1}{mU_x} + \frac{a^2}{I_z V} \right) \hat{F}_{yf} + \left( \frac{1}{mU_x} - \frac{ab}{I_z V} \right) \hat{F}_{yr} - r - \dot{\delta} + K \left( \hat{F}_{yf} + \hat{F}_{yr} - ma_y \right) \quad (5.3)$$

where  $a_y$  is directly measurable and  $K$  is the observer gain. To obtain estimates of the forces, a single coefficient version of the brush tire model described in Section 2.1.1 is used in combination with the slip angle estimate. This model describes the lateral forces as a function of slip angle, normal load, and friction coefficient.

$$F_y = -C_\alpha \tan \alpha + \frac{C_\alpha^2}{3\mu F_z} |\tan \alpha| \tan \alpha - \frac{C_\alpha^3}{27\mu F_z} \tan^3 \alpha \quad (5.4)$$

The cornering stiffness,  $C_\alpha$ , can be estimated offline. Unfortunately, the normal load and friction coefficient vary in real time. However, these quantities appear only as a product with each other in the denominator of the tire force model. Therefore, a new

quantity referred to as “inverted peak force” may be defined as

$$I_f = \frac{1}{\mu F_z}, \quad (5.5)$$

reducing the real time task to that of estimating a single parameter. The resulting tire model, written in terms of the inverted peak force, is

$$F_y = C_\alpha \tan \alpha - \frac{C_\alpha^2 I_f}{3} |\tan \alpha| \tan \alpha + \frac{C_\alpha^3 I_f}{27} \tan^3 \alpha. \quad (5.6)$$

Thus, with an estimate of  $I_f$ , the necessary sideslip angle and peak force may be calculated and used to inform the model predictive envelope controller. Since normal load can be roughly estimated from the lateral and longitudinal acceleration measurements and an *a priori* measurement of vehicle mass,  $F_z$  can also be readily estimated. Therefore, it is straightforward to convert between  $I_f$  and  $\mu$  and these quantities will be used interchangeably in the description of the coupled estimation and control structure.

### 5.1.2 Peak Force Estimation

To understand the inverted peak force estimation scheme, one must first understand the mechanism by which tire forces generate torques about the steering axis. There are three tire forces that are reacted by the suspension: the lateral force, the normal load, and longitudinal force from drive and braking. In a typical suspension design, the steering axis is inclined in both the lateral and longitudinal directions. The resulting angles between the steering axis and the vertical direction are referred to as the kingpin and caster angles, respectively, as seen in Figure 5.1. In many suspension designs, these angles result in the intersection of the steering axis and the ground being offset from the center of the tire contact patch. In the lateral direction, this offset is referred to as scrub radius, while in the longitudinal direction, it is referred to as trail.

The torque that the steering system of the vehicle must resist is produced as a result of these offsets and the forces generated by the tire. Because the lateral force

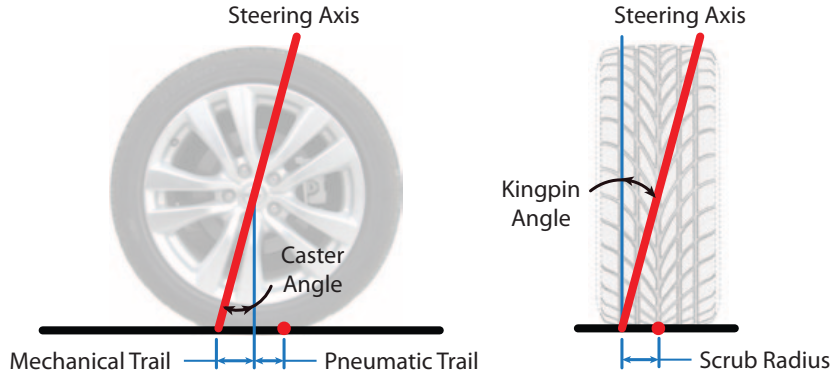


Figure 5.1: Steering Axis Geometry

is dependent on the slip angle and friction coefficient, measuring this torque provides a means for real time estimation of both quantities. However, the moment arm in the lateral direction is comprised of two separate lengths from which the resultant torques provide different information to the estimation scheme. The first portion of the moment arm is a result of the suspension geometry. Referred to as mechanical trail, the moment arm is the distance in the longitudinal direction from the steering axis intersection with the ground to the center of the contact patch. Depending on the suspension geometry, this length may change with steering angle and suspension deflection, but does not depend on the state of the tire. The product of this moment arm and the lateral tire force results in a steering torque proportional to the lateral force and is one component of what is called the aligning moment due to its tendency to rotate the tire into the zero slip, straight-ahead configuration.

The second component of the moment arm in the longitudinal direction varies due to the variation in the effective application point of the lateral forces generated in the contact patch as described in Chapter 2. The offset of the lateral tire force from the center of the contact patch is referred to as pneumatic trail. For the purposes of the estimator described in this chapter, the pneumatic trail is modeled as decreasing linearly with increasing slip angle until the tire saturates; beyond this angle, the pneumatic trail and associated steering torque are zero.

In addition to the aligning moment, there are also torques generated by the vertical

and longitudinal tire forces. Since the normal force on the tire acts roughly at the center of the contact patch, this offset of the steering axis results in a moment arm that causes a torque to be exerted about the steering axis. This is known as jacking torque and varies only with changing normal load. Although this normal load changes with the dynamic state of the vehicle, it does not provide useful information for estimating the friction coefficient. Thus, for use in the estimator, the jacking torque is estimated from other vehicle state measurements and removed from the total steering torque measurement.

The drive and braking torques on the wheel also result in torque being applied to the steering system. The component of the scrub radius that is perpendicular to the steering axis defines the moment arm for this effect. This torque can also be calculated and removed from the steering torque measurements used for estimation, but for tests performed with the P1 experimental testbed, no drive or braking torques are applied to the front axle during estimation and so no compensation is necessary.

Thus, the aligning moment needed for estimation can be found from the steering torque measurement by subtracting the jacking torque and any dynamic effects from the wheel and tire assembly:

$$M_{\text{align}} = M_{\text{loadcell}} - F_z l_{\text{jacking}} - b_{\text{damping}} \dot{\omega}_{\text{wheel}} - \text{sgn}(\dot{\omega}_{\text{wheel}}) F_{\text{coulomb}} \quad (5.7)$$

where  $M_{\text{loadcell}}$  is the steering effort measured by load cells in the steering tie rods,  $l_{\text{jacking}}$  is the jacking moment arm calculated from the suspension geometry, and  $b_{\text{damping}}$  and  $F_{\text{coulomb}}$  are found through system identification of the steering and suspension systems. The resulting aligning moment may be used to generate an estimate of the pneumatic trail if the mechanical trail is known and an estimate of lateral force is available, as seen from the following equation.

$$\hat{t}_p = -\frac{M_{\text{align}}}{\hat{F}_{yf}} + t_m \quad (5.8)$$

In the case of the coupled observer structure presented here, the lateral force estimate from the previous time step is utilized to generate the pneumatic trail value.

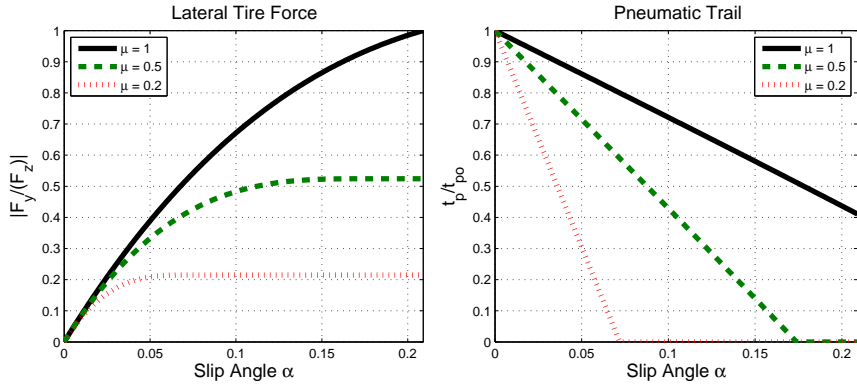


Figure 5.2: Lateral Force and Linear Pneumatic Trail Models

The benefit of calculating pneumatic trail for estimation is clear from Figure 5.2, which illustrates the evolution of lateral tire forces and pneumatic trails for various friction conditions as the slip angle of the tire increases. At low slip angles, the lateral tire force is unrelated to the friction coefficient and yields no information for the estimator. However, the model of pneumatic trail illustrated in Figure 5.2 decreases linearly with slip angle and friction coefficient until tire saturation and thus can be used to interpret the inertial and steering torque measurements to arrive at an estimate of the peak force capabilities of the vehicle. This piecewise linear model for pneumatic trail can be expressed as:

$$\hat{I}_f = \begin{cases} \frac{3(t_{p0} - \hat{t}_p)}{t_{p0} C_\alpha |\tan \hat{\alpha}|} & \text{if } \hat{\alpha} \leq \tan^{-1} \left( \frac{3}{C_{\alpha_f} I_f} \right) \\ \frac{|M_{meas}|}{t_m} & \text{otherwise} \end{cases} \quad (5.9)$$

where  $t_{p0}$  and  $C_\alpha$  are estimated offline and  $\hat{\alpha}$  is the previous front axle slip estimate. This coupled estimation process is outlined in Figure 5.3. A proof that the coupled structure is stable is presented in the work by Hsu and Gerdès [31].

### 5.1.3 Practical Considerations

Although the estimation scheme is capable of handling a wide range of driving conditions, there are regimes in which the estimator does a poor job of estimating as a result of limited excitation. To avoid the generation of poor estimates in these

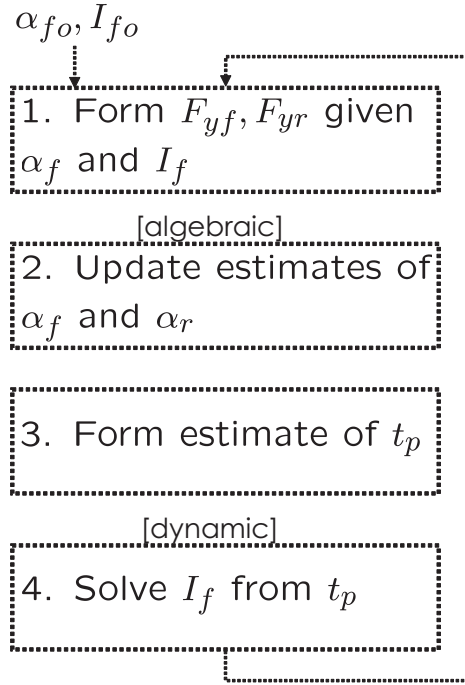


Figure 5.3: Coupled Sideslip and Friction Estimator Flowchart [31]

regimes, additional logic is added to the estimation structure.

The first of these logic switches is based on speed and causes the estimator to output default values of zero slip angle and unity friction coefficient if the speed is below  $3\frac{m}{s}$ .

The second logical case is when the front slip angle lies in the band of  $\pm 2^\circ$ . For most surface friction conditions, the front axle is within the linear region at these low slip angles and therefore it is very difficult to generate a good inverted peak force estimate. In this case, the estimator holds the previous value of the peak force and updates only the slip angle estimate.

The final logical case applied to the estimator prevents nonsensical values of pneumatic trail, since values greater than  $t_{p0}$  will yield a negative inverted peak force and negative values are undefined in the pneumatic trail model. Therefore, the pneumatic trail value is bounded between zero and  $t_{p0}$  to prevent unrealistic estimates from being produced.

## 5.2 Estimator Results

This section presents results from the use of the real time estimator on the P1 experimental vehicle operating on the highly variable gravel over asphalt surface described in Chapter 2. The performance highlights and limitations of the estimation technique are also described in this section.

### 5.2.1 Estimator Input Data Characteristics

The estimation technique used in this dissertation utilizes two inertial measurements, a calculated steering derivative, and steering torque measurements. Internally, the estimator seeks to match these measurements to a bicycle model of the vehicle behavior to produce estimates of the vehicle state. The data from these measurements are plotted in Figures 5.4, 5.5, and 5.6 without any filtering, aside from the anti-aliasing filters built into the data acquisition hardware. To generate the data shown in these figures, P1 was driven in a slalom maneuver followed by steady state cornering.

Figure 5.4 shows the yaw rate and lateral acceleration measurements. These measurements come from a standard Bosch MEMS accelerometer and gyroscope pair used for production ESC systems. While these sensors are not designed to be accurate enough for dead-reckoning use such as some inertial sensors in aircraft applications, the noise levels here are well below the excitation from the vehicle motion.

The steering rate data shown in Figure 5.5 are obtained by using a simple discrete approximation of the derivative of the steering angle. A 1000 line encoder is mounted to a force-feedback motor for the steering system on the test vehicle. Because the motor operates on the steering wheel through a harmonic drive with a 160:1 gear-ratio and very little backlash, this increases the effective encoder resolution to 160000 lines per revolution and allows for relatively clean differentiation of the steering angle, as seen in Figure 5.5.

Unfortunately, the signal-to-noise ratio in the measurement of the steering torque is not as good as in the inertial measurements and the steering rate. Figure 5.6 shows the aligning moments about the steering axis, obtained through direct measurement of the force in the steering tie rods with load cells. Effects of jacking torque and

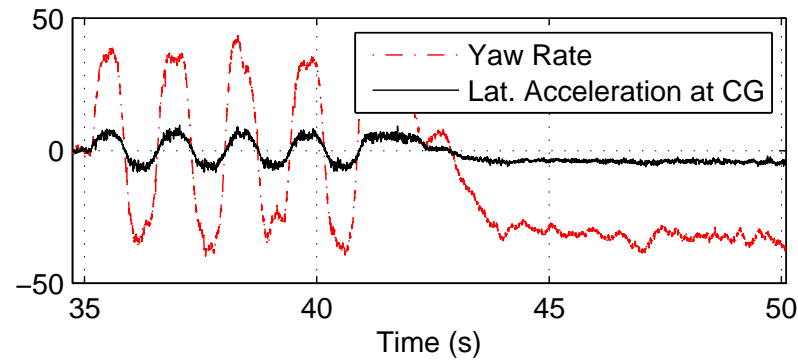


Figure 5.4: Representative Inertial Measurements

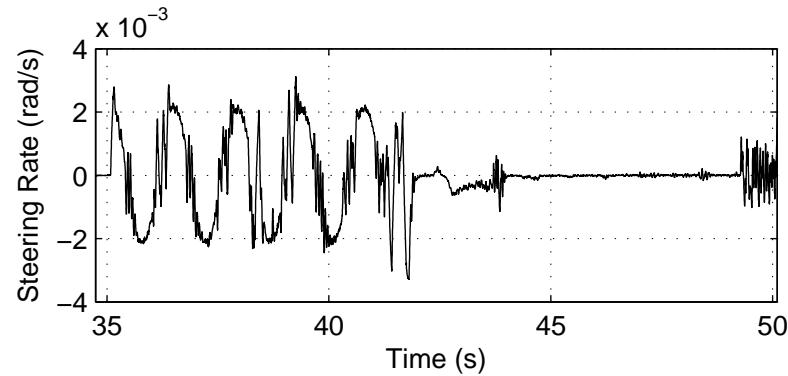


Figure 5.5: Representative Steering Derivative

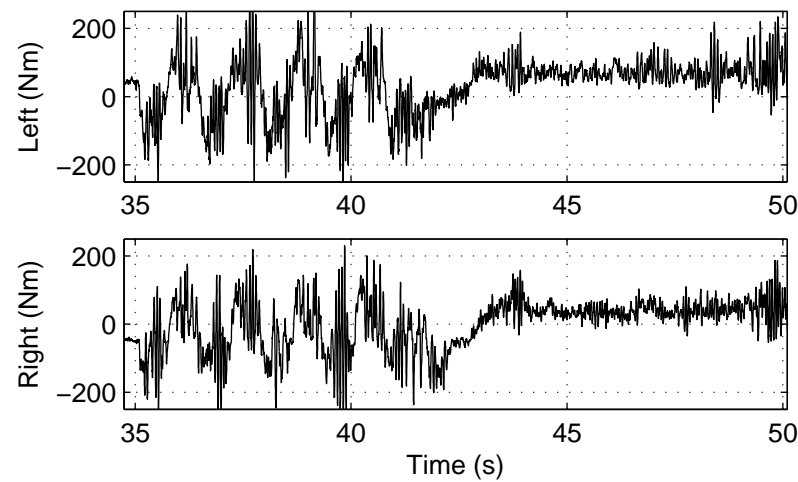


Figure 5.6: Representative Aligning Moments

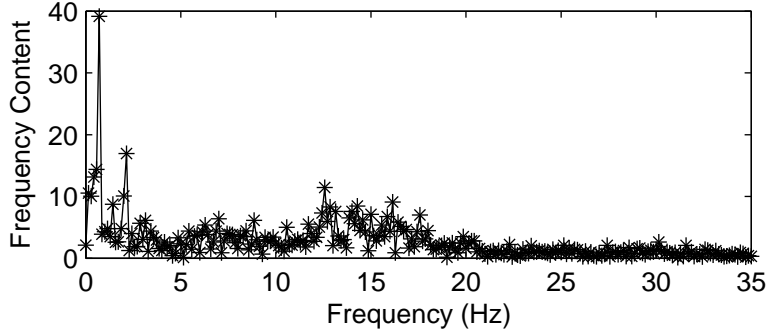


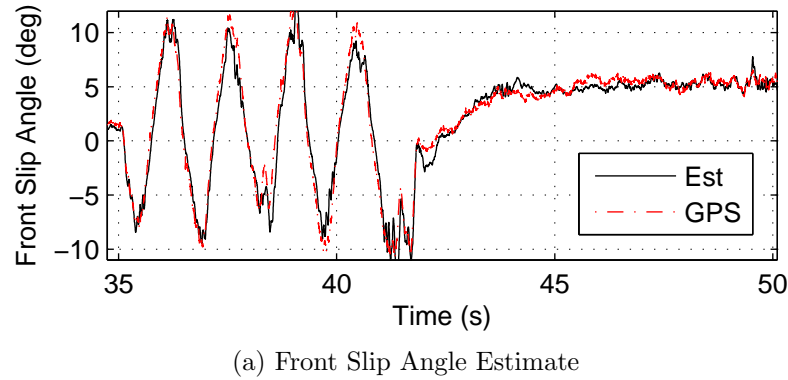
Figure 5.7: Aligning Moment Frequency Content

damping have been subtracted from the measurements to remove any known torque components not coming from the aligning moment. This figure demonstrates the challenge in accurately estimating the quantities of interest on the variable gravel over asphalt surface. In the slalom portion of the maneuver, the aligning moment appears to be roughly sinusoidal with an amplitude of 100 Nm and variation of approximately  $\pm 100$  Nm. In the steady state cornering phase, the data is somewhat cleaner, but still includes quite a bit of variation.

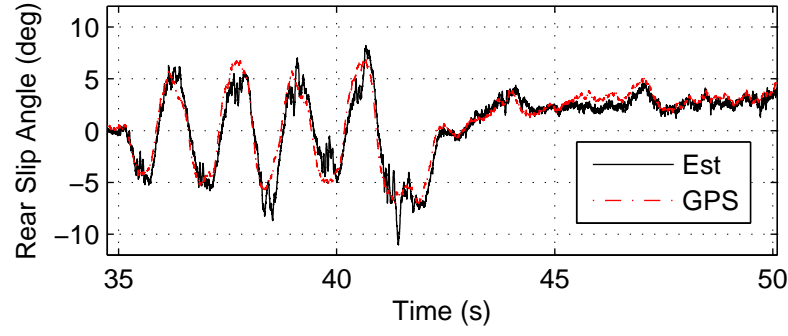
The significant difference in the noise characteristics between the aligning moment measurements and the inertial measurements is due, to a large extent, to the locations of the sensors. Because the load cells are attached to the steering tie rod, the possibility of undesired excitation exists. The tie rod is attached to the wheel, which experiences suspension modes such as the tire hop mode around 15 Hz and body pitch and heave modes around 2 Hz. The ideal suspension model assumes that these vertical motions are decoupled from the steering, but Figure 5.7 demonstrates that these frequencies appear in the aligning moment measurement both at their primary frequencies and with subharmonics and harmonics. In addition to the non-idealities of the suspension, the location of the sensor also has a direct effect due to the small unsprung mass. Unlike the inertial sensors, for which the excitation is limited by the inertia of the chassis, the load cells are subject to all of the variations in force generated by the tire as it encounters different amounts of gravel on the driving surface. One approach to handling this measurement would be to use a filter to restrict the

frequency content in the signal, but experiments with this approach demonstrated that the filters necessary to improve the magnitude response of the signal resulted in phase delays that were unacceptable for use in real time control. Therefore, the signals were left unfiltered and the signal variation was handled within the estimation structure.

### 5.2.2 Slip Angle Observer Results



(a) Front Slip Angle Estimate



(b) Rear Slip Angle Estimate

Figure 5.8: Slip Angle Estimates

While the observer structure couples together the friction and front slip angle estimation, it is instructive to examine the two parts of the estimator separately. In the slip angle observer, the derivative of the slip angle is calculated using only previous estimates and the yaw rate and steering rate measurements, as seen in Eq. 5.3. As

demonstrated in the previous subsection, these measurements have a better signal-to-noise ratio than the steering torques and allow for a reasonably clean estimate of the slip angle derivative. The difference between the sum of the front and rear axle forces and the lateral acceleration measurement is also used to correct the slip angle dynamics. Using these data, the slip angle portion of the estimator works well, as illustrated by Figures 5.8a and 5.8b. By avoiding any prefiltering of the inputs and utilizing the relatively clean inertial measurements, the slip angle estimation achieves good tracking of the GPS “truth” measurement without significant delay. However, the variation in the force measurements does appear in the estimate, becoming particularly obvious at the peaks of the slalom where Figure 5.6 shows the largest variation in the signal.

### 5.2.3 Pneumatic Trail and Friction Results

The friction estimation portion of the estimator relies on the slip angle estimate and the aligning torque information. As in the previous section, it is instructive to examine the results of the estimation separately despite the coupling of the estimator. Peak force capability, and thus friction coefficient, is calculated through the intermediate quantity of pneumatic trail, assuming the linear relationship illustrated in Figure 5.2. Figure 5.9 shows the pneumatic trail values calculated for the left and right wheels for the same data set used for the previous results.

This figure makes the difficulty in calculating friction coefficient from the aligning moment measurement relatively clear. The results of the previous section demonstrate that the slip angle estimate is reasonably accurate throughout the maneuvers. Therefore, the majority of the variability in the peak force estimate is a result of the variability in the input data. Examining Figure 5.9 and recalling the relationship between slip angle and pneumatic trail illustrated in Figure 5.2, it is clear that the pneumatic trail is generally following the trend that is expected from the vehicle dynamics. As the vehicle corners, the pneumatic trails decrease in response to the increased lateral force with the more lightly loaded wheel getting close to saturation

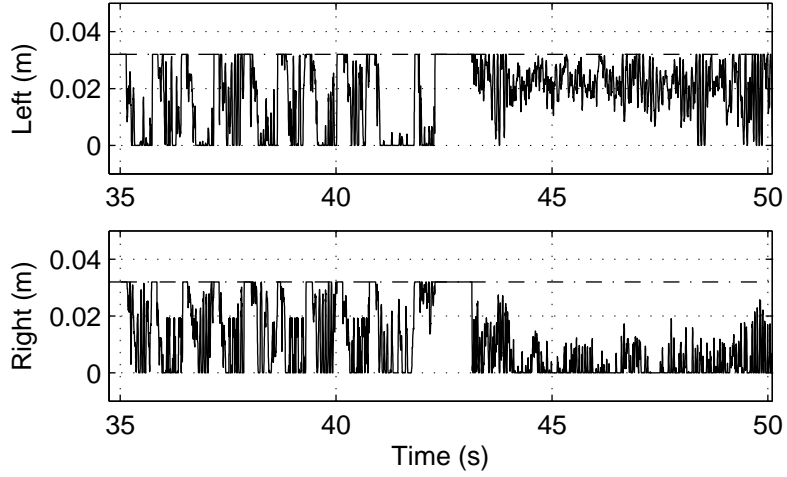


Figure 5.9: Calculated Pneumatic Trail

as indicated by the pneumatic trail nearing zero. However, the variation in the aligning moment measurement can be seen in the large changes of the pneumatic trail between the initial value, assumed to be 0.04 m, and zero. In particular, between 37 and 38 seconds, the pneumatic trails vary though nearly the full range, despite the vehicle dynamics being significantly slower than frequency in this variation.

In order to reduce the variation in peak force, the calculated values are fed into a moving average filter with a 300 sample window, which restricts the bandwidth of the friction coefficient to 0.9Hz. Since the relevant yaw and sideslip vehicle dynamics are typically on this order, this filtering operation allows the estimator to achieve reasonable performance from both the slip angle and friction values without significantly compromising the dynamic performance of the estimation structure. Figure 5.10 shows the estimated friction value after being filtered.

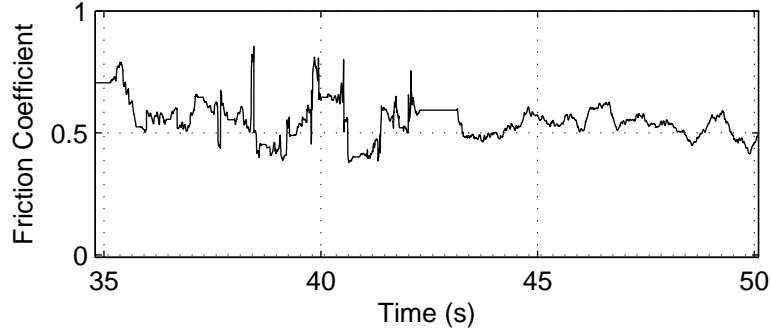


Figure 5.10: Calculated Friction Coefficient

### 5.3 Coupled Controller/Estimator Design

The incorporation of the estimator with the model predictive envelope controller was implemented in a straightforward manner. For real time implementation on the test vehicle, the estimator and controller were run on separate computers, connected via a CAN bus. The estimator was run at the 500Hz sampling rate of the primary computer while the controller was run at 100Hz as before to allow time for the MPC computations. Therefore, estimates of the slip angles and friction coefficient were sent to the controller via CAN messages after every 5 time steps.

Additionally, the friction coefficient output from the estimator was passed through a secondary selective moving average filter before usage in the envelope controller. This 25 sample filter was updated only when the steering rate fell below a very restrictive threshold of  $0.005 \frac{rad}{s}$ , which was selected by examining previous aligning moment data and friction estimates. This criterion ensures that the friction estimates are only averaged when the vehicle is near steady-state and the steering torque measurement is least variable. In the interim periods, no filter update was performed, resulting in the previous value being held until the next steady steering period. The resulting friction estimate can be seen in Figure 5.11, where the estimate from prior to the start of the plot time scale was held constant up to the completion of the slalom maneuver and the beginning of steady-state cornering. Previous experiments with over- and under-estimated *a priori* friction values suggest that the controller is capable of

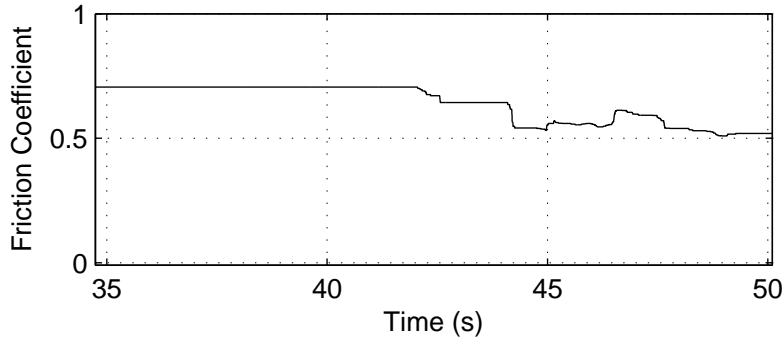


Figure 5.11: Calculated Friction Coefficient

handling a 20% to 30% friction mismatch. Therefore, for smooth controller action and better passenger comfort, it was deemed better to update selectively to restrict variation in the friction coefficient estimate.

The controller was also adapted slightly for better coupled operation with the estimator. This adaptation is in the post-processing phase of the controller, where a steering angle is determined from the lateral force output of the optimization. In the controller results presented in Chapter 4, the steering angle was always chosen to achieve exactly the desired force without allowing any significant understeer. However, this algorithm limits the achievable front slip angle, and in the case of a friction underestimate, prevents the front axle from utilizing the full potential of the tires to generate lateral force. This situation is made even worse by the fact that the friction estimator cannot obtain sufficient excitation to improve the estimate while in this situation. Therefore, in cases where the optimization output demands the maximum lateral force, the driver input is not altered so long as the front slip angle is past the point where the tire is fully saturated. Results later in this chapter will demonstrate the advantage of this change in the algorithm.

## 5.4 Control Results with Real Time Estimation

The results presented in the previous sections demonstrate the viability of the real time friction and slip angle estimation technique. This section presents results from

the operational estimator-controller system, demonstrating the intended behavior of the complete system as well as a few instances where the coupling of the two subsystems required careful consideration to reduce undesirable interactions.

### 5.4.1 System Convergence

The first set of results presented here illustrate the convergence of the estimator from initialization at the beginning of a test run. The plots in Figure 5.12 show the vehicle initiating and traversing a moderate left turn at approximately  $10\frac{m}{s}$ . Figure 5.12a shows the evolution of the friction coefficient estimate throughout the turn. The initial value of the estimate is set to 1.0 and is held until the front slip angle passes the estimation threshold. After obtaining sufficient excitation, the estimator converges to the correct range of approximately 0.5 to 0.6. The coupled estimator simultaneously produces a front slip angle estimate that agrees with the value measured with GPS. Figure 5.12d also shows the slow movement of the input steering angle to ensure that the steering rate constraint was satisfied and the friction coefficient post-filter was continuously updated.

### 5.4.2 Coupled Operation

The next set of results, presented in Figure 5.13, demonstrate the proper functionality of the combined system when the vehicle is driven to the limits of its handling capabilities on the gravel surface. In this test, the envelope boundaries were set to  $\pm 15^\circ$  rear slip angle limit and 115% of the maximum steady-state yaw rate allowed at  $0^\circ$  sideslip angle. The resulting envelope is very similar to that shown in Figure 3.9 with slightly smaller rear slip angle bounds. The slack weight associated with the yaw boundary was also lowered to  $5 \times 10^2$  to reduce the controller effort in correcting small oscillations in the yaw rate around the bound as will be illustrated in the subsequent section.

Figure 5.13 shows the estimated friction coefficient, limited quantities, steering angles, and longitudinal vehicle speed for the maneuver, which includes three step steers with a return to straight driving in between each. The maneuver was performed at

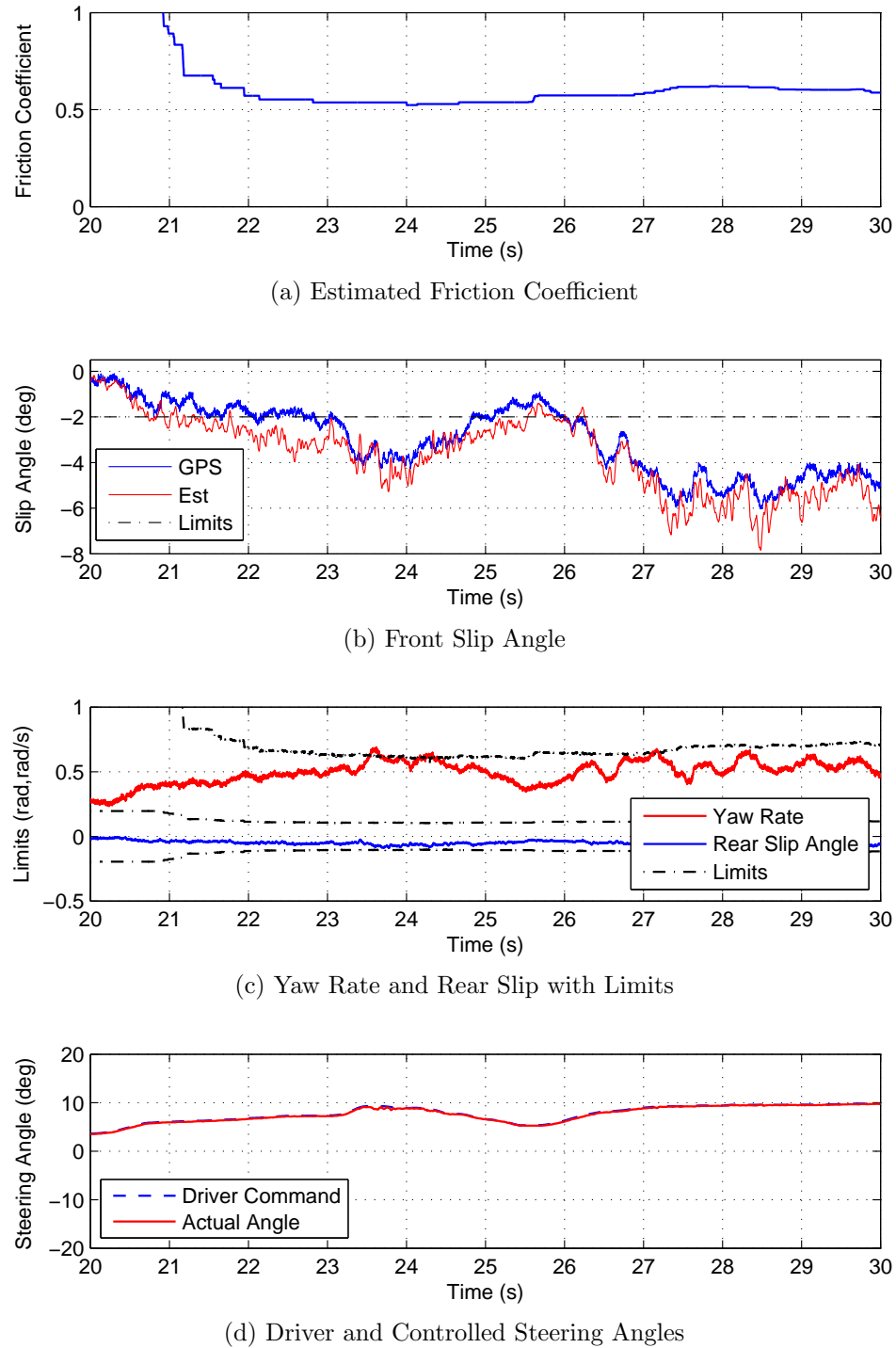


Figure 5.12: Convergence of the Friction Estimate under Envelope Control

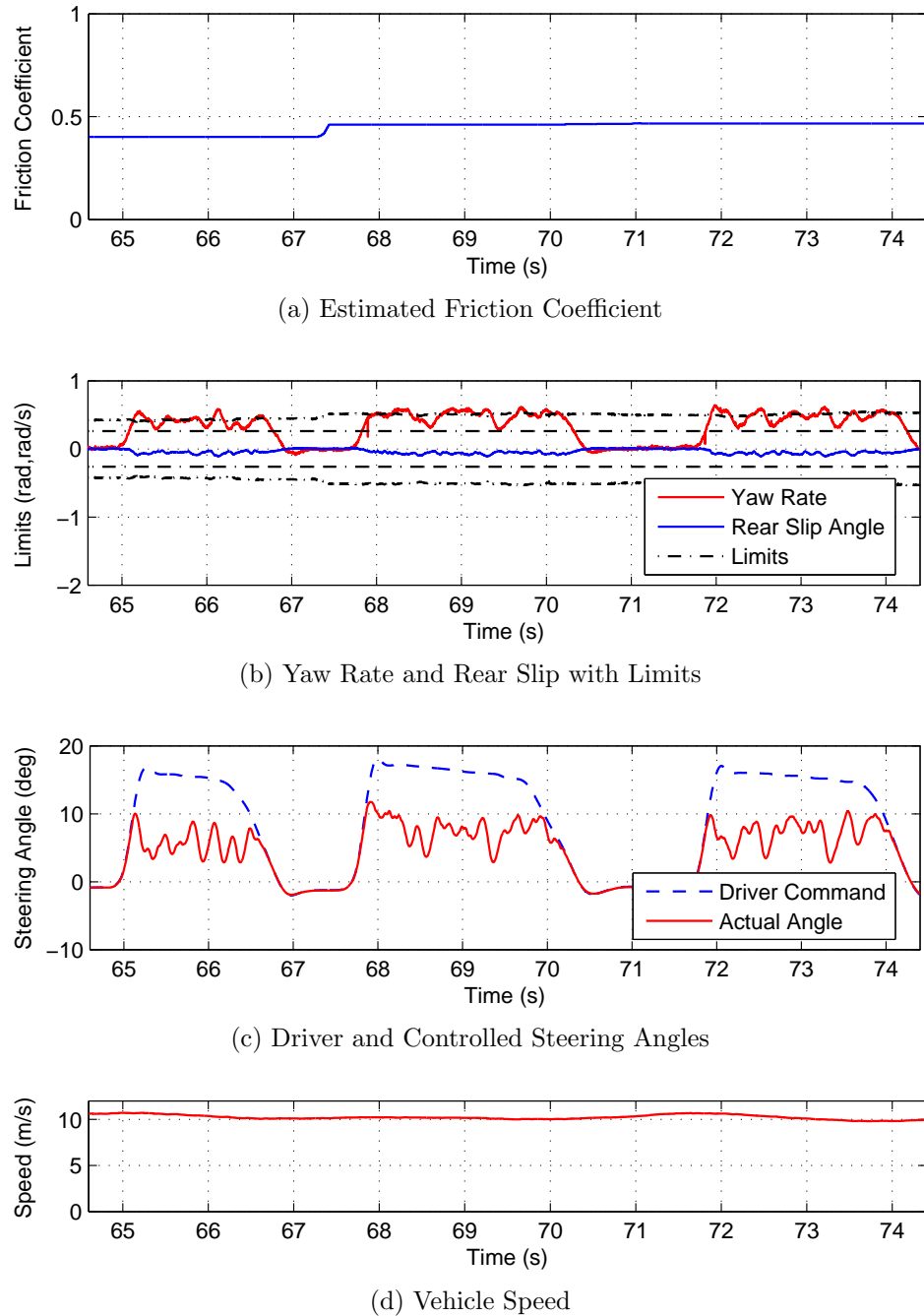


Figure 5.13: Envelope Control with Real Time Slip and Friction Estimate

$10\frac{m}{s}$  with cruise control, which was employed to maintain a constant speed, but also to minimize rear wheel drive torques. Unlike the maneuver presented in Figure 5.12, in this maneuver the natural yaw and sideslip oscillations of the vehicle caused the controller to make frequent steering corrections. Thus, the friction estimate was updated less frequently as a result of the friction post filter. The estimated value is slightly outside of the expected range between 0.5 and 0.6, likely an effect of unmodeled rear wheel torques that reduce lateral grip. Figure 5.13b shows that given this friction coefficient and the real time estimates of slip angle, the yaw rate and rear slip angle are effectively limited to the boundaries of the envelope by the steering corrections of the controller, seen in Figure 5.13c.

### 5.4.3 Controller Parameter Sensitivity

Perhaps as interesting as achieving a successful integration of the controller and estimator are the subtle dynamics that occur due to the coupling of the two subsystems. One of these is the sensitivity of the controller to variation in the slip angles from the estimator. As seen in Figure 5.8, the slip angle estimates are noisier than the GPS-measured values, particularly at large slip angles. This makes sense given the structure of the estimator. Because of the nonlinear relationship between force and slip angle of a tire, a small change in estimated force near the peak of the tire curve results in a very large change in slip angle estimate. Therefore, the estimator is highly sensitive to variation when near the limits of the tire grip. The result is that when large values are chosen for the yaw rate slack weight, the controller responds to this variation by rapidly slewing the steering system. The extra actuator effort is unnecessary and undesired as it generates significant and uncomfortable accelerations for the passengers and degrades the handling.

Figure 5.14 illustrates the controller behavior when the slack penalty weights for both the yaw rate and rear slip angle are set to  $5 \times 10^4$  in a steady-state cornering maneuver. All other controller parameters are the same as the previous results. As the maneuver is initiated, the yaw rate and rear slip constraints are reached and the controller must countersteer. However, a combination of noise in the estimates

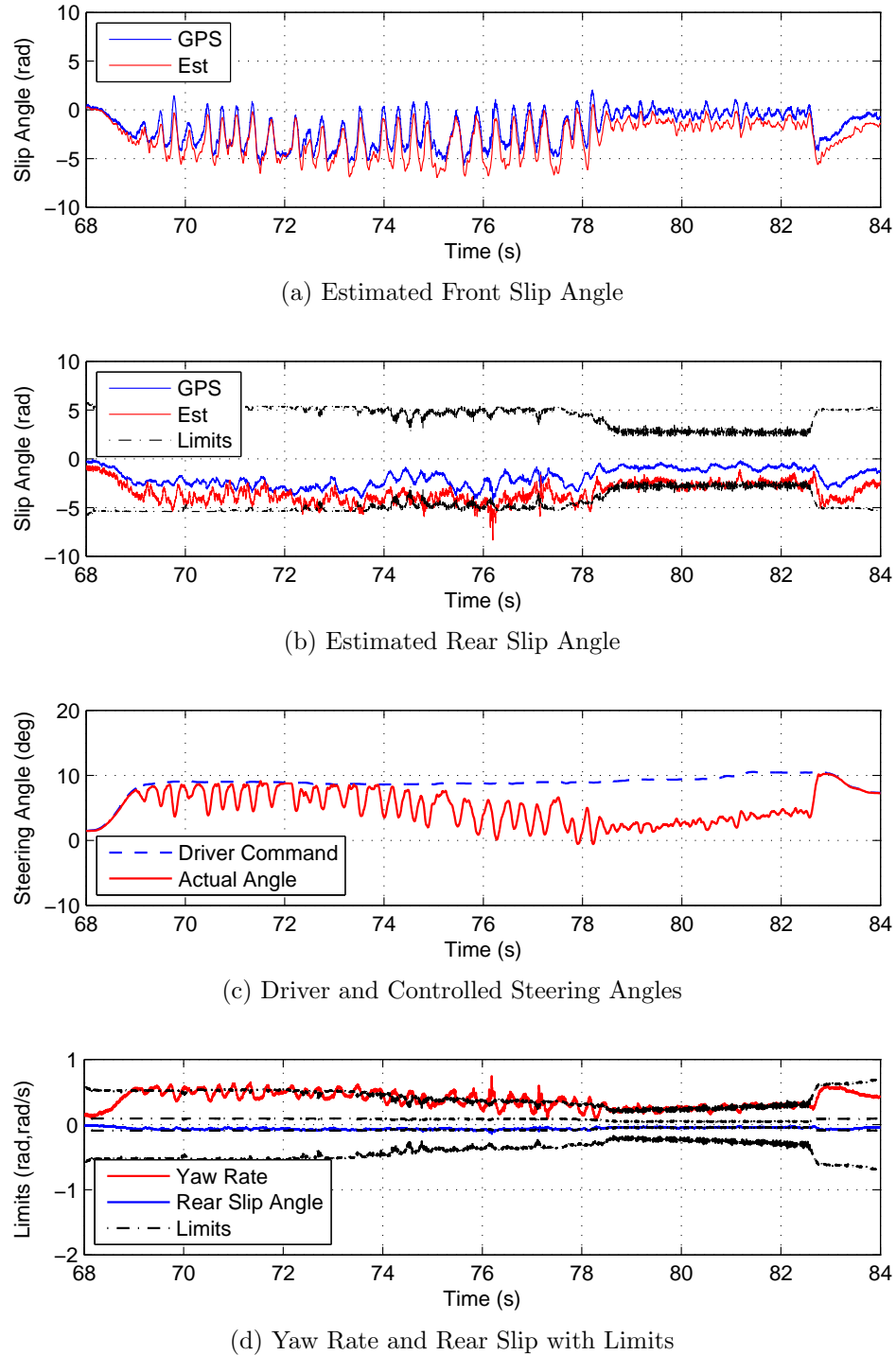


Figure 5.14: Envelope Control Over-response with Real Time Slip and Friction Estimate

and real variation in the yaw rate result in strong steering responses in the coupled estimator-controller system. Figures 5.14a, 5.14b, 5.14c, and 5.14d demonstrate the system response in this case. Notice that the vehicle actually remains very close to the yaw rate and rear slip angle limits. Absent of considerations of human comfort, the results in Figure 5.14d would seem excellent. However, the extra steering input makes the car difficult to drive and degrades the driver's understanding of the assistance system behavior at the limits of handling. Furthermore, the boundaries of the envelope are only known approximately. Therefore, softening the constraints allows the controller to generally respect these approximate boundaries without over-controlling the vehicle.

#### 5.4.4 “Locked-low” Operating Regime

Another interesting interaction of the estimator and controller is a situation that can occur due to an underestimation of the friction coefficient and subsequent conservatism of the controller. Accurate estimates of friction coefficient may be obtained only after the front axle reaches 30-50% of the slip angle needed to saturate the tires. If the estimator produces a very low friction estimate and the controller enforces the artificially low limits, the combined system may prevent the front axle from developing sufficient excitation to obtain a better estimate. This case is exacerbated by logic in the estimator that stops estimation if the slip angles are within the range of  $\pm 2^\circ$ . In this case, the vehicle will be restricted to very low yaw rates, as seen in Figure 5.15 which includes steady cornering and a slalom.

Figure 5.15a shows the friction estimate throughout the maneuver. Prior to the section of the data set plotted, the friction estimate dropped low. As a result, the estimate remains consistently low as there is insufficient excitation to improve the estimate. This is because of the drastic controller intervention, as seen in Figure 5.15c, where the steering angle is severely limited. Note that the controller does a good job of maintaining the vehicle within the artificially low boundaries, even though this results in a significant reduction of the vehicle performance compared with the maximum possible capabilities on the driving surface.

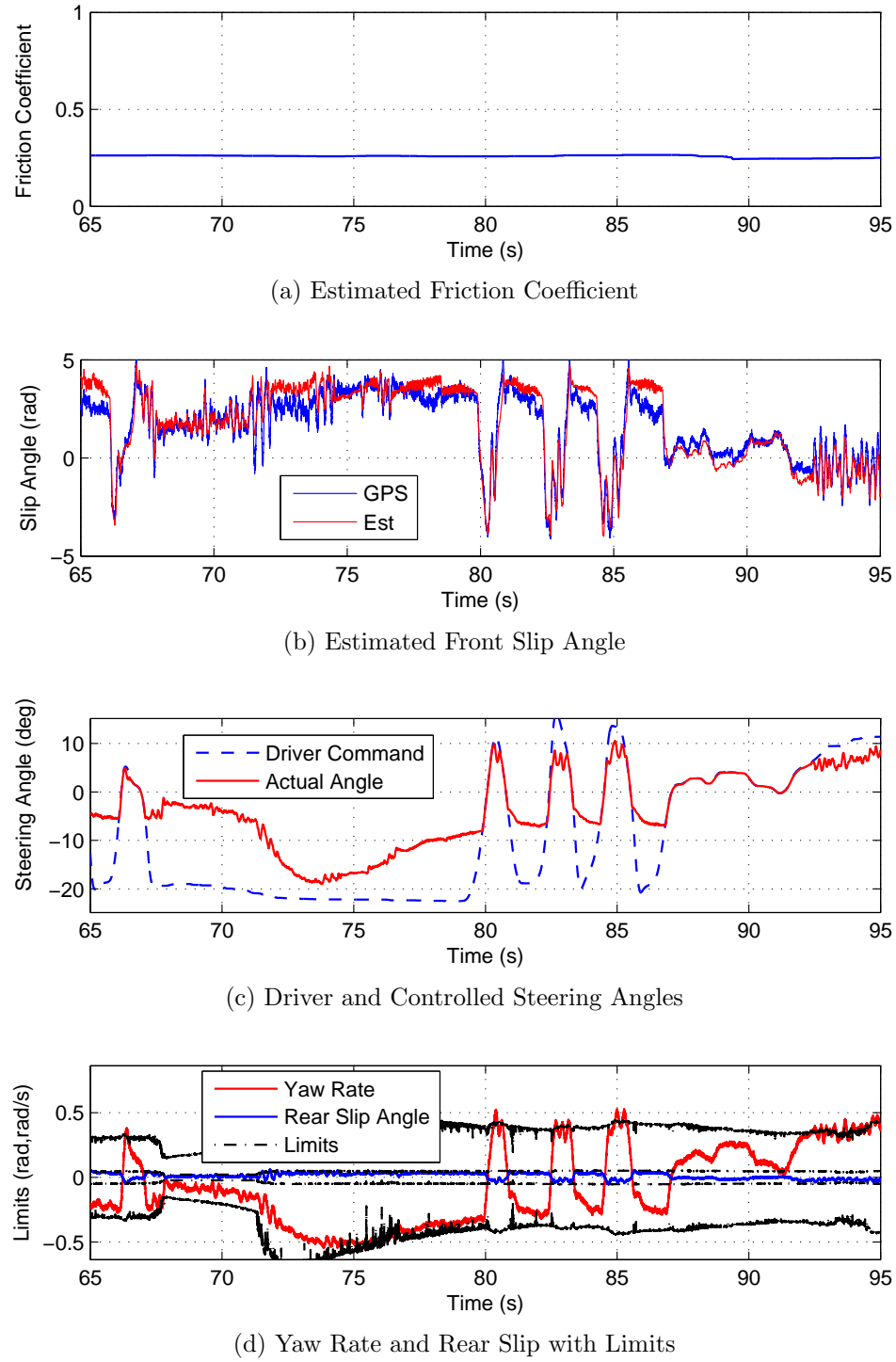


Figure 5.15: “Locked-low” Coupled System Operation

The alternative logic described in Section 5.3 that allows the driver to attain large front slip angles in cases where countersteering is not necessary can provide some excitation to the controller. The extended yaw rate bound for the MPC envelope also allows the front slip angle to reach higher slip angles in non-critical situations. However, once the yaw rate or rear slip angle limits are reached, the controller will slew the wheels into a countersteer and control the front slip angle to a small value. Other ad-hoc solutions may be possible, including artificially ramping the friction estimate to “feel” for higher levels of friction or providing a small offset from the real value to provide additional excitation to the estimator.

## 5.5 Discussion

The results presented in this chapter, particularly Figure 5.13, demonstrate the viability of a GPS-free envelope control system using low cost inertial sensors and readily available steering torque measurements. The robustness of the model predictive envelope controller allows the system to handle variation in the estimator output as a result of the rough gravel surface, while the slack weights on the yaw rate and rear slip angle boundaries allow the controller to automatically handle small natural oscillations in the vehicle dynamics around the envelope boundaries without exerting unnecessary control effort. The final system design correctly detects the lowered friction condition, adjusting the steering angle smoothly and appropriately to prevent the vehicle from spinning out or sliding sideways.

# Chapter 6

## Extensions of Envelope Control

The previous chapters of this dissertation have presented a framework for developing a driver assistance system with model predictive control that takes advantage of the inherent structure of MPC to track the desired vehicle trajectory, provided that it does not exceed the limitations of the vehicle's handling capabilities. This chapter utilizes the same conceptual framework to control the roll states of the vehicle while attempting to the nominal planar vehicle behavior of the uncontrolled vehicle. This structure facilitates coordination with the driver since the vehicle behaves in accordance with the driver's internal model except in extreme cases where the controller must drastically alter the planar behavior to prevent a dangerous roll situation.

### 6.1 Control of Roll Dynamics

It is well known that vehicle rollovers are particularly dangerous situations for the occupants of a vehicle. Data from the U.S. NHTSA shows that occupants in a rollover event are more than ten times more likely to be fatally injured than in a nonrollover accident [65]. Coupled with the fact that high-CG vehicles (Sport Utility Vehicles) have been popular with American automotive consumers in the last decade, these trends suggest that systems that actively control the vehicle dynamics to prevent rollover events create significant safety benefits for consumers.

As a result of this high rate of injuries and fatalities, there has been a significant

amount of work on rollover prevention with authors focusing on varied aspects of the problem. The Ford Motor Company has developed the Roll Stability Control system which has been installed on select Ford Motor Company vehicles since model year 2003 [36]. This system uses a series of estimation techniques to identify an imminent rollover and applies a hard braking input to a single wheel to mitigate the rollover event. Other authors such as Chen [13] and Yoon [35] have focused on developing metrics for assessing rollover risk that are then used to trigger a specific rollover prevention action [13, 35]. In [60], the authors even propose a scheme to control and correct the vehicle behavior after tire lift-off has occurred. In this chapter, the model predictive control framework used for planar envelope control is adapted to coordinate the trade-offs that must be made in the planar vehicle dynamics to control the roll states. Using rear wheel steering and rear wheel differential drive, two different controllers that restrict the vehicle roll rate in extreme maneuvers are developed. This approach to choosing the optimal actuator inputs facilitates a dramatic alteration of the vehicle roll state trajectory while maintaining the validity of the driver's internal model of the planar vehicle dynamics.

### 6.1.1 Control Approach

There are several objectives to consider in designing controllers to modify the behavior of the roll states. The control task is a challenging one due to the fact that most production vehicles, like the vehicles considered in this investigation, lack actuation of the roll dynamics and thus the roll states are excited indirectly by the forces generated by the tires. Unfortunately, this link between the planar behaviors of the vehicle and the roll motion of the body means that certain motions that may be desirable from a planar perspective are unobtainable without exciting potentially dangerous roll dynamics. Yet restricting the driver's ability to maneuver the vehicle may be equally dangerous. As a result, a trade-off must be made in real time to determine the least hazardous situation. Since rollover crashes are known to have a highly elevated injury and fatality rate, the control strategy is to use all available actuation to prevent the overturning of the vehicle, but whenever possible, minimize

the deviation between the driver's intended and the vehicle's actual behavior.

As with the planar envelope control presented in the previous chapters, a model predictive controller offers the opportunity to express this problem in terms of constraints on the roll states and costs on the differences between the nominal and controlled vehicle states. This allows for the system to coordinate the available actuators in order to preserve normal handling aspects of the vehicle, relieving the driver of the burden of controlling the vehicle in an unfamiliar regime. However, the controller does not incorporate information about road curvature or vehicle path. Instead, the system utilizes the driver's input to determine proper vehicle behavior by mapping the inputs to a linear model of the intended vehicle state trajectory. The driver is assumed to be capable of properly tracking the lane and avoiding obstacles provided the vehicle responds in the expected manner to the driver's inputs. However, drivers' internal models are typically more accurate for the planar dynamics of the vehicle than they are for the vehicle roll states. Thus, the linear model yields a model of the driver's intent that is likely appropriate for a large majority of drivers and the task of the control system is to make sure that the driver inputs are not capable of overturning the vehicle while minimizing deviation from the model of expected vehicle behavior.

Unlike the planar envelope controller presented in previous chapters, the strategy for controlling the roll dynamics of the vehicle utilizes multiple actuators. Clearly the roll states could be restricted through the use of front steering alone, but this would impose significant limitations on the lateral planar dynamics of the vehicle. To mitigate this intrusion into the lateral dynamics, a second actuator is utilized in coordination with the front steering. Rear wheel steering is one choice for this additional actuator, while the other is independent application of acceleration and braking torques to the left and right wheels of the vehicle. Both actuators can be found in certain production vehicles, although the ability to brake independent wheels is provided by standard ESC systems that are becoming standard on all production vehicles. More importantly, both actuators affect the planar and roll dynamics in different ways, allowing the controller to coordinate these actuators to simultaneously restrict the roll states and track the intended planar behavior.

### 6.1.2 MPC Expression

The model underlying the control scheme is a four-state linear model incorporating single-track planar dynamics and roll dynamics. Previous work by Carlson and Gerdes [12] showed that model predictive control of vehicle roll states is achievable in real time by using a simplified explicit solution to the problem. The system described in this chapter solves the model predictive control problem in real time to calculate an optimal set of inputs to minimize deviation from the uncontrolled state trajectory while respecting limits on the roll states and the actuators.

The controller itself is found by phrasing the problem as a linearly constrained quadratic problem, a subset of convex optimization problems that can be solved robustly and rapidly as described in [10]. The same framework that was introduced for planar envelope control can be used to phrase the roll control problem. Like the planar problem, there is a trajectory for the states that the driver intends that should be tracked when constraints on the actuators and states are satisfied. The linear roll model presented in Section 2.2.4 can be discretized to form the discrete state space description ( $x^{k+1} = A_d x^k + B_d u^k$ ,  $y^k = C_d x^k + D_d u^k$ ), allowing the model predictive control problem to be described by the following expression:

$$\text{minimize} \quad \sum_{k=1}^N \left\| x_{\text{opt}}^k - x_{\text{des}}^k \right\|_{W_x}^2 + \sum_{k=1}^{N-1} \left\| F_{yf}^k \right\|_{W_u}^2 + \eta \sum_{k=1}^N \left\| s_{\text{opt}}^k \right\|_1 \quad (6.1a)$$

$$\text{subject to} \quad x_{\text{opt}}^1 = A_d x_{\text{init}} + B_d u_{\text{init}} \quad (6.1b)$$

$$x_{\text{opt}}^{k+1} = A_d x_{\text{opt}}^k + B_d u_{\text{opt}}^k + B_d u_{\text{user}}, \quad (6.1c)$$

$$k = 1, \dots, N$$

$$|u_{\text{opt}}^1 + u_{\text{user}} - u_{\text{init}}| \leq u_{\text{slew}} \quad (6.1d)$$

$$|u_{\text{opt}}^{k+1} - u_{\text{opt}}^k| \leq u_{\text{slew}}, \quad (6.1e)$$

$$k = 1, \dots, N-1$$

$$|u_{\text{opt}}^k + u_{\text{user}}| \leq u_{\text{lim}}, \quad (6.1f)$$

$$k = 1, \dots, N-1$$

$$|x_{\text{opt}}^k| \leq x_{\text{lim}} + s_{\text{opt}}^k \quad (6.1g)$$

$$k = 1, \dots, N$$

$$s_{\text{opt}}^k \geq 0, \quad k = 1, \dots, N \quad (6.1h)$$

where the parameters for the MPC problem are listed in Table 6.1 and the optimization variables are  $x_{\text{opt}}^k$  for time steps  $k = 1, \dots, N$ , the optimal state trajectory,  $u_{\text{opt}}^k$  for time steps  $k = 1, \dots, N-1$ , the optimal input addition to the user input, and  $s_{\text{opt}}^k$  for time steps  $k = 1, \dots, N$ , the slack variables on the state limits (to prevent infeasible problems). Just as with the planar envelope control, these slack variables remain unused (zero-valued) unless the optimization problem is infeasible. In this expression of the problem, both the roll angle and roll rate are constrained, though the limits may be set so that either one of these constraints is never active in operation.

Table 6.1: Description of Roll Controller Parameters

Parameter	Description
$A_d$	Discrete State Propagation Matrix
$B_d$	Input Effect Matrix
$W_x$	State Tracking Weight Matrix
$W_u$	Input Penalty Matrix
$x_{\text{des}}$	Open Loop Trajectory from Driver Input
$x_{\text{init}}$	Vehicle State at Start of Optimization
$u_{\text{init}}$	Vehicle Actuator State at Start of Optimization
$u_{\text{user}}$	Driver Commanded Input (constant over the horizon)
$x_{\text{lim}}$	State and Input Limits
$u_{\text{limits}}$	Actuator Saturation Limits
$u_{\text{slew}}$	Limit on Rate of Change of Inputs
$\eta$	Stiffness of Slack Variables

### 6.1.3 Real Time MPC Implementation

Typically a MPC problem is solved at every time step to find an optimal input sequence from which only the first calculated input is utilized. However, the computation time for this problem is non-negligible and an input may not be calculated rapidly enough for the immediate time step. Instead, the input for the following time step is calculated, stored, and applied at the appropriate time. The input parameters can be varied between time steps. Thus, the controller limits can be computed in real time or adjusted with adaptive techniques.

To solve the MPC problem, the same convex optimization tools used for the planar envelope controller may be applied. This toolchain, CVXMOD [44], produces automatically generated C-code that can solve this roll control problem in less than 10 milliseconds on a modern Pentium processor chip. This is slightly longer than the results observed for the planar problem, which can be attributed to the additional states and dynamics required to describe the roll motion of vehicle.

The work done on this rollover prevention technique examines the possibility of using either rear differential drive or rear wheel steering to provide a needed additional degree of freedom to the base mode of the vehicle. The P1 experimental steer- and drive-by-wire research vehicle, described in Chapter 2 and shown in Figure 2.7, is equipped with independent drive motors for the rear wheels and has the capability to support testing of the differential drive concept. The rear wheel steering concept can be tested on a different platform, referred to as X1, that has also been developed by students in the mechanical engineering department at Stanford University. The X1 by-wire vehicle couples a modular chassis design with a distributed data collection and control system based on the Flexray communication standard and can be seen in Figure A.1. A more complete description of X1 can be found in Appendix A.

## 6.2 Simulation Results

### 6.2.1 Roll Control Objective

A number of criteria for preventing vehicle rollover events have been presented in previous publications. These include static stability criteria, time-to-rollover metrics, roll angle limits, and wheel lift criteria [68, 13, 35, 36]. The model predictive controller described in this chapter provides the mechanism for describing a linear limitation of the roll rate and roll angle. Since most production vehicles will lose tire grip before rolling over in a static maneuver, as demonstrated by the NHTSA rollover testing [68], it is assumed that non-tripped rollovers are caused by dynamic maneuvers such as the fish hook and J-turn that excite both large roll rates and roll angles. Therefore, the results presented in this section describe the vehicle behavior when the roll rate is restricted as an illustration of the potential of this assistance scheme.

### 6.2.2 Baseline Dynamics

As a baseline for the discussion of the results in this section, the uncontrolled vehicle behavior was examined in simulation using the nonlinear yaw-roll model to describe the vehicle behavior. This model, described in Section 2.2.1, includes degrees of

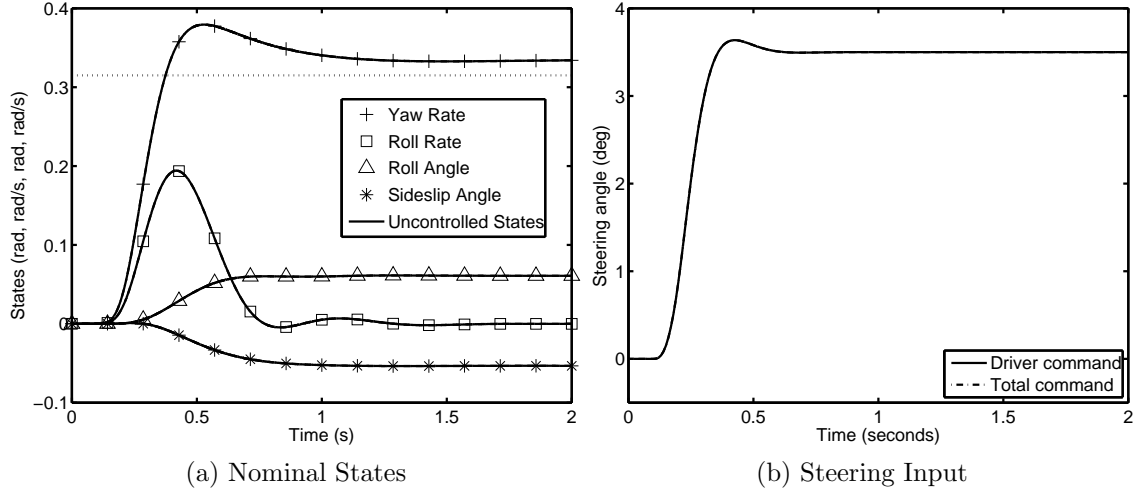


Figure 6.1: Vehicle state and input trajectories for baseline (inactive) case

freedom for yaw rate, sideslip angle, roll angle, roll rate, and independent wheel dynamics for all four wheels. A nonlinear brush tire model such as the one described in Section 2.1.1 was used to calculate the tire forces. Later simulations demonstrate the ability of the controller to restrict the roll rate to  $0.15 \frac{rad}{s}$  and  $0.18 \frac{rad}{s}$ , but in this case no restriction is specified and so the figures illustrate the nominal dynamics for the roll rate and roll angle of the uncontrolled vehicle. This case can be seen in Figure 6.1.

The driver's steering input for this simulation was generated by applying a 3Hz low-pass filter to a 3.5 degree fast ramp steer input. This filtering represents the limited capability that a human possesses to create extremely fast steering inputs. Data taken from research testbeds under manual driving supports the observation that nearly all of the frequency content of a driver's input signal is at or below 3Hz. Since the vehicle model incorporates the assumption that the vehicle travels at a constant speed, a “cruise control” function was used to keep the vehicle at 20 m/s for the duration of the maneuver.

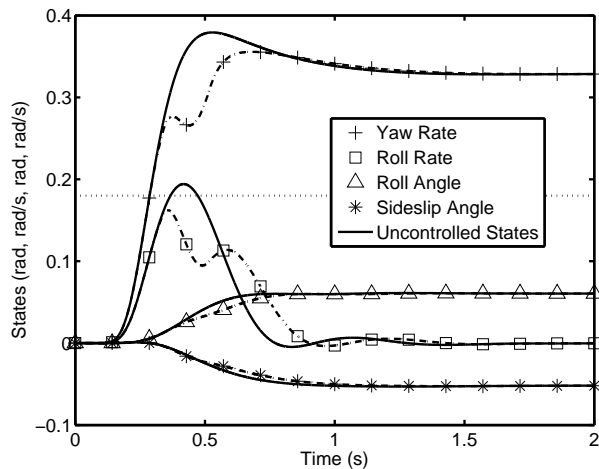


Figure 6.2: Vehicle state trajectories for drive/brake torque controller

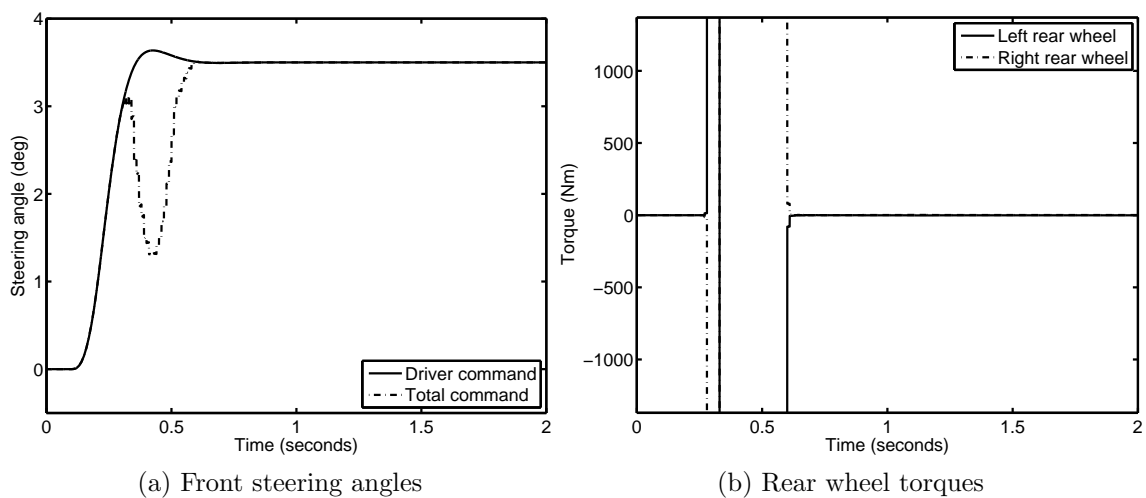


Figure 6.3: Inputs for controlled fast ramp steer with differential drive

Table 6.2: Independent Wheel Torque Roll Controller Parameters

Parameter	Symbol	Value	Units
roll angle limit	$x_{\lim}[1]$	$\pm 10$	deg
roll rate limit	$x_{\lim}[2]$	$\pm 0.18$	rad/s
front steer limit	$u_{\lim}[1]$	$\pm 20$	deg
wheel torque limit	$u_{\lim}[2]$	$\pm 1370$	Nm
torque slew limit	$u_{\text{slew}}[1, 2]$	$\pm 24000$	Nm/s
slack penalty	$\eta$	$10^6$	–
time horizon	$N$	15	–

### 6.2.3 Independent Wheel Torque Control

The first controlled case is the drive-brake controller, which uses independent control of the accelerating and braking torques on the rear wheels to complement the front steering actuator to achieve a restriction of the roll rate to  $0.18 \frac{\text{rad}}{\text{s}}$ . This roll rate was selected by examining the nominal dynamics of the vehicle and choosing a limit that would require significant controller intervention to achieve while still retaining much of the nominal vehicle behavior. Table 6.2 lists the full set of controller parameters used for the simulation.

The state trajectories as well as front steering and rear torque commands for the system under control of the drive-brake controller can be seen in Figures 6.2 and 6.3, respectively. In Figure 6.2, there is clearly a significant deviation from the nominal yaw rate trajectory. Examining Figure 6.3, there is a significant steering correction to control the roll rate while the rear-wheel torque saturates to the limits set to represent the maximum longitudinal force that the rear tires can produce. Despite saturating the longitudinal forces on the rear axle, the controller is unable to compensate for the yaw rate lost by reducing the front steering. This is a result of the geometry of the car and the coupling of the lateral and longitudinal forces. Because the width of the car is smaller than the length, very large differential longitudinal forces must be created to generate effective yaw moments. However, because of the coupled nature

of lateral and longitudinal force generation by the tires, large torques may not result in the desired longitudinal force, particularly if the vehicle is cornering aggressively. This reduces the effectiveness of differential torques as a means to regulate the roll dynamics of the vehicle.

In addition to the physical limitation of the independent torques, the coupled tire forces are challenging to represent in a convex formulation that is suitable for expressing as part of the model predictive control problem. Therefore, a linear model was utilized, along with a 100Hz sample rate that was expected to compensate for some of the reduction in the accuracy of the model. Thus, the nonlinear simulations presented here demonstrate the level of impact on the system due to the controller modeling assumptions. Despite having a linear model that leaves out this force coupling, the feedback aspect of model predictive controller is capable of controlling the roll rate. However, it is at the expense of tracking the yaw rate trajectory. Further reductions in the roll rate limit below  $0.18 \frac{\text{rad}}{\text{s}}$  result in significantly worse tracking of the yaw rate.

#### 6.2.4 Rear Wheel Steering Control

The second controller is a front- and rear-wheel steering controller. This controller was also simulated with the same nonlinear model and driver inputs used for the drive-brake controller. The state trajectories as well as front- and rear-wheel steering commands for the system can be seen in Figures 6.4 and 6.5, respectively. Note that in this example, the roll rate limit was lowered to 0.15 rad/s to demonstrate the performance of the controller in a case where the limit more significantly restricted the nominal vehicle dynamics. Table 6.3 lists the full set of controller parameters used for the simulation.

The behavior of the controlled system is improved when compared to the performance of the system when using the differential wheel torque actuator. In this case, the roll rate constraint is met and modification of the roll states results in significantly less degradation of the tracking of the uncontrolled system trajectory.

Like the differential torque controller, the necessary reduction in lateral force to

Table 6.3: Rear Steering Roll Controller Parameters

Parameter	Symbol	Value	Units
roll angle limit	$x_{\text{lim}}[1]$	$\pm 10$	deg
roll rate limit	$x_{\text{lim}}[2]$	$\pm 0.18$	rad/s
front steer limit	$u_{\text{lim}}[1]$	$\pm 20$	deg
rear steer limit	$u_{\text{lim}}[2]$	$\pm 10$	deg
steer slew limit	$u_{\text{slew}}[1, 2]$	$\pm 140$	deg/s
slack penalty	$\eta$	$10^6$	–
time horizon	$N$	15	–

keep the roll rate within the limit is accomplished by reducing the front steering angle, which, if performed as the only action, would cause a decrease in yaw rate. However, the model predictive control scheme can coordinate the rear steering as well, and so the controller compensates for the reduction in the front steering angle by an increase in the magnitude of the rear steering angle to increase the yaw moment. The slight oscillation seen in Figure 6.5 is a result of the driver input changing in between subsequent controller time steps. As the driver changes the angle of the steering wheel, the controller must adjust both to the changed desired trajectory and also the resulting dynamics.

The results of the simulations demonstrate that the front and rear steering controller is more effective in controlling the roll rate while matching the yaw rate and sideslip trajectories of the vehicle. As seen in Figure 6.5, the required steering modifications to the front and rear of the vehicle are on the order of  $\pm 1^\circ$ , whereas the front and rear physical steering limits are  $\pm 30^\circ$  and  $\pm 20^\circ$ , respectively. These small magnitude corrections illustrate that standard rear-steering systems such as those seen on a few recent production vehicles have sufficient actuator authority to significantly influence the roll states of the vehicle if coordinated with front steering angle corrections.

The simulations presented here highlight the value of the model predictive controller, as the roll states are significantly modified while degradation of the planar vehicle behavior is minimized. This ensures that the actions of the controller preserve the validity of the driver's model of the vehicle behavior, enabling the driver to handle the tasks of lanekeeping and obstacle avoidance. Additionally, it is clear that the magnitude of the steering corrections remain small when using rear-wheel steering as a second actuator, minimizing modeling error and maximizing controller performance.

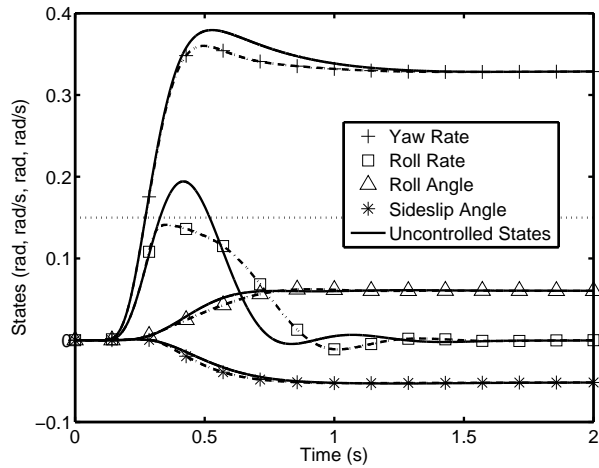


Figure 6.4: Vehicle state trajectories for rear wheel steering controller

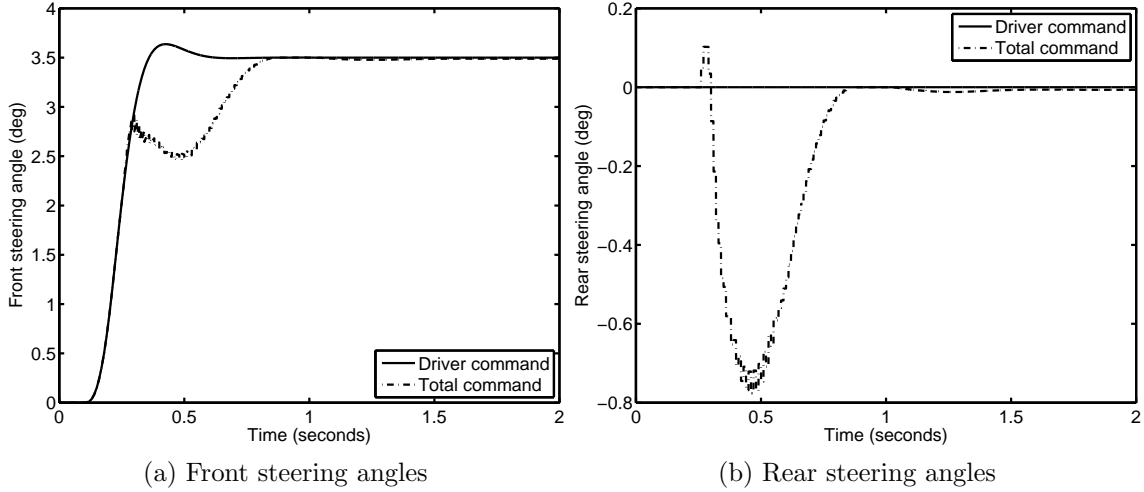


Figure 6.5: Inputs for controlled fast ramp steer with rear wheel steering

### 6.3 Discussion

In this chapter, a pair of controllers designed to coordinate the actions of different actuator sets for control of vehicle roll rate were presented. While both controllers successfully coordinated the vehicle actuators to respect the roll state limits, the deviation in the planar state tracking was significantly lower using a front- and rear-wheel steering controller than using rear-wheel drive and braking to augment front steering control.

The nonlinear simulation also demonstrates that the rear-wheel drive/brake controller must exert very large rear-wheel torques to achieve the desired result, which result in negative effects when considering the real pneumatic tire with coupled longitudinal and lateral forces. The four-wheel steering controller, however, uses very small steering corrections at each axle. Thus, the linear model used for the controller yields a more accurate representation of the vehicle behavior and results in better controller performance.

Despite the different dynamics involved in controlling the roll states of the vehicle, these controllers demonstrate the validity of the model predictive control framework used for both planar envelope and roll control. When phrased as a problem of tracking

the driver's desired vehicle behavior while incorporating limits on the vehicle handling, this structure allows the controller to appropriately incorporate the driver's input. The result is a driver assistance system that can operate in tight collaboration with a driver to make a vehicle safer in highly adverse conditions.

# Chapter 7

## Conclusions

The work presented in this dissertation demonstrates the feasibility of using real time estimates of friction and vehicle sideslip angle to assist drivers in stabilizing the vehicle at the limits of handling. The system, unlike production stability control systems, allows the driver complete freedom to maneuver the vehicle within the bounds of a safe handling envelope.

### 7.1 Summary

This dissertation presents a number of new concepts, summarized in the following subsections by chapter.

#### 7.1.1 Safe Handling Envelopes

Chapter 3 presents a method for finding a safe handling envelope. Once the tire-road friction coefficient and the speed are known, the method allows for the calculation of an envelope in terms of the planar vehicle states. The physically motivated boundaries of this envelope can be continuously updated in real time and offer the driver access to a significant portion of the state space. For intrepid drivers who are comfortable driving with the rear tires in a saturated condition, the boundaries of the handling envelope can be expanded to allow for high sideslip “drifting” maneuvers.

### 7.1.2 Real Time Model Predictive Control

Chapter 4 presents a model predictive envelope controller that enforces the boundaries of the safe handling envelopes in real time. The development of the controller includes the formulation of the Affine Force-Input model, a critical step in generating a problem that can be solved with convex optimization techniques in real time at 100Hz. The resulting controller yields smooth, progressive, and predictive augmentations to the driver's steering input to stabilize the vehicle while allowing it to reach the maximum extents of the safe handling envelope.

### 7.1.3 Real Time Friction and Sideslip Estimation

In order to implement the envelope controller in a production vehicle, sensing of the friction coefficient and vehicle sideslip angle are needed in real time. Because it is difficult to obtain measurements of these quantities with inexpensive sensors, Chapter 5 describes the implementation of an estimation technique that utilizes steering torque measurements to supplement readily available inertial sensors to provide the necessary information to the envelope controller. Despite guarantees of stability of the two separate algorithms, the coupling of the controller and estimator sometimes led to poor system performance in experimental testing. The reasons for these performance issues are analyzed and several solutions to this problem are introduced.

### 7.1.4 Extension of the Envelope Control Technique

The envelope controller presented in this dissertation is designed to control the planar states of the vehicle. Yet there are other vehicle control problems that can be phrased in terms of driver intent that must be limited by a safe envelope. The model predictive envelope control technique may be extended to handle many of these problems. Chapter 6 presents a controller of the same model predictive control form that is used to coordinate multiple vehicle actuators to prevent the vehicle roll states from exceeding the bounds of a safe envelope.

## 7.2 Future Work

This dissertation has demonstrated that the model predictive envelope controller yields good performance in conjunction with the human driver, and that control of the front steering of the vehicle in response to the friction conditions in the environment can rapidly and smoothly stabilize the vehicle. However, there are a few key areas in which this work may be extended and improved.

### 7.2.1 Driver Feedback

In the discussion in Chapter 5, the issue of informing the driver of the controller action was briefly addressed. In experimental testing, it was noted by several drivers that it often felt like the vehicle dramatically understeered, particularly with certain controller settings. In many of these cases, the vehicle was actually doing just the opposite and tending toward oversteer, but the controller was countersteering to prevent a spin. Thus, the drivers were merely misunderstanding the control action. Developing haptic feedback to inform the driver of the augmented steering command would likely improve the interpretation by the driver and lead to better acceptance of the system by drivers.

### 7.2.2 Controller Complexity

The model predictive envelope controller presented in this dissertation is an optimal control design for a particular set of specified criteria. However, a relatively powerful computer is required to solve the problem in real time on the vehicle. At present, ruggedized computers suitable for installation in a vehicle are expensive and lack the speed needed for the control computations. However, using the phase-plane analysis presented in Chapter 3, other less computational techniques for controlling the handling dynamics could be compared to the model predictive controller to develop a controller suitable for use in currently available production hardware.

### 7.2.3 Handling Environmental Constraints

The safe handling envelopes presented in Chapter 3 are calculated based on estimates of the maximum vehicle performance. When the controller enforces these boundaries, there are cases in which the driver steers to travel through a corner but the controller limits the minimum radius of the corner that the vehicle can achieve. When the envelope is calculated correctly, the controller is not “taking away” performance, but rather the driver’s intended path is unachievable. In this case, a new path that is achievable must be selected, either by the driver or by the controller.

The action of the current model predictive controller is to maintain the minimum radius corner since the objective of the controller is to match the intent of the driver. However, a different formulation of the control objective might be to find and traverse a safe trajectory, regardless of driver input. This would be a significant departure from the intent of the current controller, yet it would be possible to use additional information about obstacles and the environment to choose a safer alternative path. Integration of environmental sensing would also allow for prediction of infeasible trajectories and the ability to keep the vehicle out of these hazardous situations. Despite the different objectives of these controllers, the control framework presented in this dissertation may be used as a foundation upon which to base the development of this new control design.

## 7.3 Outlook

The envelope control approach to assisting drivers in stabilizing a vehicle shows great promise. The additional information provided to the controller by the friction and sideslip estimation technique yields a controller that allows a skilled driver to utilize the maximum handling capabilities of the vehicle. There are, of course, a number of challenges in refining the system to the point of being ready for installation in production cars, but this dissertation demonstrates the advantages of the system. Additionally, hybrid and electric cars and the use of electric motors to actuate steering systems are becoming increasingly common, providing the opportunity for tighter

control and additional driver assistance over all aspects of the driving experience. These new opportunities for control can allow the designers of driver assistance to develop seamless systems that allow even the most intrepid drivers to enjoy the experience of driving, knowing that somewhere under the hood is a controller to keep them safe.

# Appendix A

## X1 Experimental Test Vehicle

The X1 experimental test vehicle is an electric vehicle designed and constructed by students at Stanford University. This vehicle leverages electronic and physical modularity to allow for adaptation to changing research needs and the creation of student projects focused on particular subsystems of the vehicle.

### A.1 Physical Design

X1 was designed with the research needs and manufacturing capabilities of students at the Dynamic Design Lab in mind. Because the construction of large body panels with complex geometries was incompatible with the available fabrication equipment, the structure of the chassis was designed not only to provide strength and rigidity, but also to suggest the form of the car. However, this was not the only consideration, as the safety of students operating X1 for vehicle dynamics is paramount in all testing situations. Therefore, the chassis was also designed to protect the occupants in case of an impact or rollover. The final vehicle design, as seen in Figure A.1, includes a full roll cage, achieves an estimated  $10000 \frac{ft-lbf}{deg}$ , and suggests the shape of a car body, satisfying the design objectives.



Figure A.1: X1 steer and drive by-wire research testbed

### A.1.1 Modularity Concept

In the design phase of the vehicle, the meaning of modularity was discussed at length and many different concepts of “modular design” were generated. Ultimately, the driving force behind the design was determined to be maximum utility for vehicle dynamics research. Therefore, the modules were defined such that there is a chassis module along with front and rear suspension modules. With this definition of the modularity, projects that seek to use different actuators such as active suspension, steer-by-wire, active camber, or independent drive can all be accommodated with minimal changes to the remainder of the system. Supporting this modularity concept is a by-wire design that limits the connections to each suspension module to a power bus, a communication bus, and a dry-disconnect hydraulic braking line. Thus, aside from these three connections, each module is an isolated system that can be designed, constructed, and tested independently before installation on the vehicle.

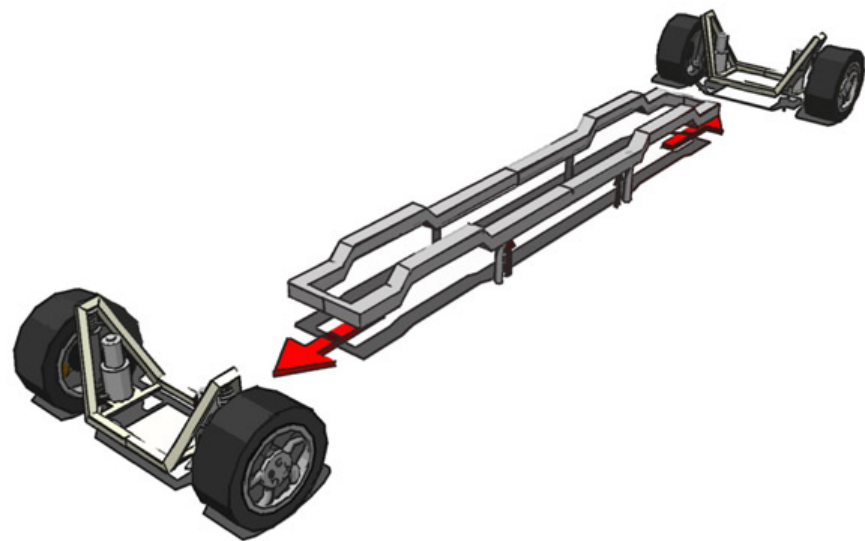


Figure A.2: Front-Middle-Rear Modularity Concept

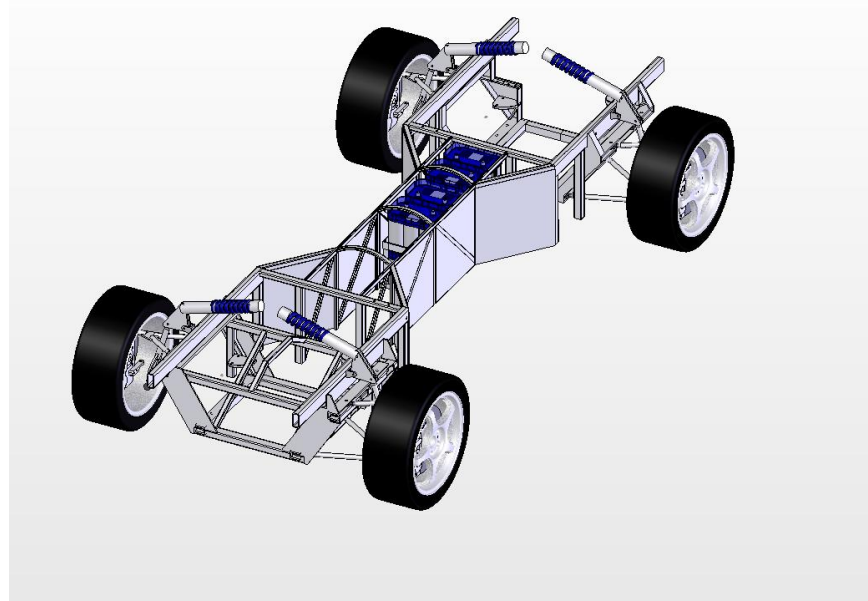


Figure A.3: CAD Mockup of Modular Structure

### A.1.2 Actuation Opportunities

In designing X1 to be modular, the intent was to create as many opportunities to alter the actuation scheme of the vehicle as possible. Therefore, the first front and rear modules built for the vehicle are based on a double A-arm pushrod suspension that leaves room in the module for a drive system and motors to implement steer-by-wire. By utilizing the pushrod to locate the spring and shock remotely, this design also includes a rotational joint upon which a motor could be mounted to actuate the suspension. Furthermore, work done by Laws [39] was based on the X1 modular architecture and demonstrated that a suspension capable of actively controlling camber, steering, and vertical load can be installed on the vehicle.

### A.1.3 Drivetrain

The drive system selected for X1 is a battery-powered DC brushless motor obtained from UQM Technologies. The motor is rated for 75 kW of power and 240 Nm of torque and can be driven up to 8000 RPM. Rather than include the additional mechanical complexity of a transmission, the motor is coupled directly to a custom fabricated Ford 9" differential geared with a 7.33:1 ring and pinion, providing all of the gear reduction necessary for the drivetrain. With the gearing selection, the vehicle is capable of approximately 80 MPH before reaching the limit of the motor speed. This direct-drive design also saves space and weight, a critical consideration since it is desirable to locate the motor directly in the driven module. The UQM motor also provides a research advantage in that it communicates with the vehicle through the CAN communication protocol and reports real time measurements of battery pack voltage, battery current draw, motor RPM, and motor torque. The input to the motor can also be set up to accept torque or speed commands, allowing higher level vehicle dynamics controllers such as the model predictive envelope controller to utilize torque measurements and output torque commands.

## A.2 Electrical Design

The electrical design of the vehicle is comprised of two parts. The first is the power system for the electric drive and the second is the electronics architecture that allows the modules to be controlled through a data network.

### A.2.1 Power System

There are a number of considerations for an electric vehicle power system. The first is the ability of the system to supply energy to the electric motor, particularly the total energy storage capacity. However, it is also important to consider the maximum current that the system can source. Furthermore, it is important to choose a system that provides relatively easy and robust charging. For this reason, the high voltage system for X1 is comprised of 28 lead acid batteries. While this battery chemistry does not have the highest energy density of all the technologies on the market, the batteries can supply very large currents and are significantly more tolerant of deep discharge and rapid charging than other battery chemistries. The batteries are also complemented with a pair of onboard chargers capable of charging at a rate of 3.3 kW each. The nominal charged voltage of this system is approximately 360V, allowing for a significant power draw with lower currents than other low voltage systems.

### A.2.2 Data Network

The electronic modularity of the vehicle is based on a data network implemented with the state-of-the-art Flexray communication protocol [5]. Flexray offers several advantages over previous vehicle communication protocols such as CAN, LIN, and pure parallel wiring harnesses. With Flexray, redundancy in the network is easily accomplished and large data packets containing many tens of bytes may be sent from node to node. Furthermore, the protocol includes a time-triggered scheme for high priority information to be sent between nodes. The ability to send multiple floating point numbers between nodes with guaranteed latency opens up the possibility of distributed computing on the vehicle, and supports the independence of each module.

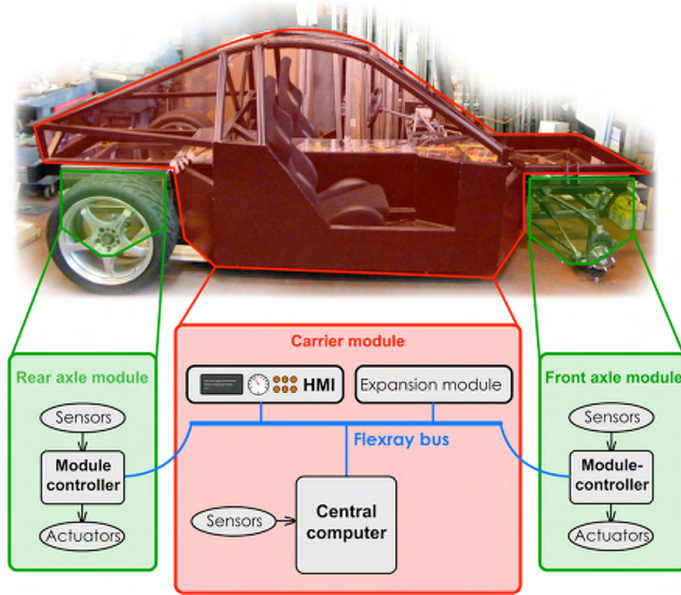


Figure A.4: Electronic Modularity Concept

### A.3 Discussion

With the mechanical and electrical modularity of the system, the X1 test vehicle provides an excellent platform for vehicle dynamics research. The chassis is safe, flexible, and will evolve with the research of the Dynamic Design Lab. Finally, the ability to distribute computing load across various modules will allow for the development of future advanced vehicle controllers such as the one presented in this thesis.

# Bibliography

- [1] *Bosch Automotive Handbook, 6th Edition.* SAE Society of Automotive Engineers, Inc, 2004.
- [2] Guillaume Baffet and Ali Charara. An observer of tire-road forces and friction for active security vehicle systems. *IEEE/ASME Transactions on Mechatronics*, 12(6), 2007.
- [3] Craig E. Beal and J. Christian Gerdes. Enhancing Vehicle Stability through Model Predictive Control. In *Proceedings of the ASME Dynamic Systems and Controls Conference*, September 2009.
- [4] Craig E. Beal and J. Christian Gerdes. Experimental Validation of a Linear Model Predictive Envelope Controller in the Presence of Vehicle Nonlinearities. In *Proc. of the 2010 IFAC Symp. on Advances in Automotive Control, Munich.*, July 2010.
- [5] Peter Bergmiller. Design and implementation of a controller network for a modular by-wire vehicle for safety-critical real-time applications. Master's thesis, Technical University of Braunschweig, 2008.
- [6] J. E. Bernard, L. Segel, and R. E. Wild. Tire shear force generation during combined steering and braking manueuvres. *SAE World Congress*, 1977. Paper number 770852.
- [7] D. Bernardini, S. Di Cairano, Alberto Bemporad, and H.E. Tseng. Drive-by-wire Vehicle Stabilization and Yaw Regulation: a Hybrid Model Predictive Control

- Design. In *Proceedings of the 48th IEEE Conference on Decision and Control, Shanghai, China*, December 2009.
- [8] David M. Bevly, Robert Sheridan, and J. Christian Gerdes. Integrating INS sensors with GPS velocity measurements for continuous estimation of vehicle sideslip and tire cornering stiffness. In *Proceedings of the 2001 American Control Conference (ACC), Arlington, Virginia*, 2001.
  - [9] Francesco Borrelli, Jahan Asgari, Hongtei Eric Tseng, and Davor Hrovat. Predictive Active Steering Control for Autonomous Vehicle Systems. *IEEE Transactions on Control Systems Technology*, 15(3), May 2007.
  - [10] Stephen Boyd and Lieven Vandenberghe. *Convex Optimization*. Cambridge University Press, Cambridge, UK, 2004.
  - [11] CarAdvice.com.au. Electronic stability control getting more popular, August 2007.
  - [12] C. R. Carlson and J. C. Gerdes. Optimal rollover prevention with steer by wire and differential braking. In *IMECHE03*, 2003.
  - [13] Bo-Chiuan Chen and Huei Peng. A real-time rollover threat index for sports utility vehicles. In *Proceedings of the American Control Conference (ACC), San Diego, California*, June 1999.
  - [14] Andy Chuter. Airbus launches more safety aids. *Flight International*, page 26, 1997.
  - [15] John Croft. Taming loss-of-control: Solutions are elusive. *Aviation Week & Space Technology*, 157(9):50, August 2002.
  - [16] Jennifer N. Dang. Statistical analysis of the effectiveness of electronic stability control systems. Technical report, NHTSA, July 2007.
  - [17] Moritz Diehl, Hans Joachim Ferreau, and Niels Haverbeke. *Nonlinear Model Predictive Control*. Springer Berlin/Heidelberg, 2009.

- [18] Howard Dugoff, P.S. Fancher, and Leonard Segel. An analysis of tire traction properties and their influence on vehicle dynamic performance. In *Proceedings of the SAE World Congress, Paper 700377*. 1970.
- [19] P. Falcone, F. Borrelli, H. E. Tseng, J. Asgari, and D. Hrovat. Linear time-varying model predictive control and its application to active steering systems: Stability analysis and experimental validation. *International Journal of Robust and Nonlinear Control*, 6:862–975, July 2007.
- [20] E Fiala. Lateral forces on rolling pneumatic tires. In *Zeitschrift V.D.I. 96*. 1954.
- [21] Michael Gipser. Ftire : a physically based application-oriented tyre model for use with detailed mbs and finite-element suspension models. *Vehicle System Dynamics*, 43(Supplement):76–91, 2005.
- [22] Havard Fjaer Grip, Lars Imsland, Tor A. Johansen, Thor I. Fossen, Jens C. Kalkkuhl, and Avshalom Suissa. Nonlinear vehicle velocity observer with road-tire friction adaptation. *Proceedings of the 45th IEEE Conference on Decision & Control, San Diego, CA*, 2006.
- [23] Fredrik Gustafsson. Monitoring tire-road friction using the wheel slip. *IEEE Control Systems Magazine*, pages 42–49, 1998.
- [24] R. Hadekel. The mechanical characteristics of pneumatic tyres. In *S and T Memo TPA3/TIB*. 1952.
- [25] S. P. Han and O. L. Mangasarian. Exact penalty functions in nonlinear programming. *Mathematical Programming*, 17:251–269, 1979.
- [26] Junjie He, David A. Crolla, Martin C. Levesley, and Warren J. Manning. Integrated chassis control through coordination of active front steering and intelligent torque distribution. In *Proceedings of the 2004 International Symposium on Advanced Vehicle Control, Arnhem, Netherlands.*, August 2004.

- [27] P. Helnwein, C. J. Lie, G. Meschke, and H. A. Mang. A new 3-D finite element model for cord-reinforced rubber composite: application to analysis of automobile tires. *Finite elements in analysis and design*, 14(1):1–16, 1993.
- [28] Rami Y. Hindiyeh and J. Christian Gerdes. Equilibrium Analysis of Drifting Vehicles for Control Design. In *Proceedings of the ASME Dynamic Systems and Controls Conference*, 2009.
- [29] Yutaka Hirano and Katsumi Fukatani. Development of robust active rear steering control. In *Proceedings of the 1996 International Symposium on Advanced Vehicle Control, Aachen, Germany.*, June 1996.
- [30] Robert C. Hoffman, Jeffrey L. Stein, Loucas S. Louca, and Kunsoo Huh. Using the milliken moment method and dynamic simulation to evaluate vehicle stability and controllability. In *Proceedings of the International Mechanical Engineering Congress and Exposition, Anaheim, CA*, November 2004.
- [31] Y.-H.J. Hsu, S.M. Laws, and J.C. Gerdes. Estimation of tire slip angle and friction limits using steering torque. *Control Systems Technology, IEEE Transactions on*, 18(4):896–907, July 2010.
- [32] Yung-Hsiang Judy Hsu and J. Christian Gerdes. The predictive nature of pneumatic trail: Tire slip angle and peak force estimation using steering torque. In *Proceedings of the International Symposium on Advanced Vehicle Control (AVEC), Kobe, Japan*, October 2008.
- [33] Yung-Hsiang Judy Hsu and J. Christian Gerdes. Envelope control: Keeping the vehicle within its handling limits using front steering. In *Proc. of the 21st Intl. Symp. on Dynamics of Vehicle on Roads and Tracks*, August 2009.
- [34] Wookug Hwang and Byung-Suk Song. Road condition monitoring system using tire-road friction estimation. In *Proceedings of the International Symposium on Advanced Vehicle Control (AVEC)*, 2000.

- [35] Kyongsu Yi Jangyeol Yoon, Dongshin Kim. Design of a rollover index-based vehicle stability control scheme. *Vehicle System Dynamics*, 45(5):459–475, May 2007.
- [36] Jianbo Lu and Dave Messih and Albert Salib. Roll Rate Based Stability Control - The Roll Stability Control<sup>TM</sup> System. Ford Motor Company, Paper Number 07-136.
- [37] U. Kiencke and A. Daib. Observation of lateral vehicle dynamics. *Control Engineering Practice*, 5(8):1145–1150, 1997.
- [38] M. Koishi, K. Kabe, and M. Shiratori. Tire cornering simulation using an explicit finite element analysis code. *Tire Science and Technology*, 26(2):109–119, April 1998.
- [39] Shad M. Laws. *An Active Camber Concept for Extreme Maneuverability: Mechanistic Suspension Design, Tire Modeling, and Prototype Development*. PhD thesis, Stanford University, 2010.
- [40] Shad M. Laws, Christopher D. Gadda, and J. Christian Gerdes. Frequency characteristics of vehicle handling: Modeling and experimental validation of yaw, sideslip, and roll modes to 8hz. In *Proceedings of the International Symposium on Advanced Vehicle Control (AVEC), Taipei, Taiwan*, August 2006.
- [41] Heinz Leffler, Reinhard Auffhammer, Reent Heyken, and Harald R'oth. New driving stability control system with reduced technical effort for compact and medium class passenger cars. In *Proceedings of the 1998 SAE International Congrees and Exposition, Detroit, Michigan.*, February 1998.
- [42] W.J. Manning and D.A. Crolla. A review of yaw rate and sideslip controllers for passenger vehicles. *Transactions of the Institute of Measurement and Control*, 29(2):117–135, 2007.
- [43] Shinji Matsumoto, Hirotugu Yamaguchi, Hideaki Inoue, and Yoshiki Yasuno. Braking force distribution control for improved vehicle dynamics. In *Proceedings of the 1992 International Symposium on Advanced Vehicle Control.*, 1992.

- [44] J. Mattingley and S. Boyd. CVXMOD: Convex optimization software in Python (web page and software). <http://cvxmod.net/>, 2008.
- [45] J. Mattingley and S. Boyd. Automatic code generation for real-time convex optimization. In Y. Eldar and D. P. Palomar, editors, *Convex Optimization in Signal Processing and Communications*. Cambridge University Press, Cambridge, UK, 2009.
- [46] J. Mattingley and S. Boyd. Real-time convex optimization in signal processing. *IEEE Signal Processing Magazine*, 27:50–61, May 2010.
- [47] W. F. Milliken and D. L. Milliken. *Race Car Vehicle Dynamics*. SAE International, 1995.
- [48] NHTSA. Traffic safety facts 2009: A compilation of motor vehicle crash data from the fatality analysis reporting system and the general estimates system. Technical report, National Center for Statistics and Analysis, 2009.
- [49] David M. North. Finding common ground in envelope protection systems. *Aviation Week & Space Technology*, 153(9):66, August 2000.
- [50] Eiichi Ono, Shigeyuki Hosoe, Hoang D. Tuan, and Shun'ichi Doi. Bifurcation in vehicle dynamics and robust front wheel steering control. *IEEE Transactions on Control Systems Technology*, 6:412–420, 1998.
- [51] Hans B. Pacejka. *Tire and Vehicle Dynamics*. Society of Automotive Engineers, Warrendale, PA USA, 2nd edition, 2005.
- [52] Hans B. Pacejka and Egbert Bakker. The magic formula tyre model. *Vehicle System Dynamics*, 21(S1):1–18, 1992.
- [53] Giovanni Palmieri, Osvaldo Barbarisi, Stefano Scala, and Luigi Glielmo. A preliminary study to integrate LTV-MPC Lateral Vehicle Dynamics Control with a Slip Control. In *Proceedings of the 48th IEEE Conference on Decision and Control and 28th Chinese Control Conference*, December 2009.

- [54] Laura Ray. Nonlinear tire force estimation and road friction identification, simulation and experiments. *Automatica*, 33(10):1819–1833, 1997.
- [55] R. S. Rice. Measuring car-driver interaction with the g-g diagram. In *Proceedings of the International Engineering Congress, Detroit, MI*, January 1973.
- [56] K. Rock, S. Beiker, S. Laws, and J.C. Gerdes. Validating GPS Based Measurements for Vehicle Control. In *Proceedings of ASME International Mechanical Engineering Congress and Exposition, Orlando, Florida*, 2005.
- [57] Jihan Ryu and J. Christian Gerdes. Integrating Inertial Sensors with GPS for Vehicle Dynamics Control. *Journal of Dynamic Systems, Measurement, and Control*, 126:243–254, June 2004.
- [58] H. Sakai. Theoretical and experimental studies on the dynamic properties of tyres part 4: Investigations of the influences of running conditions by calculation and experiment. *Int. J. of Vehicle Design*, No. 3, 3:333–375, 1982.
- [59] Y. Shibahata, K. Shimada, and T. Tomari. Improvement of Vehicle Maneuverability by Direct Yaw Moment Control. *Vehicle System Dynamics*, 22:465–481, 1993.
- [60] Taehyun Shim, Daniel Toomey, Chinar Ghike, and Hemant M. Sardar. Vehicle rollover recovery using active steering/wheel torque control. *International Journal of Vehicle Design*, 46(1):51–71, 2008.
- [61] P. S. Shoemaker. Tire engineering by finite element modeling. *SAE World Congress*, 1984. Paper number 840065.
- [62] Shoji Inagaki, Ikuo Kshiro, and Masaki Yamamoto. Analysis on Vehicle Stability in Critical Cornering Using Phase-Plane Method. In *Proceedings of the International Symposium on Advanced Vehicle Control*, 1994.
- [63] Henk Smakman. Functional integration of active suspension with slip control for improved lateral vehicle dynamics. In *Proceedings of the 2000 International Symposium on Advanced Vehicle Control, Ann Arbor, Michigan.*, June 1996.

- [64] Joanny Stephant, Ali Charara, and Dominique Meizel. Virtual sensor: Application to vehicle sideslip angle and transversal forces. *IEEE Transactions on Industrial Electronics*, 51(2), 2004.
- [65] Alexander Strashny. An analysis of motor vehicle rollover crashes and injury outcomes. Technical report, National Highway Traffic Safety Administration, 2007.
- [66] Alfred Straub. Dsc (dynamic stability control) in bmw 7 series cars. In *Proceedings of the 1996 International Symposium on Advanced Vehicle Control, Aachen, Germany.*, June 1996.
- [67] J. T. Tielking. A finite element tire model. *Tire Science and Technology*, 1(1):50–63, January 1983.
- [68] U.S. National Highway Traffic Safety Administration. Nhtsa safercar rollover information page. <http://www.safercar.gov/Rollover/>, 2011.
- [69] Anton T. van Zanten. Evolution of Electronic Control Systems for Improving the Vehicle Dynamic Behavior. In *Proceedings of the International Symposium on Advanced Vehicle Control*, 2002.
- [70] Anton T. van Zanten, Rainer Erhardt, Georg Pfaff, Friedrich Kost, Uwe Hartmann, and Thomas Ehret. Control Aspects of the Bosch-VDC. In *Proceedings of the International Symposium on Advanced Vehicle Control*, June 1996.
- [71] P. J. T. Venhovens and K. Naab. Vehicle dynamics estimation using Kalman filters. *Vehicle System Dynamics*, 32:171–184, 1999.
- [72] M. Mitchell Waldrop. Flying the electric skies. *Science*, 244(4912):pp. 1532–1534, 1989.
- [73] Klaus H. Well. Aircraft control laws for envelope protection. In *AIAA Guidance, Navigation, and Control Conference and Exhibit*, 2006. AIAA 2006-6055.

- [74] Paul Yih and J. Christian Gerdes. Steer-by-wire for vehicle state estimation and control. In *Proceedings of the International Symposium on Advanced Vehicle Control (AVEC), Arnhem, The Netherlands*, 2004.
- [75] Tohru Yoshioka, Tomohiko Adachi, Tetsuro Butsuen, Haruki Okazaki, and Hiro-taka Mochizuki. Application of sliding-mode control to control vehicle stability. In *Proceedings of the 1998 International Symposium on Advanced Vehicle Control.*, 1998.